UNIVERSIDADE FEDERAL DO CEARÁ
CENTRO DE TECNOLOGIA
DEPARTAMENTO DE ENGENHARIA QUÍMICA
PROGRAMA DE PÓS-GRADUAÇÃO EM EMGENHARIA QUÍMICA

RAFAEL AUGUSTO MORALES OSPINO

CO_2 POST-COMBUSTION CAPTURE FROM A COAL-FIRED POWER PLANT: ASSESSMENT OF COMMERCIAL AND SYNTHESIZED ZEOLITES AND MOVING BED SIMULATIONS

FORTALEZA

2021

RAFAEL AUGUSTO MORALES OSPINO

CO_2 POST-COMBUSTION CAPTURE FROM A COAL-FIRED POWER PLANT: ASSESSMENT OF COMMERCIAL AND SYNTHESIZED ZEOLITES AND MOVING BED SIMULATIONS

Tese apresentada ao Programa de Pós-Graduação em Engenharia Química da Universidade Federal do Ceará, como parte dos requisitos para obtenção do Título de Doutor em Engenharia Química. Área de Concentração: Processos Químicos e Bioquímicos.

Orientadora: Profª. Drª. Diana Cristina Silva de Azevedo
Coorientadores: Prof. Dr. Moisés Bastos Neto & Prof. Dr. Enrique Vilarrasa García

FORTALEZA

2021

Dados Internacionais de Catalogação na Publicação
Universidade Federal do Ceará
Biblioteca Universitária
Gerada automaticamente pelo módulo Catalog, mediante os dados fornecidos pelo(a) autor(a)

M828c Morales Ospino, Rafael Augusto.
CO2 Post-Combustion Capture From A Coal-Fired Power Plant: Assessment Of Commercial And Synthesized Zeolites And Moving Bed Simulations / Rafael Augusto Morales Ospino. – 2021.
133 f. : il. color.

Tese (doutorado) – Universidade Federal do Ceará, Centro de Tecnologia, Programa de Pós-Graduação em Engenharia Química, Fortaleza, 2021.
Orientação: Profa. Dra. Diana C. S. De Azevedo.
Coorientação: Prof. Dr. Moisés Bastos-Neto; Enrique Vilarrasa García.

1. Adsorption. 2. CO2 capture. 3. Zeolites. 4. Fly ash. 5. Process simulation. I. Título.

CDD 660

RAFAEL AUGUSTO MORALES OSPINO

CO_2 POST-COMBUSTION CAPTURE FROM A COAL-FIRED POWER PLANT: ASSESSMENT OF COMMERCIAL AND SYNTHESIZED ZEOLITES AND MOVING BED SIMULATIONS

Thesis submitted to Federal University of Ceará as a requirement to obtain the Doctor's Degree in Chemical Engineering.
Concentration area: Chemical and biological separation processes.

Approved on August 05 2021.

_____
Prof. Dr. Moisés Bastos Neto
Federal University of Ceará

_____
Prof. Dr. Arvind Rajendran
University of Alberta

_____
Prof. Dr. Paul Webley
Monash University

_____
Prof. Dr. Thiago Fernandes de Aquino
SATC University

_____
Prof. Dr. Sebastião Mardônio Pereira de Lucena
Federal University of Ceará

RESUMO

A necessidade incessante de suprir a demanda energética global tem levado à queima generalizada de combustíveis fósseis, provocando a liberação de gases de efeito estufa. O efeito de retenção de calor devido às concentrações alarmantes de gases de efeito estufa como o CO_2 está causando danos à camada de ozônio e, portanto, contribuindo para o aquecimento global. Além disso, os processos de Captura e Armazenamento de Carbono (CCS) estão atualmente sendo investigados para mitigar as crescentes emissões de CO_2 na atmosfera. Em usinas de energia que utilizam carvão como combustível, além da problemática das emissões de CO_2, o acúmulo de cinzas volantes derivados da queima do carvão tornou-se uma grande preocupação. Na tentativa de fornecer uma solução conjugada para as emissões de CO_2 e descarte de cinzas volantes, materiais adsorventes, como zeólitas sintetizadas a partir de cinzas volantes de duas usinas termoelétricas brasileiras foram avaliados como materiais potenciais para capturar CO_2. As zeólitas à base de cinzas volantes (uma tipo X e outra tipo A) foram comparadas com zeólitas comerciais de referência usados para separação de CO_2 /N_2 como zeólita 13X e 4A por meio de caracterização de adsorção de gás (N_2 em 77 K e CO_2 em isotermas de 273 K) e métricas de adsorção. Testes de equilíbrio foram realizados para obter isotermas de adsorção de CO_2, N_2 e vapor d'água em diferentes temperaturas com o auxílio de uma balança de suspensão magnética. Além disso, uma unidade de adsorção de oscilação de temperatura em leito móvel (MBTSA) para capturar CO_2 com zeólita comercial 13X de uma corrente de gás de combustão contendo apenas N_2 (85% vol.) e CO_2 (15% vol.) foi simulada por meio de um modelo com balanços apropriados de fenômenos de transporte. Considerou-se que o gás de combustão foi submetido a uma operação de secagem cuja penalidade energética foi considerada no item de consumo energético da unidade. O modelo consistia em três seções que abrangiam todo o sistema MBTSA: seções de adsorção, regeneração e resfriamento. Cada seção do MBTSA foi modelada individualmente, mas interconectada por meio de um modelo composto que simulou a unidade toda. Devido ao grande número de variáveis e parâmetros envolvidos no sistema MBTSA que podem ser organizados em diversos conjuntos de dados de entrada, efetuou-se um estudo paramétrico analisando o efeito de diferentes variáveis de

processo nos principais parâmetros de desempenho (ou seja, recuperação e pureza de CO_2 no corrente produto, consumo de energia e produtividade da unidade). Os resultados de caracterização e equilíbrio indicaram que os materiais sintetizados a partir de cinzas volantes podem ser considerados como adsorventes promissores de baixo custo para captura de CO_2. As amostras sintetizadas exibiram características, capacidade de adsorção de CO_2 e seletividades semelhantes como suas contrapartes comerciais. As isotermas experimentais de adsorção água pura e binária água/CO_2 indicaram a necessidade de secar os gases de combustão antes de sua utilização no processo de captura de carbono, dada a alta afinidade das zeólitas em adsorver umidade sobre o CO_2. Por outro lado, os resultados da simulação sugeriram que, nas condições estudadas, poderiam ser alcançados valores de até 99% e 91% de recuperação e pureza de CO_2, respectivamente. Os valores da demanda de energia específica, incluindo a penalidade de remoção de água, foram considerados comparáveis aos valores relatados para a absorção de amina líquida, indicando que o processo MBTSA pode ser um candidato potencial para captura de CO_2 em cenário pós-combustão em grande escala.

Palavras-chave: adsorção; captura de CO_2; leito móvel; zeólitas; cinza volante; simulação de processo.

ABSTRACT

The incessant necessity to supply the global energy demand has led to the widespread burning of fossil fuels provoking the release of greenhouse gases. The heat-trapping effect due to the alarming concentrations of greenhouse gases like CO_2 is causing damages to the ozone layer and thus, contributing to global warming. On top of this, Carbon Capture & Storage processes (CCS) are currently being subjected of investigation to mitigate the increasing CO_2 emissions into the atmosphere. In power plants employing coal as fuel, besides the CO_2 emissions problematic, fly ash accumulation derived from the coal burning has become a major concern. In attempt to provide a conjugated solution to both the CO_2 emissions and fly ash discarding, adsorbent materials such as zeolites synthesized from fly ash of two Brazilian coal-fired power plants were evaluated as potential materials to capture CO_2. Fly ash-based zeolites (one type X and other type A) were compared to benchmark commercial zeolites used for CO_2/N_2 separation like zeolite 13X and 4A by means of gas adsorption characterization (N_2 at 77 K and CO_2 at 273 K isotherms) and adsorption metrics. Equilibrium experiments were performed in all the samples to obtain CO_2, N_2 and water vapor adsorption isotherms at different temperatures with the aid of a magnetic suspension balance. Furthermore, a Moving Bed Temperature Swing Adsorption (MBTSA) unit to capture CO_2 with commercial zeolite 13X from a flue gas stream only containing N_2 (85 % vol.) and CO_2 (15 %.vol.) was simulated through a model with appropriate transport phenomena balances. The flue gas was assumed to undergo a drying operation whose energy penalty was taken into account within the energetic consumption item of the unit. The model consisted of three sections that comprised the whole MBTSA system: adsorption, regeneration and cooling sections. Every section of the MBTSA was individually modeled but interconnected by means of a composite model that simulated the entire unit. Due to the large number of variables and parameters involved in the MBTSA system that can be arranged in diverse input datasets, a parametric study analyzing the effect of different process variables on key performance parameters of the process (i.e., CO_2 recovery and purity of the product stream, energy consumption and productivity) was carried out. The characterization and equilibrium results indicated that the synthesized materials from fly ash can be considered as low cost

promising CO_2 adsorbents. The synthesized samples exhibited similar characteristics, CO_2 adsorption capacities and selectivities as their commercial counterparts. The pure water and binary water/CO_2 experimental adsorption isotherms indicated the necessity to dry the flue prior to its use in a carbon capture process given the high affinity of zeolites to adsorb moisture over CO_2. On the other hand, the simulation results suggested that, under the studied conditions, values up to 99% and 91% of CO_2 recovery and purity could be achieved, respectively. Values of the specific energy demand, including the water removal penalty, were found to be comparable to reported values for amine liquid absorption indicating that MBTSA process might be a potential candidate process for large-scale post-combustion CO_2 capture.

Keywords: adsorption; CO_2 capture; moving bed; zeolites; fly ash; process simulation.

.

LIST OF FIGURES

LIST OF TABLES

NOMENCLATURE

A_v	Heat exchange area per unit volume, m^{-1}
$A_{section}$	Sectional area, m^2
b_i	Affinity constant for component *i*, Pa^{-1}
b_{0i}	Affinity constant for component *i* at a reference temperature T_0, Pa^{-1}
C_{gT}	Gas mixture concentration, $mol.m^{-3}$
C_{gT0}	Gas mixture concentration at feed conditions, $mol.m^{-3}$
C_{gT}*	Dimensionless gas mixture concentration
$C_{g,i}$	Gas concentration of component *i*, $mol.m^{-3}$
$C_{g,i0}$	Gas concentration of component *i* at feed conditions, $mol.m^{-3}$
$C_{g,i}$*	Dimensionless gas concentration of component *i*
C_{pg}	Gas mixture calorific capacity at constant pressure, $J.mol^{-1}.K^{-1}$
$C_{pg,i}$	Gas calorific capacity at constant pressure of component *i*, $J.mol^{-1}.K^{-1}$
C_{ps}	Solid calorific capacity at constant pressure, $J.Kg^{-1}.K^{-1}$
C_{pw}	Wall calorific capacity at constant pressure, $J.Kg^{-1}.K^{-1}$
C_{vg}	Gas calorific capacity at constant volume, $J.mol^{-1}.K^{-1}$
D_{ax}	Axial mass dispersion coefficient of the gas mixture, $m^2.s^{-1}$
$D_{e,i}$	Effective diffusivity of component *i*, $m^2.s^{-1}$
$D_{k,i}$	Knudsen diffusivity of component *i*, $m^2.s^{-1}$
D_m	Molecular diffusivity, $m^2.s^{-1}$
D_p	Particle diameter, m
e_{H20}	Thermal energy per unit water removed, MJ kg^{-1} H_2O
e_w	wall thickness, m
F_s	solid mass flowrate, $kg.s^{-1}$
g	Gravity constant, $m.s^{-2}$
h_w	Heat transfer coefficient between the gas and the wall,$W.m^{-2}.K^{-1}$
h_w*	Dimensionless heat transfer coefficient between the gas and the wall
h_{w0}	Heat transfer coefficient between the gas and the wall at u_0, $\rho_{g,0}$,,$W.m^{-2}.K^{-1}$
K_D	Darcy constant in laminar flow, Pa s m^{-1}
K_i	Fitting parameter in Sips model
K_{LDF}	Linear Driving Force (LDF) mass transfer coefficient, s^{-1}
L	Length of a section of the moving bed, m
L_o	Bed length, m
m_{ads}	Adsorbent mass, kg
Mi	Molar mass of component *i*, $g.mol^{-1}$
n_i	Heterogeneity parameter of component *i* in Sips model
n_{0i}	Heterogeneity parameter of component *i* in Sips model at reference temperature T_0
NoC	Number of components
P	Pressure, Pa
P*	Dimensionless Pressure

P_0	Atmospheric pressure, Pa
$P_{0,i}$	Partial pressure of component *i* at feed conditions, Pa
Pi	Partial pressure of component *i*, Pa
qe,i	Equilibrium loading of component *i*, $mol.kg^{-1}$
*qe,i**	Dimensionless equilibrium loading of component *i*
qi	Average adsorbed concentration of component *i*, $mol.kg^{-1}$
*qi**	Dimensionless average adsorbed concentration of component *i*,
Qi	Measure of energy of adsorption of component *i* in Sips model, $J.mol^{-1}$
qm,i	Maximum adsorption capacity for component i , $mol.kg^{-1}$
qm0,i	Maximum adsorption capacity for component *i* at T_0 and $P_{0,i}$, $mol.kg^{-1}$
Rg	Ideal gas constant, $J.mol^{-1}.K^{-1}$
Rp	Particle radius, m
rp	Pore radius, m
t	Time domain, s
*t**	Dimensionless time
tR	Residence time, s
T	Gas temperature, K
T0	Reference gas temperature, 323 K
*T**	Dimensionless gas temperature
Tinf	External air or heat exchange fluid temperature, K
Treg	Regeneration temperature, K
Tw	Wall temperature, K
*Tw**	Dimensionless wall temperature, K
u	superficial gas velocity, $m.s^{-1}$
*u**	Dimensionless superficial gas velocity
us	solid velocity, $m.s^{-1}$
uo	feed gas velocity, $m.s^{-1}$
Ug	Overall heat transfer coefficient between the wall and the external air or heat exchange fluid, $W.m^{-2}.K^{-1}$
*Ug**	Dimensionless overall heat transfer coefficient between the wall and the external air or heat exchange fluid
v	Superficial velocity, $m.s^{-1}$
Vp	Specific pore volume, $m^3.kg^{-1}$
Vs	Specific solid volume, $m^3.kg^{-1}$
wads	solid loading in the adsorption section, kg
Xi	Fitting parameter in Sips model
yi	Molar fraction of component *i*
yi0	Molar fraction of component *i* at the feed of the adsorber
*z**	Dimensionless length

Greek letters

ΔL	Height of the MBTSA system, m
$(-\Delta H_{ads,i})$	Heat of adsorption of component *i,* $J.mol^{-1}$
α_i	Dimensionless parameter, *i=1, 2, 3, 4*.

βi	Dimensionless parameter, *i=1, 2, 3, 4*, 5, 6.
θ	Dimensionless parameter
φi	Dimensionless parameter, *i=1, 2.*
δ	Dimensionless parameter
γ	Adiabatic expansion coefficient for ideal gases.
λ	Heat axial dispersion coefficient, $W.m^{-1}.K^{-1}$
λ^*	Dimensionless heat axial dispersion coefficient
λ_0	Heat axial dispersion coefficient at u_0, $\rho_{g,0}$, $W.m^{-1}.K^{-1}$
μ_g	Gas viscosity, Pa.s
ρ_b	Bed density, $Kg.m^{-3}$
ρ_g	Gas density, $kg.m^{-3}$
$\rho_{g,0}$	Gas density at P_0, T_0, $kg.m^{-3}$
ρ_{H2O}	Water vapor density, $kg.m^{-3}$
ρ_w	Wall density, $kg.m^{-3}$
ε	void fraction
ε_p	Particle porosity

CONTENTS

1. INTRODUCTION

The constant accentuation of the global warming phenomenon during the last decades is probably one of the greatest challenges facing modern society. Since the period of the Industrial Revolution, human activity has become increasingly significant in contributing to climate change. To meet the needs arising from a more industrialized civilization, mainly non-renewable sources of energy have been employed. Consequently, the growing demand for energy to move the world has been mostly supplied by fossil fuel burning. A telling example is the energy generation from coal-fired power plants, which has led to the emission of several pollutants including SO_2, NO_X, particulate matter, heavy metals, CO_2 and fly ash (Guttikunda,Jawahar 2014, Smith et al. 2013). CO_2 is a major greenhouse gas effect, whereas fly ash is a solid by-product representing between 60 and 90 % of the whole combustion residues from coal-based power plants (Dindi et al. 2019). While the increasing CO_2 emissions to the atmosphere have become a major environmental concern, only close to 25% of the fly ash residue is estimated to have a further utility globally (Hosseini et al. 2018). Moreover, coal burning in power plants may continue growing owed to its abundance in the most energy-consuming countries such as China, the USA, parts of Europe, India and Australia unless new laws or regulations prohibit or discourage it. (Lior 2010, Belviso 2018a)

In the national context, there are two concerning scenarios regarding the coal exploitation and the fly ash generation. On the one hand, despite Brazil might not play a major role in the global production of coal (Restrepo et al. 2015), its coal reserves appeared to be large enough to generate power during 5 centuries straight at the present consumption rate (Izidoro et al. 2012). On the other hand, fly ash from Brazilian coal is particularly more troubling given its reasonably high content of ash i.e., amid 30 and 50 wt. % (Flores et al. 2017, Pires,Querol 2005, Restrepo et al. 2015). Typical applications of fly ash such as raw and auxiliary material in the construction/cement industry (Giaccio,Malhotra 1988) or as partial substitute of clinkers in ordinary Portland cement (Siddique 2004, Sua-Iam,Makul 2015) are insufficient to balance the rising accumulation of fly ash, revealing the necessity to diversify the usage of fly ash in new applications. Additionally, the unemployed fly ash is currently disposed in land-fills and ash ponds

(Prasad,Mondal 2009, Gollakota et al. 2019) leading to environmental problems with public health consequences (Ahmaruzzaman 2010).

In regards to the control and reduction of the CO_2 emissions, Carbon Capture and Storage (CCS) have been considered as a potential technology to mitigate the global warming impact by the CO_2 released from coal/gas-fired power plants. This has motivated both governments and researchers towards the deployment of more efficient carbon capture processes from large emitting sources of CO_2 (Samanta et al. 2011, Liang et al. 2016, Nie et al. 2018). However, the high-energy penalty of the current capture processes is an unresolved issue that hinders the extensive use of CCS. Therefore, the main challenge of the current carbon capture systems is the development of improved CO_2 capture technologies with low energy demand for large scale applications (Huaman,Lourenco 2015, Kim et al. 2013).

CO_2 can be captured at industrial scale by post-combustion processes in power plants, also known as end-of-pipe technologies (Koytsoumpa et al. 2018, Liang et al. 2015). Chemical absorption with liquid amines might be the only post-combustion carbon capture process commercially available (Wu et al. 2014), though at the expense of an electricity cost penalty of up to 80% and the generation of toxic by-products (Kittel et al. 2009, Lockwood 2017). Adsorption-based carbon capture technologies are in constant evolution and may be considered as a more environmentally friendly method compared to liquid absorption (Grande et al. 2017). Adsorption separation processes required the use of adsorbents with suitable features (e.g., high CO_2 selectivity and adsorption working capacity, appropriate adsorption/desorption kinetics) with industrial scale availability and at low cost to be economically feasible (Plaza et al. 2017a, Songolzadeh et al. 2012). Zeolites have shown promising results to capture CO_2 from flue gas due to its high CO_2 adsorption capacities at low pressures (Modak,Jana 2019), which is driven by the reasonably large energetic dipole and quadrupole of CO_2 that strongly interacts with the electric field formed by the cations of the zeolites (Samanta et al. 2011). However, their CO_2 adsorption capacity might be impaired by the presence of water in the flue gas because of their sharp hydrophilic character (Wang,LeVan 2010). Due to their rich content in both aluminum and silicon, fly ash can be used as starting material to synthesize zeolites (Querol et al. 2002, Henmi 1987). Therefore, the usage of inexpensively available

fly ash from coal-fired power plants to obtain adsorbents for CO_2 capture might help diminish both the cost of carbon capture and the environmental hazards associated with fly ash disposal (Gollakota et al. 2019, Aquino et al. 2020).

In adsorption based CO_2 capture processes, the adsorbent is generally used in cycles by interchanging the stages of adsorption and desorption, where desorption is performed by either reducing the pressure (PSA) or increasing the temperature (TSA) (Grande et al. 2017). In a power plant where low pressure steam might be accessible, residual or waste heat could be used to recover CO_2 during the regeneration with TSA processes. Traditional fixed bed systems are difficult to be implemented in industrial scale due to the increased number of equipment necessary to cope with the large amount of flue gas and the time-consuming cycles limited by the long heating and cooling steps in TSA (Okumura et al. 2017, Plaza et al. 2017a). In light of the need to treat large volumes of flue gas continuously, it is essential to have minor units than those imposed by fixed bed configurations. Hence, the application of another type of solid - gas contactor, such as moving beds may be useful to surpass such limitation. A separation process consisting of a Moving Bed employing Temperature Swing Adsorption for the adsorbent regeneration (MBTSA) may be seen as a potential technology able to work in continuous operation and reduce the cost of energy demand in large-scale CO_2 capture by means of intelligent heat integration (Kim et al. 2013). Furthermore, an additional advantage moving beds offer is that pressure drop might not be troublesome for MBTSA technologies as it is for conventional fixed bed systems (Grande et al. 2017).

All things considered, the aim of this thesis is firstly to evaluate the potential use of both commercial and fly ash-based zeolites to capture CO_2 from flue gas under post-combustion scenario; and secondly, to assess, by numerical simulation, the performance of a Moving bed TSA process for CO_2 capture employing zeolites as adsorbent material. The study includes methodological phases as adsorbent characterization by gas adsorption and measurement of CO_2, N_2 and water vapor adsorption capacity by means of adsorption isotherms at different temperatures aiming at envisaging the performance of the synthesized adsorbents in a carbon capture process. These fundamental adsorption metrics along with the material characterization data, carried out for both the commercial and the synthesized samples, allowed us to both select

one of the adsorbents and provide input data for the simulation of a MBTSA pilot plant facility. Due to the significant number of design and operational variables playing roles in the MBTSA process, a parametric study though simulations was performed with the objective to evaluate the effectiveness of the MBTSA process by key performance parameters such as CO_2 recovery, purity, energy demand and productivity.

2. LITERATURE REVIEW

2.1. Carbon Capture & Storage (CCS)

Fossil fuels are still the dominant source of the world energy demand. Unfortunately, their combustion produces carbon dioxide (CO_2), which is regarded as one of the main promoters for climate change (Ben-Mansour et al. 2016). Different approaches have been pinpointed to be adopted worldwide aiming to decrease CO_2 emissions (Leung et al. 2014):

- The enhancement of energy efficiency and promotion of energy conservation mostly in commercial and industrial buildings where energy saving from 10% to 20% can be easily achievable.
- The increase of low carbon fuels usage such as natural gas, hydrogen or nuclear power. A cleaner fuel like natural gas emits 40 to 50% less CO_2 than coal because of its minor carbon content and greater combustion efficiency.
- The deployment of renewable energy including solar, wind, hydropower and bioenergy by the use of local natural resources, therefore avoiding the emissions of greenhouse and toxic gases.
- The application of geoengineering approaches, e.g. afforestation and reforestation as a simple method to generate natural and sustainable CO_2 sinks.
- CO_2 capture and storage (CCS).

Carbon Capture and Storage (CCS) is a process that involves, firstly, the separation of CO_2 from large sources of emissions (i.e., industrial and energy-related sources) and secondly, the transportation of CO_2 to a suitable storage location for a longstanding isolation from the atmosphere. The widespread application of CCS would depend on technical maturity, costs, diffusion and transfer of the technology to developing countries and their capacity to apply the technology, regulatory aspects, environmental issues and public perception (Davidson et al. 2005). CCS has the potential to reduce overall mitigation costs and increase flexibility in achieving greenhouse gas emission reductions. In an extensive review of the current status of CCS, Bui et al. (2018) emphasize on the crucial role that CCS plays in helping to meet the global warming goals

by Intergovernmental Panel on Climate Change (IPCC) and the Paris Agreement of the Conference of the Parties (COP21). The main objective is to assess different pathways towards limiting average global warming to less than 2 °C within this century. However, only a small number of the Intended Nationally Determine Contributions (INDCs), which countries promised at the climate negotiations in Paris, set CCS as a priority area. More specifically, a report on CCS by the International Energy Agency (IEA) in 2016 indicated that the progress of the past 20 years at the current rate is falling short of what is required to achieve climate goals. In addition, the deployment of large-scale CCS projects has been slow due to a variety of technical, economic and commercial challenges. It is estimated that of the 37 major large scale CCS projects, 17 of these are in operation, 4 in construction and the rest are in different stages of development (Bui et al. 2018).

2.2. Carbon Capture technologies

There are three technological pathways or scenarios that can be followed for CO_2 capture from power plants associated with different combustion processes (Figueroa et al. 2008, Leung et al. 2014): post-combustion capture, pre-combustion capture and oxyfuel combustion capture.

Post-combustion capture is an end-of-pipe process which involves the removal of CO_2 from flue gas coming from the power plant combustion chamber as shown in Figure 1 (Mondal et al. 2012). Post-combustion capture is in many aspects analogue to flue gas desulphurization (FGD), which is widely used to capture SO_2 from flue gas in coal and oil fired power plants. The separation of the CO_2 from other flue gases is necessary because the sequestration of all combustion gases is not feasible mainly due to the high cost of gas compression and storage (Olajire 2010). Additionally, post-combustion capture offers a substantial design challenge due to the low concentration of CO_2 in power-plant flue gas (typically 4 -15% vol.) and the large volume of gas has to be handled, which results in large equipment sizes and high capital costs (Olajire 2010, Ben-Mansour et al. 2016). However, the ease to retrofit post-combustion capture to the existing power plants without significant modifications in the technology of the plant makes post-combustion capture an attractive option for CO_2 capture. Moreover, its flexibility avoids undesirable shutdown

because its maintenance do not require stopping the power plant (Ben-Mansour et al. 2016).

Figure 1. Technological pathways to capture CO_2 from power plants

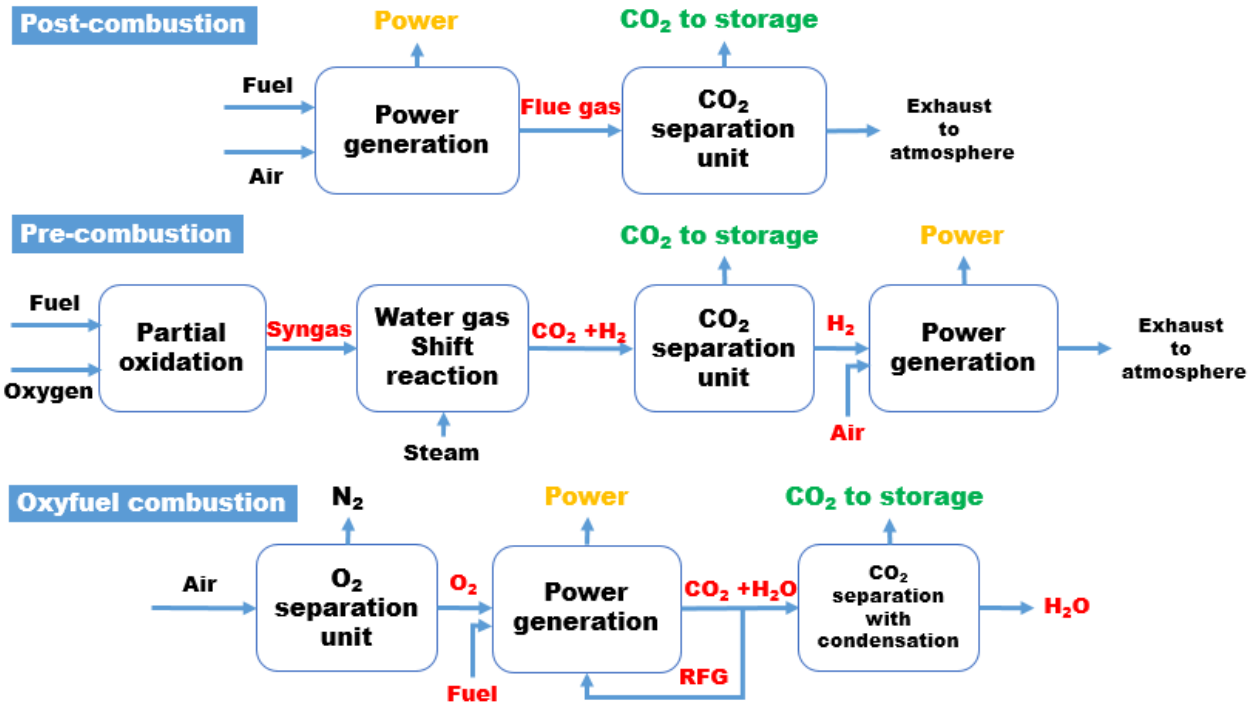

Source: Modified from Mondal et al. (2012)

In pre-combustion capture (Figure 1), fuel reacts with oxygen or air to yield mostly CO and H_2 (syngas) in a process known as gasification, partial oxidation or reforming. The syngas goes through a catalytic reactor, called a shift converter, where the CO reacts with steam to produce CO_2 and more H_2. The CO_2 is then separated and the H_2 is used as fuel in a gas turbine combined-cycle plant. The main advantage of pre-combustion capture relies on the higher partial pressure of CO_2 in comparison with post-combustion, which enables the use of smaller units for the separation process. Another profit of pre-combustion is the production of a carbonless fuel as Hydrogen, whose combustion does not emit SO_2. Nevertheless, the main shortcoming regarding pre-combustion capture is the requirement of a chemical plant ahead of the turbine. Complex chemical processes may eventually cause extra shutdowns of the plant, resulting in a minor power output (Mondal et al. 2012).

Oxyfuel combustion is essentially a modified version of post-combustion capture, where fuel is burned in almost pure oxygen in replacement for air, which results in a high concentration of CO_2 in the flue gas (over 80% vol. in flue gas). The combustion of fuel in pure oxygen leads to an exceptionally high flame temperature, requiring that some CO_2-rich flue gas (RFG) (see Figure 1) be recycled to the combustor to make the flame temperature akin to that in normal air-blown combustor. The advantages of oxyfuel combustion include the avoidance of NOx formation, the use of simple physical separation processes for O_2 production and CO_2 capture; thus, eluding the use of any solvent that can contribute to operating costs and environmental discarding of any related solid or liquid waste. The main weakness of oxyfuel combustion is the need of a great amount of oxygen, which is expensive both in terms of capital cost and in energy consumption (Olajire 2010).

2.3. CO_2 separation processes

Several processes are available for CO_2 separation and these include physical and chemical absorption, adsorption, membrane and cryogenics as illustrated in Figure 2.

Figure 2. Different CO_2 separation processes

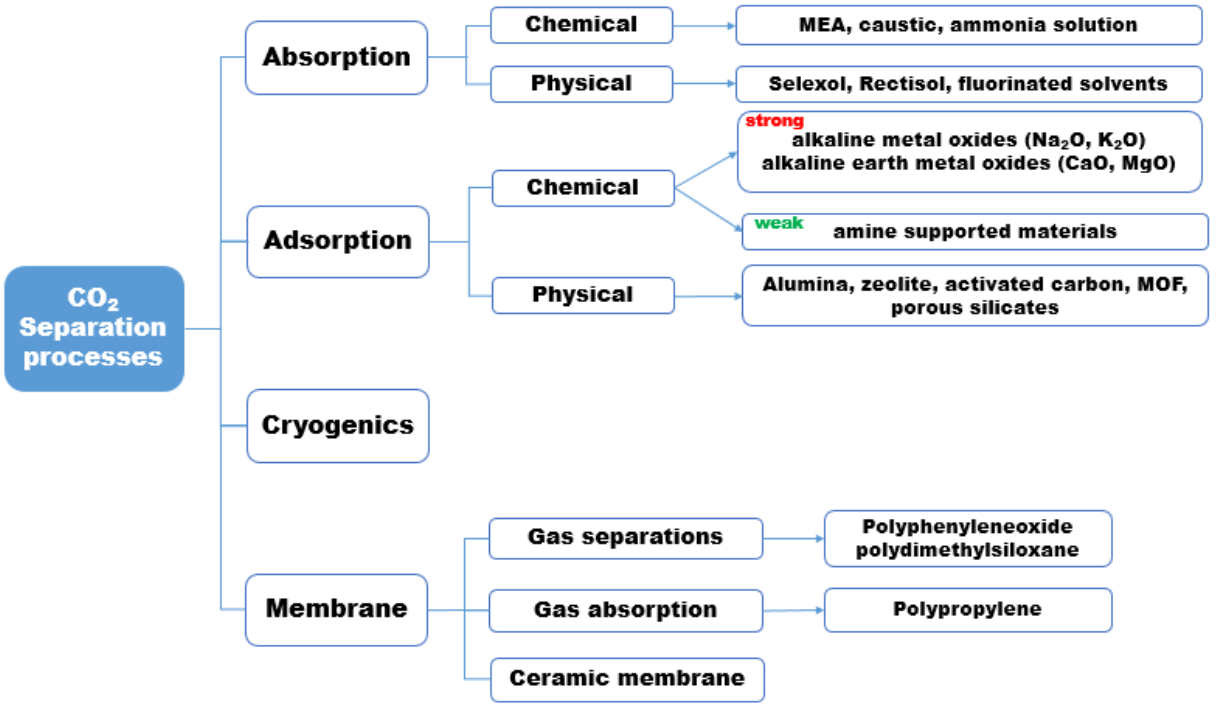

Source: Modified from (Songolzadeh et al. (2014), Thiruvenkatachari et al. (2009))

Since a wide range of technologies currently exist for the separation of CO_2 from flue gas, the choice of a suitable technology depends on the characteristics of the flue gas stream, which depend mainly on the power-plant technology (Olajire 2010). These techniques are briefly described below with the exception of adsorption separation process that will be further explained in greater depth in accordance with this research interest.

Chemical or physical absorption processes are widely used in the petroleum, natural gas and coal power plants, as well as in chemical industries for CO_2 separation. In this method (Figure 3), the absorber (absorption vessel) and regenerator (desorption vessel) operate continuously. A CO_2-containing flue gas stream is introduced into the bottom of the absorber. The absorbent is introduced from the top of the column, which leads to countercurrent contact between the flue gas and the solvent and selective CO_2 absorption takes place. The CO_2-rich stream is then fed to the regenerator, where CO_2 desorption occurs and the regenerated solvent is recycled for later use. The desorbed CO_2 is then compressed and sent to storage (Mondal et al. 2012). Previous studies have suggested that amine-based CO_2 absorption systems are the most suitable and common for combustion power plants (Rubin,Rao 2002, Ma'mun et al. 2007). Particularly for the post-combustion context, chemical absorption is a more appropriate option than physical absorption due to the low concentration of CO_2 in the flue gas near atmospheric pressure (Bhattacharyya,Miller 2017). Amine-based separation systems are the most widely used for the chemical absorption of CO_2, and MEA (monoethanolamine) is the most viable absorbent for the CO_2 capture from coal-fired power plants (Chu et al. 2016). MEA is very reactive with CO_2 and is considered as the reference solvent in amine-based CO_2 scrubbing processes; therefore, most studies focus mainly on assessing process modification/optimization for MEA solvent (Le Moullec et al. 2014).

Figure 3. Graphical representation of absorption, membrane and cryogenic separation processes

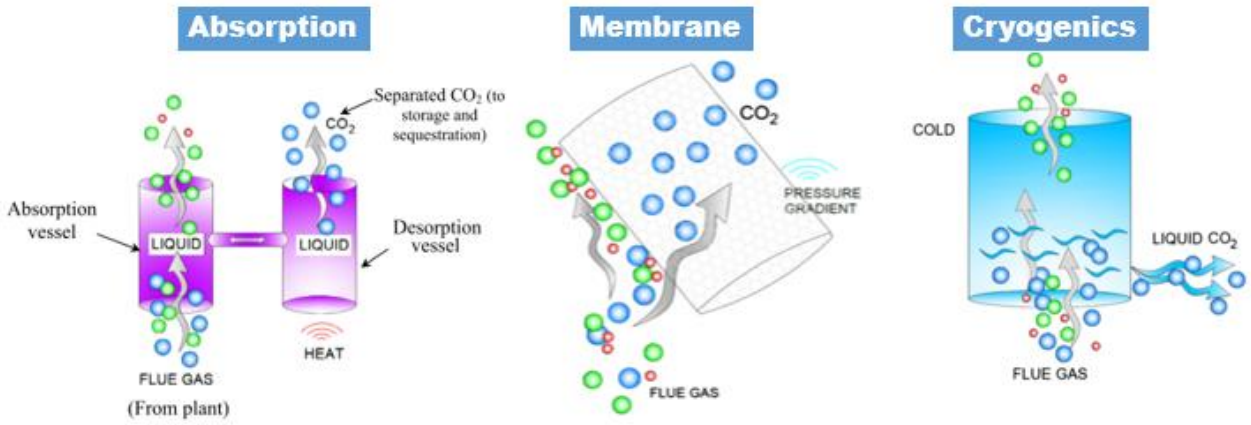

Source: Modified from Ben-Mansour et al. (2016)

Owed to its low-cost and ease of production, MEA has been used industrially for more than five decades and its use in CO_2 absorption is considered a state-of-the-art process with operating conditions between 20% and 30% (by mass) of aqueous MEA and an inlet temperature of approximately 40 °C. With regards to the capture process configuration, a standard process of a 30 wt.% MEA may require a thermal energy duty around 3.6–3.7 MJ/kg CO_2; however, thanks to improved solvent formulations, advanced process configurations and the introduction of heat integration, the thermal energy consumption values have decreased to 3.2–3.6 MJ/kg CO_2 (Sanchez Fernandez et al. 2014). Despite its high reactivity with CO_2, MEA absorption systems still faces various challenges, namely high energy consumption for solvent regeneration, poor thermal stability, and high corrosivity (Liang et al. 2016).

Membranes are selective materials that can be used to allow only CO_2 to pass through them while rejecting other components of the flue gas (Leung et al. 2014), as displayed in Figure 3. Membranes are made from polymer or ceramic materials and their configurations can be specially designed for CO_2 selectivity (Ben-Mansour et al. 2016). A number of issues limit the use of membranes for CO_2 capture especially in post-combustion context where the concentration of CO_2 is low so that large volumes of flue gas will require to be processed. Their application still needs to be demonstrated at large scale and over relevant timescales of operation under realistic conditions to confirm if they are able to preserve their selectivity in different gas environments. Furthermore, problems

related to membrane sealing and failure require special attention as well. Organic membranes are not suitable to operate at relatively high temperatures, which implies that an upstream cooling step for the flue gas is required; thus, reducing the application to inorganic membranes only (Bui et al. 2018). Additionally, creating a pressure difference through the membrane will require a substantial extent of power, which might decrease the thermal efficiency of the power plant (Brunetti et al. 2015).

Cryogenic capture process involves compression and cooling of the gas mixtures in several stages to induce phase changes of CO_2 in flue gases and invariably other components present in the mixture as shown in Figure 3. Depending on the operating conditions, the CO_2 can arise as a solid or liquid together with other components from which it can be distilled (Mondal et al. 2012). Cryogenic CO_2 capture techniques can perform carbon capture without the energy penalty of solvent regeneration and pressure drop generation. However, the cryogenic process covers a large range of operating condition from normal to supercritical state (Song et al. 2012). For that reason, the major shortcoming of cryogenics is the large amount of energy required to provide the refrigeration (Songolzadeh et al. 2014). Cryogenic application is more suitable to CO_2 capture where the gas stream contains high CO_2 concentrations e.g., in oxy-fuel combustion or CO_2 capture from exhaust of the cement industry. It is currently not applied to more dilute CO_2 streams such as those encountered in post-combustion capture (Thiruvenkatachari et al. 2009).

2.4. CO_2 capture by adsorption

2.4.1. General overview of adsorption

Adsorption processes are of great technological importance, i.e., some adsorbents are employed on a large scale as desiccants, catalysts or catalyst supports. The diversity of the adsorption applications are not only limited to the separation or storage of gases and purification of liquids but also to other areas including controlled drug delivery, pollution control or respiratory protection (Rouquerol et al. 2014). In the field of CO_2 capture, adsorption-based separations are still in the process of consolidation and

require greater efforts to become widely commercially available. By definition, adsorption is considered as the enrichment of material or increase in the density of the fluid in the vicinity of an interface (Rouquerol et al. 2014, Thommes et al. 2015). Adsorption is an exothermic phenomenon occurring whenever a solid surface is exposed to a fluid. The solid is called the adsorbent and the gas or liquid, which is capable of being adsorbed, is called the adsorptive. The fluid in the adsorbed state is called adsorbate (Lowell et al. 2006). Adsorption can be classified into two main categories: physical (physisorption) or chemical (chemisorption) (Ruthven 1984). The main difference between these two categories is the type of forces involved in the adsorbate-adsorbent interactions. While intermolecular forces between the adsorbate and adsorbent govern physical adsorption, chemisorption implies the formation of new chemical bonds. The specific molecular interactions found in physisorption (e.g., polarization, field-dipole, field gradient quadrupole) typically occur as a result of particular geometric and electronic properties of the adsorbent and the adsorptive (Thommes et al. 2015). Some of the physical properties of adsorbates of interest are presented in Table 1. These properties can shed light on which gas molecule from a particular gas mixture may adsorb preferentially in a given surface, e.g., the dipole moment forms a stronger interaction than the quadrupole moment, meaning that H_2O will adsorb to a given surface more strongly than CO_2 (Danaci et al. 2020).

Table 1. Physical properties of selected gases

Gas	Kinetic diameter (Á)	Polarizability ($x10^{-25}$ cm^3)	Dipole moment ($x10^{18}$ esu cm)	Quadrupole moment ($x10^{-26}$ esu cm^2)
H_2	2.89	8.0	0	0.662
N_2	3.80	17.6	0	1.52
Ar	3.54	16.4	0	0
CO_2	3.3	26.5	0	4.30
H_2O	2.64	14.5	1.87	-
H_2S	3.623	37.8	1.0	-

Source: data taken from Sircar (2006)

Another typical example is that of CO_2/N_2 separations, where the greater quadrupole moment of CO_2 explains the preferential adsorption of CO_2 over N_2 on the adsorbent surface. In cases where the pore window of the adsorbent is smaller than the kinetic diameter of a component in the gas mixture, the mixture can be sieved molecularly

(Hedin et al. 2013). On the other hand, chemisorption is often defined as ‘specific’ since a certain adsorbate will only react with a specific site; for instance, in the case of post-combustion capture, CO_2 will form a bond with $–NH_2$ functional groups, nevertheless N_2 will not (Webley,Danaci 2020).

2.4.2. Adsorption isotherm modeling

Despite the countless existing adsorption isotherm models, the derivation of the different isotherm models may be classified in terms of three fundamental approaches: kinetic, thermodynamic and potential theory (Malek,Farooq 1996). The first coherent proposal for adsorption on a flat surface was proposed by Langmuir (1918). Langmuir theory is based on a kinetic principle, that is the rate of adsorption is equal to the rate of desorption from the surface (Do 1998). The most known thermodynamic based isotherm is the Gibbs adsorption isotherm and the third approach is based on the potential theory of the gas adsorption proposed by Dubinin (1960). Some isotherm models such as the Langmuir isotherm can be derived using more than one approach, therefore leading to a difference in the physical interpretation of the model parameters (Malek,Farooq 1996). In some cases, one approach can result in a physically more meaningful model than the others (Ruthven 1984).

2.4.2.1. Empirical models

The Freundlich equation (1932) is one of the first empirical equations used to represent equilibrium data. The Freundlich isotherm is commonly used in the description of adsorption of organics from aqueous streams onto activated carbon. It is equally applicable in gas phase systems having heterogeneous surfaces, in cases where the range of pressure is not too wide, as this isotherm equation does not have neither a proper Henry law behavior at low pressure nor a finite limit when pressure is sufficiently high (Do 1998). Sips model, also known as the Langmuir-Freundlich model, is likely to describe heterogeneous surfaces much better than Langmuir isotherm (Sips 1948). At low pressures, it reduces to a Freundlich isotherm; yet, at high pressures, the Sips model

predicts the monolayer capacity representative of the Langmuir isotherm. Toth (1971) proposed another empirical isotherm model to improve Langmuir isotherm fittings. The main advantage of the Toth isotherm is its ability to describe heterogeneous adsorption systems with thermodynamic consistency at both the low and the high-end boundary of the concentration (Foo,Hameed 2010). Both Sips and Toth isotherms are popular adsorption isotherm equations because of their ability to model a wide variety of equilibrium data (Malek,Farooq 1996). The equation forms of the most common adsorption models are presented in Table 2.

Table 2. Common models for adsorption isotherms

Isotherm	Single component form	Direct multicomponent extension
Langmuir	$\frac{q_e}{q_{max}} = \frac{bP}{1+bP}$	$\left(\frac{q_e}{q_{max}}\right)_i = \frac{b_i P_i}{1+\sum_{j=1}^{NoC} b_j P_j}$ *j=1,2,…,N.*
Freundlich	$q_e = bP^{1/n}$	Not applicable
Sips	$\frac{q_e}{q_{max}} = \frac{(bP)^{1/n}}{1+(bP)^{1/n}}$	$\left(\frac{q_e}{q_{max}}\right)_i = \frac{(b_i P_i)^{1/n_i}}{1+\sum_{j=1}^{NoC}(b_j P_j)^{1/n_j}}$ *j=1,2,…,NoC.*
Toth	$\frac{q_e}{q_{max}} = \frac{bP}{[1+(bP)^n]^{1/n}}$	Not applicable

Source: own authorship

The most popular approaches for multicomponent equilibrium are the direct extension of the monocomponent isotherm models and the ideal adsorbed solution theory (IAST) proposed by Myers and Prausnitz (1965). The IAST is a general theory that attempts to predict multicomponent adsorption from any functional form of the pure component isotherm model. The principal disadvantage of IAST multicomponent equilibrium approach is the greater computational requirement in comparison with direct extensions of the pure component isotherms. This is particularly true for isotherm models such as Sips and Toth, where the Gibbs equations for spreading pressure cannot be

integrated analytically. Conversely, owed to the model simplicity, the Langmuir isotherm allows an analytical solution to the Gibbs integral; thus, reducing computational requirements substantially (Malek,Farooq 1996).

2.4.3. Contextualization of post-combustion capture in CO_2 separation by adsorption

Three decisions are crucial at planning any separation process by adsorption. The first decision is related to the selection of the adsorbent material, the second to the regeneration strategy to clean and reuse the adsorbent and the third, the type of contactor/reactor at which the adsorption process will take place. Figure 4 illustrates some of the possible choices available to structure a CO_2 separation project by adsorption.

Figure 4. CO_2 separation process by adsorption

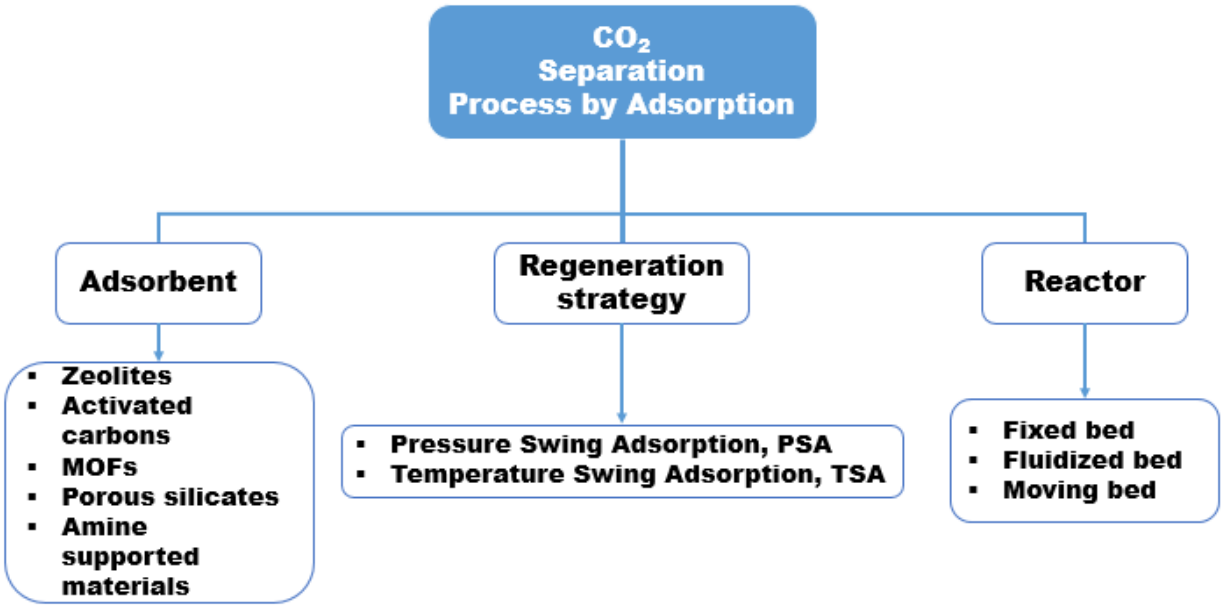

Source: own authorship

Typical flue gas composition from a coal-fired plant has a relatively low CO_2 concentration (14-16% vol.), while most of the effluent is composed of N_2 (73-78% vol.) and other smaller components, such as H_2O (5-7% vol.), O_2 (3-4% vol.), CO, NOx and SOx (ppm). The low partial pressure of CO_2 in the flue gas and the diversity of components

of the gas mixture highlights the need for adsorbent materials with high affinity for CO_2, so that mostly CO_2 is captured and subjected to permanent storage or use (Bahamon,Vega 2016). Besides selectivity, other key features include high CO_2 adsorption capacity, adequate adsorption/desorption kinetics and good thermal and mechanical stability after several adsorption/desorption cycles. Adsorbents, which could be applied to CO_2 capture include activated carbons, carbon fibers, silica gel, ion exchange resins, zeolites and porous silicates (SBA-15, MCM-41, etc.), activated alumina, metal oxides (CaO , MgO, K_2O, Li_2O), metal-organic structures (MOFs), hybrid organic-inorganic adsorbents and other surface-modified porous media (Songolzadeh et al. 2012). However, this diversity of adsorbents must be narrowed down to those with adequate characteristics and availability in tonnage quantities and at low cost (Plaza et al. 2017a). In general, zeolites can meet the above specifications. Among the different types of zeolites, zeolite 13X has been suggested as a promising adsorbent for the separation of CO_2 from flue gas especially at dried conditions (Bahamon,Vega 2016, Harlick,Tezel 2004).

The second decision in the design of adsorption processes involves determining the regeneration strategy that should be applied to the adsorbent, which will depend on economic and technical considerations. The adsorbent can be degassed or regenerated by either Pressure Swing Adsorption (decreasing the system pressure) or Temperature Swing Adsorption (increasing the system temperature). In a power plant, the availability of low pressure steam and waste heat, which could be used to heat the adsorbent in the degassing step, paves the way for Temperature Swing Adsorption (TSA) processes (Plaza et al. 2017a).

The third decision is the type of solid - gas contactor to be applied in the CO_2 capture system. Fixed bed columns working in TSA cycles can take hours due to the time-consuming cycles limited by the long heating and cooling steps (Plaza et al. 2017a). In addition, fixed bed systems are difficult to be implemented in industrial scale due to the increased number of reactors and equipment required to treat the large amount of flue gas (Okumura et al. 2017). In view of the necessity to treat large volumes continuously, it is vital to have smaller units than those imposed by fixed bed systems. Thus, fluidized bed or moving bed may be potential alternatives. The choice of any of the preceding options

can be somewhat confusing since the type of reactor does not seem to hinge on the sorption mechanism or the type of adsorbent according to Kim et al. (2014). Their investigation also suggested that both fluidized and moving beds could eventually be a less expensive alternative as compared to amine absorption especially if there is heat integration during the desorption process. Therefore, the Moving Bed Temperature Swing Adsorption (MBTSA) process is being considered as a potential technology to reduce the cost of energy demand in large-scale CO_2 capture by means of intelligent heat integration, which is not easy to achieve with circulating fluidized bed or bubbling processes (Kim et al. 2013).

2.4.4. Zeolites

Zeolites can occur naturally in alkaline environments of sediments and volcanic materials under particular hydrothermal and geological conditions. However, although many of these materials might have valuable properties as adsorbents and even as catalysts, the natural forms regularly exhibit defects and irregularities mainly due to the contamination by other minerals, metals, quartz, or other zeolite structures that limit their industrial application (Chester,Derouane 2009, Bingre et al. 2018). Nevertheless, with the deployment of the laboratory methods for the synthesis of zeolites, applications of zeolites at commercial level had a rapid growth. (Chester,Derouane 2009).

Zeolite's framework is made up of tetrahedral atoms bound with oxygen (TO_4), generally $[SiO4]^{4-}$ or $[AlO4]^{5-}$. Zeolites are crystalline microporous materials containing pores of molecular size (Bingre et al. 2018). The micropore structure of zeolites is determined by the crystal lattice and is uniform with no pore size distribution distinguishing zeolites from other microporous adsorbents (Ruthven 1984). Moreover, the presence of water and cations (generally alkalis and alkaline earths) allows the compensation of the negative charges generated by the presence of Al, giving birth to the general formula:

$$M^{n+}{}_{x/n}\left[(AlO_2)_x(SiO_2)_y\right].zH_2O$$

with M^{n+} as the compensation cation (e.g., Na+), *y/x* the Si/Al ratio, and *z* the number of molecules of water. According to the Löewenstein's rule Al-O-Al linkages are not allowed and, hence, Si/Al is always at least the unity (Bingre et al. 2018).

Zeolites are frequently called as molecular sieves especially when an appropriate framework can act as sieve at molecular level to separate molecules of a given gas mixture. This is possible owed to the well-defined pore size of zeolites that can trap larger molecules and let pass through the pores the smaller ones. Additionally, the chemistry of zeolites results in them being typically sensitive to the presence of impurities and water vapor, as these compounds can adsorb more strongly to the surface than CO_2 and are also problematic to remove (Webley,Danaci 2020).

2.4.4.1. Fly ash-based zeolites for CO_2 capture

Fly ashes are a solid residue, which represents between 60 to 90 % of the total combustion residues from coal-fired power plants (Dindi et al. 2019). Given the high content of Al and Si, the use of fly ash from coal power plants as starting material to obtain adsorbents for CO_2 capture might help reduce the cost of carbon capture while reducing the environmental risks related to fly ash discarding. An additional advantage of using fly ash is the fact that it is produced in the coal power plants and can, consequently, be straightforwardly applied onsite (Gollakota et al. 2019).

Several works have already addressed the synthesis and/or characterization of zeolites from fly ash for different purposes (Izidoro et al. 2012, Yang et al. 2019, Tauanov et al. 2018, Murayama et al. 2002, Iqbal et al. 2019, Deng et al. 2016, Belviso 2018b, Fukasawa et al. 2018, Fukasawa et al. 2017). In the CO_2 capture field, some studies have reported the pure CO_2 adsorption capacity of fly ash zeolites at atmospheric pressure by thermogravimetric analysis but only at 25 °C (Zhang et al. 2017b, Soe et al. 2016, Bukalak et al. 2013), a lower value of temperature than the expected (between 40 and 60°C) for the flue gas stream in post-combustion scenario (Bae et al. 2013, Bhown,Freeman 2011). Majchrzak-Kucęba and Nowak (2005) also applied thermogravimetric method to obtain CO_2 sorption data for different synthesized zeolites, but using a mixture of gases closer to post-combustion scenario i.e., CO_2 (10 % v/v), N_2 (80 % v/v) and O_2 (10 % v/v) at three different temperatures (25, 75, 150 °C). Lee and Jo (2010) obtained the CO_2 adsorption capacity for synthesized Na-P1 and Na-A zeolite via breakthrough curves, however for low CO_2 concentration levels (3000 ppm of CO_2), a

concentration frequently observed in domestic indoor spaces. Zgureva (2016) performed CO_2 and N_2 adsorption isotherms of synthesized zeolites measured at 0 °C and obtained a maximum adsorption capacity of 136 mg/g with the FAU (zeolite X) synthesized from fly ash. The fly ash zeolite exhibited a CO_2 selectivity of around 23–36 at 273.15 K with respect to the nitrogen. Liu et al. (2011) reported the performance of a mixture of A and X zeolites synthesized from fly ash in a Vacuum Swing Adsorption (VSA) process. Their findings indicated that zeolite A+X mixture was able to displayed a superior performance in CO_2 capture in a VSA process at 90°C when compared with 13X zeolites due to higher selectivity of CO_2 over N_2 of the mixed fly ash-based zeolite.

2.4.5. Moving Beds for CO_2 capture

Berg (1951) pioneered the commercial application of the moving bed concept by his so-called “Hypersorption” process, originally conceived for the recovery of volatile and dilute gases in the chemical and petroleum industry. The process employed a moving bed of activated carbon to adsorb and fractionate volatile hydrocarbons. The continuous moving bed was able to perform separation and recovery of light gases, which were formerly considered to be uneconomical. Late in the 80s, Storti et al. (1988) established a comparison between a counter current True Moving Bed and a Simulated Moving Bed (SMB). The True Moving bed, a “sorbex” type, was used as a comparative tool to optimize the SMB design and operation for xylene isomer separation in vapor phase on Y zeolite employing isopropyl benzene as desorbent. In the carbon capture context, Knaebel (2013) patented a TSA system using adsorbent in a moving bed to separate CO_2 from flue gas of coal-fired power plants, cement factories and other similar processes. The multi-step moving bed, known as “ARI moving bed”, was designed aiming at minimal external energetic requirement by using the heat contained in the flue gas to desorb CO_2 from the solid material. The problem of attrition, previously observed in countercurrent moving beds based on the Hypersoption invention, was addressed by the introduction of perforated plates at relatively short vertical intervals to distribute the normal force and avoid its accumulation in a column of moving adsorbent.

Literature on moving bed contactors for post-combustion CO_2 capture systems is sparse but of growing interest. Some authors have addressed the modeling of MBTSA process for carbon capture in post-combustion context. Most of them have employed zeolite 13X as adsorbent due to the availability of reliable kinetic and equilibrium parameters, yet some other materials such as activated carbons and amine-impregnated adsorbents have also been reported. Kim et al. (2013) investigated a moving bed adsorption process with heat integration using zeolite 13X. The modeled MBTSA process was able to reach 57% of the degree of thermal integration (i.e., the percentage of reused thermal energy through heat integration over the total energy required), while producing CO_2 in purity and recovery of 97% and 80%, respectively. Pilot-scale moving bed tests for CO_2 capture using porous materials impregnated with amine applying low temperature steam (60 °C) for the regeneration have been published as well (Okumura et al. 2014). The moving bed tests, which were merely experimental, aimed to establish a scale-up method that might be used for commercial purposes. The results indicated that using the relation between the residence time of the adsorbent material and the CO_2 adsorption loading, the capacity, the amount of circulation of the material as well as the design values for a moving bed adsorption reactor can be determined (Okumura et al. 2017). Mondino et al. (2017) evaluated a MBTSA process in post-combustion coal-fired power plant using activated carbon. One of the main conclusions of their work was the need to recirculate some fraction of the rich CO_2 product stream to the incoming flue gas in order to achieve purity and capture rates around 97 and 85%, respectively, given the nature of the adsorbent tested. Both the high porosity and relatively low CO_2/N_2 selectivity of the activated carbon lead to a relatively large amount of adsorbed nitrogen. Regarding the energy demand of the process, no estimation on this issue was carried out in that study. Grande et al. (2017) compared key performance parameters between the MBTSA and MEA absorption process. The MBTSA for CO_2 capture, based on ARI technology, was studied by modeling a natural gas combined cycle (NGCC) context using zeolite 13X as adsorbent. For regeneration, a flue gas at 222 °C was used, obtaining a specific energy demand for the MBTSA process of 2.3 MJ kg^{-1} of CO_2 captured, while MEA absorption required 4.0 MJ kg^{-1} of CO_2. Later, Mondino et al. (2019) proposed a more robust model aiming to propose a more in-depth assessment of the performance of this process. In this

case, unlike the previous work, the source of heat for the adsorbent regeneration was no longer the flue gas itself but steam from the power plant. The performance parameters obtained for an inlet temperature of 30 °C suggested that increasing the regeneration temperature leads to better performance both in terms of CO_2 purity and recovery. At 180 °C, the CO_2 purity and recovery were estimated at 95.1% and 96.0%, respectively. At 207 °C, the performance parameters went up to 98.8% for purity and 98.2% for recovery. More recently, Mondino et al. (2021) published some initial tests of a lab-scale MBTSA with indirect heating and a feed CO_2 concentration of 5% vol. aiming at assessing various low temperature solid adsorbents (e.g., activated carbon) for CO_2 capture. Although the functionality of the experimental setup showed stable continuous operation, some modification in the rig are required to obtain target performance output in terms of CO_2 recovery and purity, which are not yet optimized. A fraction from both CO_2 enriched gas stream from both the regenerator and the cooling section have been proposed to be recycled so that enhanced CO_2 capture rate and purity of the product stream might be achieved.

3. EXPERIMENTAL

3.1. Materials

3.1.1. Gases and liquids

The main gaseous adsorbates for the adsorption measurements were helium (White Martins Praxair, Inc., São Paulo, Brazil, 99.999%), carbon dioxide (White Martins Praxair, 99.8%), and nitrogen (White Martins Praxair, 99.999%). Helium was used for calibration procedures and to determine the specific volume of the adsorbent solid phase. Distilled water was employed for water vapor adsorption isotherms.

3.1.2. Adsorbents

The commercial adsorbents used in this work were type 13X Zeolite (Zeo13X) from Shangai Hengye Chemical Industry and type 4A Zeolite (Zeo4A) from Zeochem. On the other hand, the synthesized adsorbents were prepared from coal fly ash of two different power plants located in Brazil. The fly ash samples were collected from electrostatic precipitators. Type X zeolite (XFF) was synthesized from fly ash of Jorge Lacerda Power plant (Brazil) and type A zeolite (PAF) was synthesized from fly ash of Pecém II Power plant (Brazil). The commercial adsorbents are in bead form of 2 mm while the synthesized samples were provided in powder form (no binder).

3.2. Methodology

The zeolite synthesis of the samples were performed at the laboratory facility of the *Centro Tecnologico* by the research team of Associação Beneficente da Indústria Carbonífera de Santa Catarina (SATC), in Criciúma, SC, Brazil. The team of SATC kindly provided the prepared samples along with the commercial samples to be employed in this thesis. Although the study and/or optimization of the synthesis of the zeolites from fly ash escapes from the scope of this work, in section 3.2.1., information regarding the zeolite synthesis and the chemical/mineralogical characteristics of the prepared samples is provided.

The main methodological steps of this thesis can be summarized in Figure 5. All of the three steps that comprises this work were carried out at our laboratory: *Laboratório de Pesquisa de Adsorção e Captura de CO_2* (LPACO2). Additionally, LPACO2 is a member of the research group *Grupo de Pesquisa em Separações por Adsorção* (GPSA) at Federal University of Ceará (UFC) located in Fortaleza, CE, Brazil.

Figure 5. Sequencial methodological flowchart

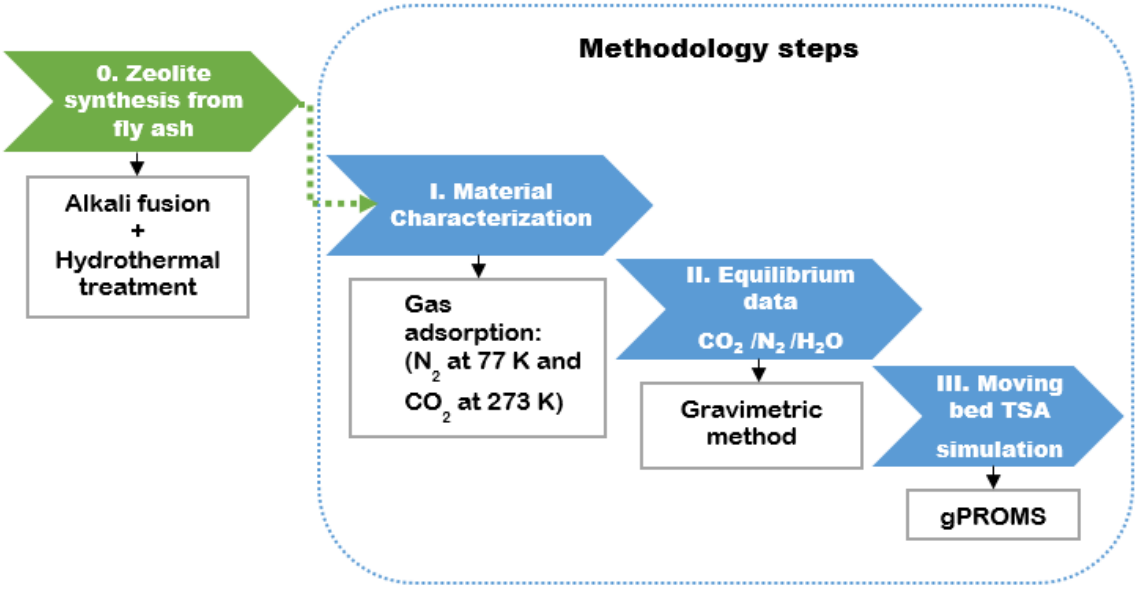

Source: own authorship

3.2.1. Zeolite synthesis from fly ash

The main consecutive steps for the synthesis of the zeolites are shown in Figure 6. The preparation procedure was based on the work of Izidoro et al. (2013) and Aquino (2018). Firstly, the fly ash samples are dried in an oven at 105 °C for 24 h. Afterwards, the dried coal fly ashes are mixed with sodium hydroxide (NaOH) to undergo a melting stage at 550 °C for 1 h. The fly ash-NaOH mixture ratio was defined according to the required SiO_2/Al_2O_3 ratios to obtain each type of zeolite. For the fine-tuning of the SiO_2/Al_2O_3 ratios, chemical and mineralogical essays of the fly ashes were performed and only the amorphous contents of these elements were taken into consideration. The desired molar ratio ranges for the synthesis of type X zeolites are: SiO_2/Al_2O_3

= 2 – 3; Na_2O/SiO_2 = 1.2 – 1.5; H_2O/Na_2O = 40 – 60 and those for type A zeolites are: SiO_2/Al_2O_3 = 1 – 2.5; Na_2O/SiO_2 = 0.8 – 3 and H_2O/Na_2O = 40 – 120 (BRECK, 1974).

After the melting step, the sample is cooled down to room temperature and crushed with the aid of a pistil and mortar. Prior to the stirring step, the melted and pulverized material is aggregated to the aluminum source (sodium aluminate) and water according to the desired SiO_2/Al_2O_3 ratio. Sample stirring is performed on a Teflon beaker under magnetic stirring with an average speed of 300 rpm. For type X zeolites the procedure is performed during 16 h at room temperature whereas for type A zeolites, the stirring time is reduced to 1 h at a higher temperature (50 °C). Once homogenization is completed, the mixture is poured inside the hydrothermal reactor, which has 0.5 L of internal volume.

Figure 6. Fly ash based zeolites synthesis route

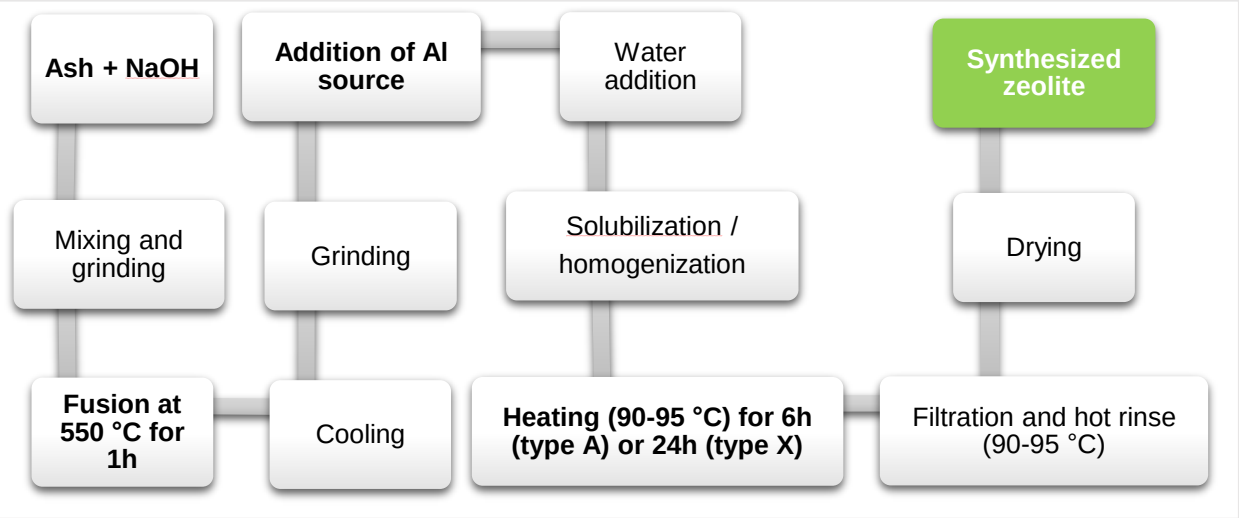

Source:modified from (Aquino et al. 2020)

The customary hydrothermal reaction time is 24 h for type X zeolites and 6 h for type A zeolites while the reaction temperature should remain between 90 and 95 °C. It is worth mentioning that an appropriate temperature control is key to prevent the formation of other type of zeolites (Sun et al. 2008, Melo et al. 2012). The internal temperature control of the solution was carried out by means of a PT100 thermal sensor, and the temperature continuously monitored and recorded by the Logchart software. Once the hydrothermal reaction time is attained, the solution is filtered under vacuum and subsequently hot washed. Distilled water at the same synthesis temperature is employed to wash the prepared sample with a volume of about 10 times the total volume of solids used for the synthesis. After filtration, the synthesized sample is oven

dried at 105 °C for 24 h. Both of the zeolites obtained are in powder form with particles sizes under 68 µm. The amount of type X zeolites produced was 20 to 30 % higher than the amount of fly ash used for the synthesis whereas for type A zeolites, the yielded product was even higher, around 30 to 40 %. The reproducibility of the synthesis procedure was also verified by producing both zeolites in a larger scale using a 3 L hydrothermal reactor.

3.2.1.1. Chemical, mineralogic and microscopic characterization analyses

Initially, the ignition loss test (LOI) is required, following the ASTM D7348-07 standard, in order to eliminate organic materials and water present in the samples. After performing the LOI, the samples are ground and pressed into tablets for further chemical analysis. The identification of the major elements constituting the fly ash, on both the prepared and commercial samples, was performed with the aid of a PW2400 X-ray Fluorescence (XRF) spectrometer of Philips.

The major element compositions (wt. %) obtained by the XRF essay performed on the fly ash are presented in Table 3. As one can observe in Table 3, the two fly ash precursors are mostly composed of SiO_2 and Al_2O_3 (i.e., > 70%), which suggests the potential of these materials to synthesize zeolites.

Table 3. Chemical composition of the fly ash used for the zeolite synthesis

Composition (wt. %)	Jorge Lacerda Ash	Pecém Ash
SiO_2	60.76	49.96
Al_2O_3	25.48	21.14
Na_2O	0.56	1.85
Fe_2O_3	5.00	8.66
MgO	0.79	3.33
CaO	1.54	6.73
TiO_2	1.11	0.86
K_2O	2.91	1.80
SO_3	0.47	1.61
P_2O_5	0.07	0.14
LOI	1.33	3.95

Source: Morales-Ospino et al. (2020)

Table 4. Chemical composition of the commercial and synthesized zeolites by XRF

Composition (wt. %)	Zeo13X	XFF	Zeo4A	PAF
SiO_2	43.33	39.64	48.95	35.02
Al_2O_3	21.44	22.35	27.39	23.39

Na_2O	7.39	7.84	9.18	8.24
Fe_2O_3	1.71	6.11	1.67	7.76
CaO	0.72	1.87	2.26	3.46
K_2O	0.80	1.25	1.04	0.77
LOI	22.94	19.18	7.20	19.48
SiO_2/Al_2O_3 (wt.%)	2.02	1.77	1.79	1.50

Source: Morales-Ospino et al. (2020)

Likewise, the chemical composition of the commercial and the synthesized zeolites was determined by XRF as shown in Table 4. The main constituents of the zeolites in oxide form, including the loss on ignition (LOI) percentage and the SiO_2/Al_2O_3 ratio, are summarized in Table 4. SiO_2/Al_2O_3 ratios of the commercial zeolites turned out to be slightly higher than those of the synthesized samples.

X-ray Diffraction (XRD) was used to detect the mineralogical compositions of crystalline phases of the zeolites by means of a LabX XRD-6100 automated diffractometer (Shimadzu). Samples are required to be in powder form to run this experimental essay. The equipment detector analyzes the diffraction generated by the material and identifies the crystalline phase generating an intensity graph, which allows the comparison of the acquired peaks with standardized data. The phase identification of the mineralogical data was made by matching the diffractograms of the samples against the PDF databases of ICDD (International Center for Diffraction Data, 2003) and COD (Crystallography Open Database, 2016) using Match!3 software.

From the X-ray diffraction (XRD) data in Figure 7, one may observe that the synthesized materials exhibited similar diffraction peaks as those found in their commercial counterparts suggesting that both XFF and PAF materials were successfully synthesized with suitable crystallinity. The zeolitization level reached during the synthesis procedure was higher than 90 % for the two prepared materials. Nevertheless, some peaks of impurities were detected in particular the presence of quartz in the synthesized type A zeolite (PAF), which might be owed to the high silica content of the fly ash (Soe et al. 2016). The XRD of the starting materials were also obtained and indicated that both fly ashes samples contained similar mineralogical phases including quartz, mullite and hematite. However, Jorge Lacerda sample displayed more intense phase peaks, which was reflected in a higher crystalline content (~26%) against 15% from Pecém fly ash

sample (Aquino et al. 2020). The diffractograms of the fly ash samples are presented in Appendix A.

Figure 7. XRD pattern of samples: (a) Zeo13X and (b) XFF (c) Zeo4A and (d) PAF

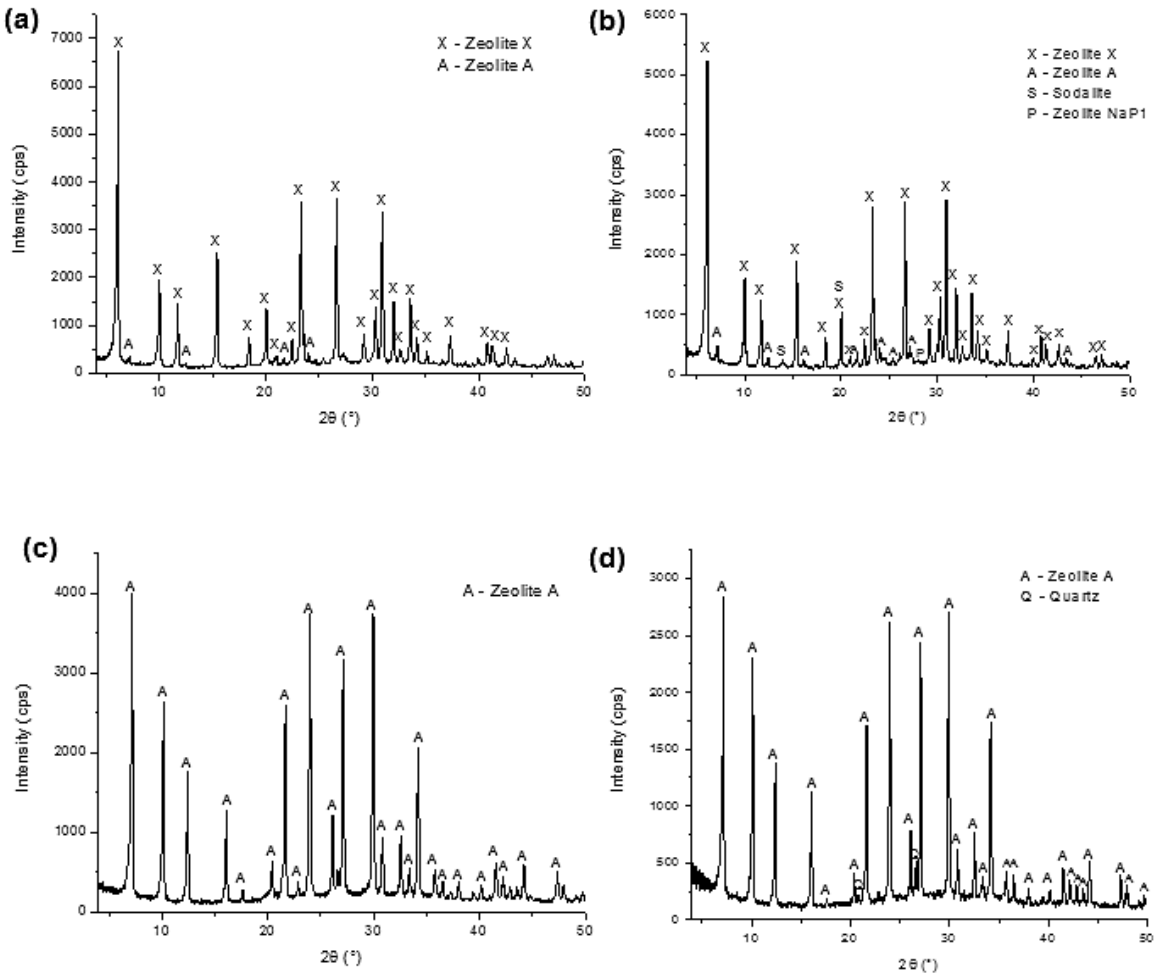

Source: Morales-Ospino et al. (2020)

The synthesized zeolites morphology was assessed via Scanning Electron Microscopy (SEM). The resulting micrographies were acquired through an EVO MA10 microscope of Zeiss. Samples were previously prepared by coating in a metallizer containing a Gold/Palladium (Au / Pd) alloy.

Figure 8. SEM images of the synthesized zeolites: (a) XFF and (b) PAF

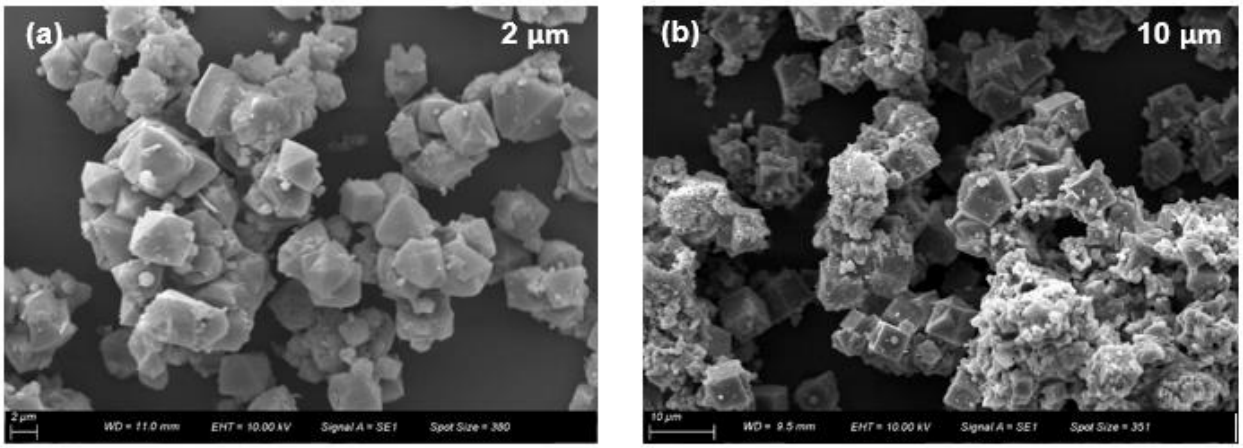

Source: Morales-Ospino et al. (2020)

Despite the apparent incrustations observed in the SEM images of the prepared samples in Figure 8, the crystals displayed characteristic shape with cubic and octahedral geometry typical of the type A and X zeolites, respectively (Soe et al. 2016). In spite of the aggregates of particulates around the crystals, no indication of defect was evidenced in the samples, which agrees with the good degree of crystallinity previously observed in XRD test.

3.2.2. Material characterization

3.2.2.1. Gas adsorption characterization analyses

The textural properties of the adsorbents were evaluated from the N_2 and CO_2 adsorption/desorption isotherms at 77 and 273 K, respectively. The specific surface area and the specific total pore volume were derived from the N_2 gas physisorption data while the specific micropore volume was obtained using both the N_2 and CO_2 isotherms. The equilibrium measurements were obtained via volumetric/manometric method by an automatic Autosorb iQ3 (Quantachrome Instruments, USA). Samples were outgassed at 300 °C and 10^{-4} mbar overnight prior to the equilibrium essays.

The specific surface area (S_{BET}) of each sample was estimated by Eq. 1 using the Brunauer–Emmett–Teller (BET) method (Brunauer et al. 1938) assuming a cross sectional area

(σ) of 1,62E-19 m^2 in the monolayer for the nitrogen molecule where the number of molecules inside that sectional area is represented by the Avogadro number (*L*). The specific monolayer capacity (n_m) was estimated following the suggestions described by Rouquerol et al. (2014). The total pore volume ($\hat{V}_P$) of the zeolites was calculated from the N_2 adsorbed amount at a relative pressure of around 0.95 (n_{sat}) i.e., right before the saturation pressure, assuming a complete pore filling by N_2 in liquid state with a density value (ρ_{N_2}) of 0.808 $g.cm^{-3}$ and a molar mass (M_{N_2}) of 28.01 $g.cm^{-3}$. The micropore volume ($\hat{V}_{mic}$) was calculated according to Eq.3 by estimating the microporosity capacity (n_{mp}) through the Dubinin-Radushkevich approach (Dubinin,Radushkevich 1947) based on the Polanyi potential theory. A density value (ρ_{CO_2}) of 1.023 $g.cm^{-3}$ (Cazorla-Amorós et al. 1998) and a molar mass (M_{CO_2}) of 44.01 $g.cm^{-3}$ were employed for the micropore volume calculation by CO_2 at 273 K.

$$S_{BET}[m^2\ g^{-1}] = n_m[mol\ g^{-1}]L\sigma \quad (1)$$

$$\hat{V}_P\ [cm^3\ g^{-1}] = n_{sat}(mol\ g^{-1})\left(\frac{M_{N2}}{\rho_{N_2}}\right) \quad (2)$$

$$\hat{V}_{mic}\ (cm^3\ g^{-1}) = n_{mp}(mol\ g^{-1})\left(\frac{M_i}{\rho_i}\right), i = N_2, CO_2 \quad (3)$$

3.2.3. Equilibrium data

The adsorption experiments were performed using two magnetic suspension balances from the same manufacturer: Rubotherm (Bochum, Germany). The first one is a two-position mode magnetic suspension balance with manual adsorbate dosing and the second one is a three-position mode magnetic suspension balance with an automatic adsorbate dosing.

The "*Zero Point Position Z* " of the balances is used to calibrate and tare the balance, the "*Measuring Point Position 1 MP1*" weighs the sample container plus the mass of adsorbent whereas the additional measuring point position of the second balance *"Measuring Point Position 2 MP2"* allows to measure the density of the surrounding gas. The pure gas CO_2, N_2 and the water vapor adsorption isotherms were performed in the

two-position microbalance while the binary CO_2/N_2 isotherms were measured using the three-position microbalance. The single component isotherms for CO_2 and N_2 were built up to 1 bar while the binary equilibrium data of CO_2/N_2 (15/85 v/v) were obtained under dynamic conditions (i.e., the gas mixture dosing is a constant continuous flow) until 7 bar.

The adsorption isotherms are generally presented in a graphical form by a plot of the excess mass versus the equilibrium relative pressure (P/P_o), or against pressure P, provided that the temperature is above the critical temperature of the adsorptive. In cases where the equilibrium measurements are carried out under conditions where the gas phase deviates considerably from ideality such as high pressure essays, it is highly recommended to plot the isotherms in terms of gas fugacity rather than pressure (Thommes et al. 2015). The characteristic equation to determine the excess mass of an adsorbate *i* ($\mathrm{m_{exc,i}}$) at a specific pressure (P) and temperature (T) is given by Eq. 4. The term (Δm) in Eq. 4 represents the mass of the gas adsorbed by the material and the second term on the right side of Eq.4 is commonly known as the buoyancy effect correction.

$$\mathrm{m_{exc,i}(P,T)} = \Delta \mathrm{m(P,T)} + (\mathrm{V_b} + \mathrm{V_s})\rho_\mathrm{g}(\mathrm{P,T}) \quad (4)$$

where V_b is the volume occupied by the components of the balance without adsorbent, V_s is the solid volume excluding internal pores and ρ_g is the surrounding gas density. On the one hand, a blank test should be performed to estimate V_b by running an experiment without adsorbent (i.e., $m_{exc}=0$ and $V_s=0$) at various values of pressure by dosing aliquots of gas. Carbon dioxide or Helium are often employed for this purpose. A plot of $(-\Delta m)$ against gas density (ρ_g) exhibits a slope equals to V_b according to Eq. 4. On the other hand, to calculate the solid specific volume (V_s), a similar experimental procedure should be performed but including the adsorbent in the sample container of the balance. Helium is a suitable adsorptive for this test since it may be considered as an inert (i.e., not adsorbed in the sample and thus, $m_{exc}=0$). A plot of $(-\Delta m)$ against vs. gas density (ρ_g) yields a slope equals to $(V_b + V_s)$ following Eq. 4, being V_b a known value. A more detailed description of the experimental device and the measurement procedure is given by Dreisbach et al. (2002).

3.2.3.1. Experimental procedure for pure gas CO_2 and N_2 isotherms

Generally, around 0.5 to 1 g of adsorbent is placed and degassed within the balance port sample overnight prior to the adsorption essay at 300 ºC during 8 h with a heating ramp of 1 ºC min^{-1}. Afterwards, the sample is cooled down to the targeted experimental adsorption temperature and later, the gas pressure is increased stepwise manually until 1 bar for the monocomponent adsorption isotherms. The mass variation is monitored and recorded uninterruptedly for each pressure level until the equilibrium condition is satisfied. The equilibrium criterion considers a mass variation of less than 10^{-4} g for at least 30 min. A correction for the buoyancy effect must be performed to allow for the determination of the excess adsorbed concentration. The temperature during the adsorption isotherms was maintained constant by means of an electrical resistance.

3.2.3.2. Experimental procedure for binary CO_2/N_2 isotherms

The experimental procedure for the binary isotherms is similar to that of the single isotherms. The main difference is that the three-position balance, with the aid of the *MessPro* software, makes the pressure increment for each point of the isotherm automatically. The number and the time of each pressure segment is user defined. A 4h time for each point of the isotherm has been found to be sufficient as equilibrium criterion for zeolites in the adsorption of CO_2/N_2 mixtures at the temperatures studied in this work.

3.2.3.3. Experimental isotherm procedure for water vapor

Since the two-position mode microbalance was not manufactured to perform water vapor adsorption measurements, the manual dosing system of the balance was altered for that purpose as seen in Figure 9.

Figure 9. Water vapor adsorption system scheme

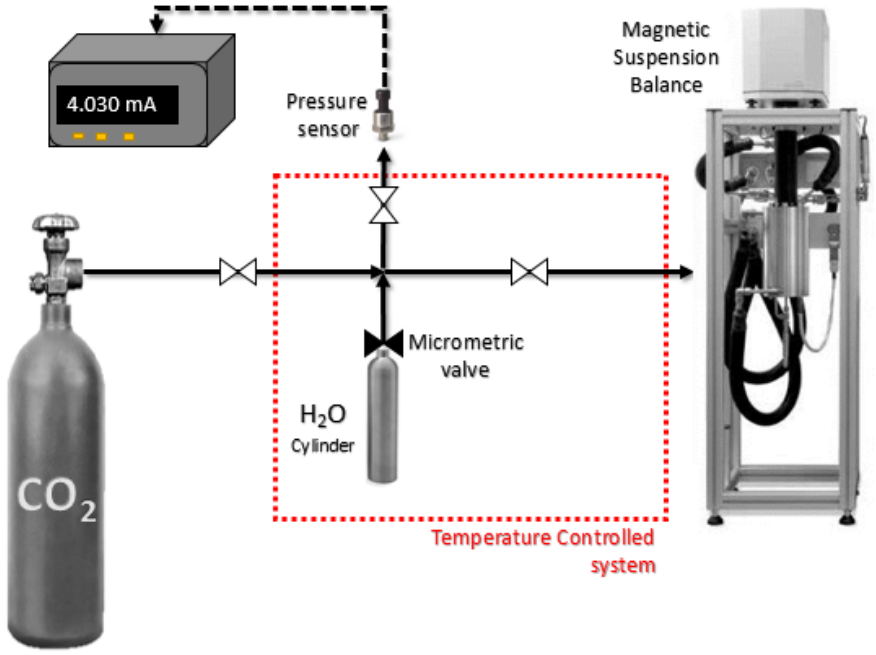

Source: own authorship

The modifications consisted of the integration of a stainless steel cylinder to store the water, a micrometric valve for water vapor dosing and a pressure transducer model P-10 (WIKA, Germany) ranging between de -1 and 2 bar gauge for a better accuracy of the pressure measurement. Additionally, a thermal tape with temperature control was used to heat the system allowing both to produce the water vapor within the cylinder at the desired experiment temperature and to prevent water condensation in the pipes and valves along the water vapor pathway towards the adsorption measurement cell.

The experimental procedure and the equilibrium condition are the same as those previously described for single component isotherms. The water vapor dosing procedure is repeated to build several experimental isotherm points until the saturation of the adsorbent. For the water/CO_2 experiments, no gaseous mixture is prepared. Instead, some water vapor amount is dosed up and once equilibrium is reached, the amount of water adsorbed is called as the “initial water loading”. Subsequently, the CO_2 isotherm is built up to 1 bar. Wang and LeVan (2010) previously demonstrated by several experiments

of water/CO_2 adsorption on zeolites that these “initial water loadings” are not affected by the coadsorption of CO_2 and can be assumed constant.

3.2.3.4. Equilibrium model

The Sips equilibrium model (Sips 1948) was used to fit pure gas isotherms. This model is a modification of the well-known Langmuir equilibrium model by the incorporation of n_i parameter that defines the heterogeneity of the adsorbent (Do,Wang 1998). Therefore, when this parameter equals the unity, the Sips equation (Eq. 5) reduces to the Langmuir equation, which is generally applied to homogeneous surfaces. Since *n* parameter is usually below the unity, the smaller its value the more heterogeneous the surface.

$$\frac{q_{e,i}}{q_{m,i}} = \frac{(b_i P)^{n_i}}{1+(b_i P)^{n_i}} \tag{5}$$

where $q_{e,i}$ is the quantity of gas adsorbed per unit mass of adsorbent at a given temperature (*T)* and pressure (*P)*, $q_{m,i}$ is the maximum adsorbed concentration per mass of adsorbent in mmol g^{-1}. Parameter b_i (bar^{-1}) is related to the affinity between adsorbate and adsorbent. Considering that the choice of the temperature-dependence form of $q_{m,i}$ can be arbitrarily chosen (Do 1998), an exponential function as shown in Eq. 6. The parameters b_i and n_i were treated as temperature dependent according to Eqs. 7 and 8, respectively.

$$q_{m,i} = q_{m0,i} \exp\left[X_i\left(1 - \frac{T}{T_0}\right)\right] \tag{6}$$

$$b_i = b_{0,i} \exp\left[\frac{Q_i}{R_g}\left(\frac{1}{T} - \frac{1}{T_0}\right)\right] \tag{7}$$

$$n_i = n_{0,i} + k_i\left(1 - \frac{T_0}{T}\right) \tag{8}$$

where $b_{0,i}$, $q_{m0,i}$ and $n_{0,i}$ are the values of b_i, $q_{m,i}$ and n_i at a reference temperature T_0. Q_i is a measure of the energy of adsorption, R_g is the ideal gas constant and both X_i and k_i are fitting parameters.

Multicomponent adsorption equilibria might regularly be predicted from pure-gas component data. The successful prediction of multicomponent adsorption equilibria strongly relies on both accurate measurements of the single component equilibrium data and adequate approach of these data with an isotherm model for mixtures. In order to predict the amount adsorbed of component *i* (*i* = CO_2, N_2) in a binary mixture, an empirical approach using the Extended Sips model for *n* number of components (*NoC*) has been applied as described in Eq. 9.

$$\frac{q_{e,i}}{q_{m,i}} = \frac{(b_i P_i)^{n_i}}{1+\sum_{j=1}^{NoC}(b_j P_j)^{n_j}} \quad , j = 1,2, \ldots, NoC. \tag{9}$$

The ideal CO_2/N_2 selectivity was estimated applying Eq. 10

$$\alpha_{CO_2/N_2} = \frac{q_{co_2}}{q_{N_2}} \frac{y_{N_2}}{y_{CO_2}} \tag{10}$$

where q_{co_2} and q_{N_2} are the CO_2 and N_2 adsorption capacities, respectively while $y_{CO_2}$and y_{N_2} are the molar fractions in the gas mixture. The values for q_{co_2} and q_{N_2} in Eq. 10 can be estimated using Eq. 9.

3.2.3.5 Isosteric heats of adsorption

The isosteric heats are the ratio of the infinitesimal change in the adsorbate enthalpy to the infinitesimal change in the amount adsorbed (Do 1998). The isosteric heats of adsorption $(-\Delta H_{ads,i})$ may or may not be a function of the adsorbate loading and can be calculated from the single gas isotherms at different temperatures for a given adsorbent sample. In a typical isotherm graph i.e., ($q_{e,i}$) vs. (*P*), the pressure values corresponding to a specific $q_{e,i}$ for each temperature are determined. Then, a graph (*ln P*) vs. (*1/T*) is plotted to display the adsorption isosteres. According to the well-known Clausius-Clapeyron equation (Eq. 11), the slope of the isosteres for a constant $q_{e,i}$ is equivalent to the value of $(-\Delta H_{ads,i})$ /R_g.

$$\frac{(-\Delta H_{ads,i})}{R_g} = \left(\frac{\partial \ln(P)}{\partial(1/T)}\right)_{q_{e,i}} \quad (11)$$

3.2.4. Moving Bed Temperature Swing Adsorption (MBTSA) simulation

The model proposed to simulate a Moving Bed Temperature Swing Adsorption (MBTSA) to capture CO_2 is explained in detail in the section 4 of this thesis.

4. MOVING BED TEMPERATURE SWING ADSORPTION (MBTSA)

4.1. MBTSA process description

The moving bed adsorption process unit for CO_2 capture considered in this study is based on the patent developed by Knaebel (2013). Figure 10 shows a schematic representation to visualize the integrated operation of each of the three sections that comprises the separation unit: adsorption, desorption and cooling section.

Figure 10. Moving bed adsorption process scheme

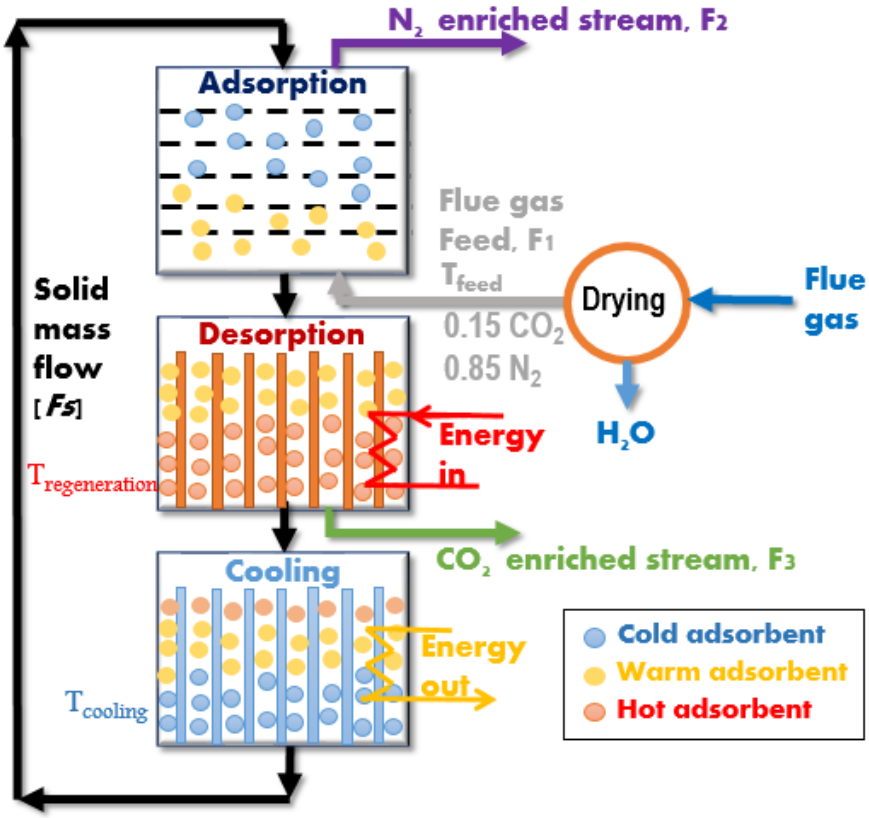

Source: (Morales-Ospino et al. 2021)

In the first place, the adsorbent falls down from the top of the adsorption section throughout a set of perforated trays that help control the time spent by the solid material inside the adsorber. This time is often known as the “residence time”. The geometrical and dimensional configuration of the trays and their holes along with the length of the adsorber and particle weight are decisive factors on the adsorbent residence time in this

section. Flue gas, previously dried in an upstream process, flows in an opposite direction to the adsorbent and is fed at the bottom of the adsorption section with the aid of a perforated distributor pipe. The CO_2 molecules are captured from the flue gas at this stage, whereas the non-adsorbed components of the gaseous mixture are collected at the adsorber upper side. The adsorbent, mostly loaded with CO_2, must be regenerated to be employed again.

The regeneration of the material occurs in the desorption section by increasing the adsorbent temperature i.e., temperature swing through indirect heating. The desorption section is essentially a parallel plate heat exchanger, which is distributed along the whole section to generate an appropriate heat exchange area between the solid material and the heat source. In contrast to the adsorption section, the adsorbent circulates co-currently with the gas stream since the CO_2 enriched stream is collected through a pipe at the end of the desorption section via vacuum. Subsequently, the outgassed adsorbent undergoes a cooling process in the last section with a similar heat exchange arrangement as in the desorption section, where the adsorbent also flows in the same direction as the gas stream. Finally, the cooled solid material is carried back to the top of the adsorption section by a bucket conveyor to begin a new adsorption cycle.

4.2. MBTSA model formulation

4.2.1. Model description

The model describing the moving bed dynamics was developed from mass, energy and momentum balances, considering the following main assumptions:

- The flow is axially dispersed for both concentration and temperature;
- There exist local thermal equilibrium between the gas and the adsorbent particles;
- The mass transfer rate of each component inside the adsorbent particle is given by a linear driving force (LDF) approximation;
- The fluid phase behaves as an ideal gas;
- Concentration, temperature and pressure gradients in directions different from the axial direction are neglected;

- The properties of the bed such as bed void fraction and packing density are considered constant and uniform for every section of the MBTSA in all the domains;
- The velocity of the particles and the molar heat capacities are constant across the whole MBTSA system.

The model formulation for the three sections of the moving bed is similar, though with minor modifications namely the boundary conditions and the heat exchange area per volume unit. The latter is much larger for the regeneration and cooling zones than that of the adsorption section. In this study, the governing equations along with their boundary and initial conditions are presented in dimensionless form. Details about the derivation of the equations and the conversion of the model equations into the dimensionless form is provided in Appendix B and C, respectively. The dimensionless variables and parameters are shown in Table 5. It is worth mentioning that although the equations describing the MBTSA model are in unsteady state, the results discussion is focused on the steady state results. Despite the usage of a set of unsteady state equations may well complex the model resolution, an unsteady state model is more likely deliver a convergent solution in steady state than a steady state model itself as indicated by Son et al. (2014).

The fluid phase mass balance for each component in the gas mixture is presented in Eq. 12. Equation 13 represents the total mass balance, which was derived by summing Eq. 12 for CO_2 and N_2.

$$\varepsilon \frac{\partial}{\partial z^*}\left(C_{g,T}{}^* \frac{\partial y_i}{\partial z^*}\right) - \alpha_1 y_{io} \frac{\partial}{\partial z^*}\left(u^* C_{g,i}{}^*\right) - \alpha_2 y_{io} \frac{\partial C_{g,i}{}^*}{\partial t^*} - (1-\varepsilon)\varepsilon_p y_{io}\left(\alpha_2 \frac{\partial C_{g,i}{}^*}{\partial t^*} + \alpha_3 \frac{\partial C_{g,i}{}^*}{\partial z^*}\right) - (1-\varepsilon)\alpha_2\alpha_4 \frac{d\bar{q}_i{}^*}{dt^*} = 0 \quad (12)$$

$$\alpha_5 \frac{\partial}{\partial z^*}\left(u^* C_{g,T}{}^*\right) + \alpha_6 \frac{\partial C_{g,T}{}^*}{\partial t^*} + (1-\varepsilon)\varepsilon_p\left(\alpha_6 \frac{\partial C_{g,T}{}^*}{\partial t^*} + \alpha_7 \frac{\partial C_{g,T}{}^*}{\partial z^*}\right) + (1-\varepsilon)\alpha_6\alpha_8 \sum_{i=1}^{NoC} \frac{d\bar{q}_i{}^*}{dt^*} = 0 \quad (13)$$

The adsorbed phase mass balance for each gas species is described by a Linear Driving Force approximation, according to Eq. 14.

$$\frac{d\bar{q}_i{}^*}{dt^*} = \frac{\partial \bar{q}_i{}^*}{\partial t^*} + \theta \frac{\partial \bar{q}_i{}^*}{\partial z^*} = \left(q_{ei}^* - \bar{q}_i{}^*\right) \quad (14)$$

Eq. 15 defines the energy balance.

$$\frac{\partial}{\partial z^*}\left(\lambda\frac{\partial T^*}{\partial z^*}\right) - \beta_1\, u^* {C_{g,T}}^* \frac{\partial T^*}{\partial z^*} + \left[\varepsilon + (1-\varepsilon)\varepsilon_p\right]\frac{(\gamma-1)}{\gamma\beta_2} T^* \frac{\partial {C_{g,T}}^*}{\partial t^*} - \beta_3 {h_w}^*(T^* - {T_w}^*) + (1-\varepsilon)\beta_4 \frac{d\bar{q}_i{}^*}{dt^*} - \frac{\varepsilon}{\gamma\beta_2}{C_{g,T}}^* \frac{\partial T^*}{\partial t^*} - (1-\varepsilon)\left[\beta_5\frac{\partial T^*}{\partial t^*} + \beta_6\frac{\partial T^*}{\partial z^*}\right] - (1-\varepsilon)\varepsilon_p {C_{g,T}}^*\left[\frac{1}{\gamma\beta_2}\frac{\partial T^*}{\partial t^*} - \beta_7\frac{\partial T^*}{\partial z^*}\right] = 0 \quad (15)$$

where γ is the ratio of the gas mixture calorific capacities at constant pressure and volume, respectively (i.e., C_{pg}/C_{vg}). The key difference between a fixed bed and a moving bed model is the accountability for the solid movement in the latter. Note that dimensionless parameters α_3, α_7, β_6, β_7 and θ are terms that include the solid velocity u_s (see Table 5) and hence describe the solid movement in the MBTSA system.

Table 5. Dimensionless variables and parameters

Independent dimensionless variables

$$z^* = \frac{z}{L}\ ;\ t^* = t\, K_{LDF,i}$$

Dependent dimensionless variables

$${C_{g,T}}^* = \frac{C_{g,T}}{C_{g,To}}\ ;\ {C_{g,i}}^* = \frac{C_{g,i}}{C_{g,io}}\ ;\ \bar{q}_i{}^* = \frac{\bar{q}_i}{q_{m0,i}}\ ;\ q^*_{e,i} = \frac{q_{e,i}}{q_{m,i}}\ ;\ u^* = \frac{u}{u_o}$$

$$T^* = \frac{T}{T_0}\ ;\ T^*_w = \frac{T_w}{T_0}\ ;\ {h_w}^* = \frac{h_w}{h_{w0}}\ ;\ \lambda^* = \frac{\lambda}{\lambda_0}\ ;\ U^*_g = \frac{U_g}{U_o}\ ;\ P^*\frac{P}{P_0}$$

Dimensionless parameters

$$\alpha_1 = \frac{u_o L}{D_{ax,i}};\ \alpha_2 = \frac{L^2 K_{LDF,i}}{D_{ax,i}}\ ;\alpha_3 = \frac{u_s L}{D_{ax,i}}\ ;\alpha_4 = \frac{\rho_p q_{m,i}}{C_{g,To}}$$

$$\alpha_5 = u_o L\ ;\ \alpha_6 = L^2 K_{LDF,i}\ ;\alpha_7 = u_s L\ ;\alpha_8 = \frac{\rho_p \sum q_{m,i}}{C_{g,To}}$$

$$\beta_1 = \frac{u_0 C_{g,T0} C_{pg}\, L}{\lambda_0}\ ;\ \beta_2 = \frac{\lambda_0}{C_{pg} C_{g,T0} L^2 K_{LDF,1}};\ \beta_3 = \frac{A_v(h_{w_0})L^2}{\lambda_0}$$

$$\beta_4 = \rho_p \sum_{i=1}^{n}(-\Delta H_{ads,i})\frac{q_{mi} L^2 K_{LDF,1}}{\lambda_0 T_0}\ ;\beta_5 = \frac{\rho_p C_{ps} L^2 K_{LDF,1}}{\lambda_0};\beta_6 = \frac{u_s \rho_p C_{ps} L}{\lambda_0};\ \beta_7 = \frac{u_s C_{g,T0} C_{pg}\, L}{\lambda_0}$$

$$\theta = \frac{u_s}{K_{LDF,i} L};\ \emptyset_1 = \frac{(1/e_w)h_w}{\rho_w C_{pw} K_{LDF,1}}\ ;\ \emptyset_2 = \frac{(1/e_w)U_o}{\rho_w C_{pw} K_{LDF,1}};\ \delta = \frac{K_D u_0 L}{P_0}$$

Source: own authorship

Note that the dimensionless parameter α_1 in Eq. 12 holds the same form as the Peclet number (*Pe*), frequently used in packed bed reactor modeling, which relates the convective flux to the dispersive. The dimensionless parameter α_3 represents an analogous significance as α_1, though related to the adsorbent since the velocity is that of the solid (u_s). Similarly, in the energy balance (Eq. 15), the dimensionless parameters β_1 and β_6 also represent a ratio between a convective and a dispersive flux, yet in terms of energy flow, where β_1 is related to the fluid and β_6 to the solid. On the other hand, the parameter Av (m^{-1}) in dimensionless parameter β_3 of the Eq. 15 refers to the ratio of heat exchange area per unit volume between each section of the moving bed and the surroundings (adsorption), the heating fluid (desorption section) or the cooling fluid (cooling section).

Eq. 16 defines the energy balance in the wall.

$$\frac{\partial \mathrm{T_w}^*}{\partial \mathrm{t}^*} = \emptyset_1(\mathrm{T}^* - \mathrm{T_w}^*) - \emptyset_2 \mathrm{U}^*(\mathrm{T_w}^* - \mathrm{T_{inf}}^*) \quad (16)$$

Due to the high void fraction in the sections of the MBTSA in comparison with fixed-bed configurations, especially in the adsorption section, the momentum balance describing the pressure drop was calculated through the Darcy equation (Eq.17).

$$-\frac{\partial P^*}{\partial z^*} = \delta u^* \quad (17)$$

4.2.2. Mass transport approach

A macropore-controlled diffusion approach was considered to calculate the mass transfer coefficients ($K_{LDF,i}$) according to Eqs. 18 and 19. This type of mass transport mechanism has been found to be suitable for CO_2/N_2 adsorption on zeolites 13X (Nikolaidis et al. (2018), Hu et al. 2013).

$$\mathrm{K_{LDF,i}} = 15\frac{\mathrm{D_{e,i}}}{\mathrm{R_p}^2} \quad (18)$$

$$\mathrm{D_{e,i}} = \frac{\varepsilon_\mathrm{p}}{\tau_\mathrm{p}}\frac{\mathrm{D_{m,i}D_{k,i}}}{\mathrm{D_{m,i}+D_{k,i}}} = \frac{\varepsilon_\mathrm{p}}{\tau_\mathrm{p}} D_{m+k} \quad (19)$$

where $D_{e,i}$ represents the effective diffusivity and R_p the particle radius. The effective diffusivity is calculated by using the Bosanquet equation which combines the contribution of both the molecular diffusivity (D_m) and the Knudsen diffusivity ($D_{k,i}$). Since both of the previously mentioned diffusivities are temperature dependent (see definitions in Table 9), thus the values of the effective diffusivity and mass transport coefficients are equally a function of the temperature. The values of D_m, $D_{k,i}$ and $D_{e,i}$ were calculated at several temperature intervals from 323 to 523 K and correlated through a linear trend line as shown in Fig 11. Parameters τ_p and ε_p in Eq. 19 represent the tortuosity factor and the particle porosity, respectively.

Figure 11. Temperature dependence plots of (a) molecular diffusivity, (b) Knudsen diffusivity and (c) effective macropore diffusivity

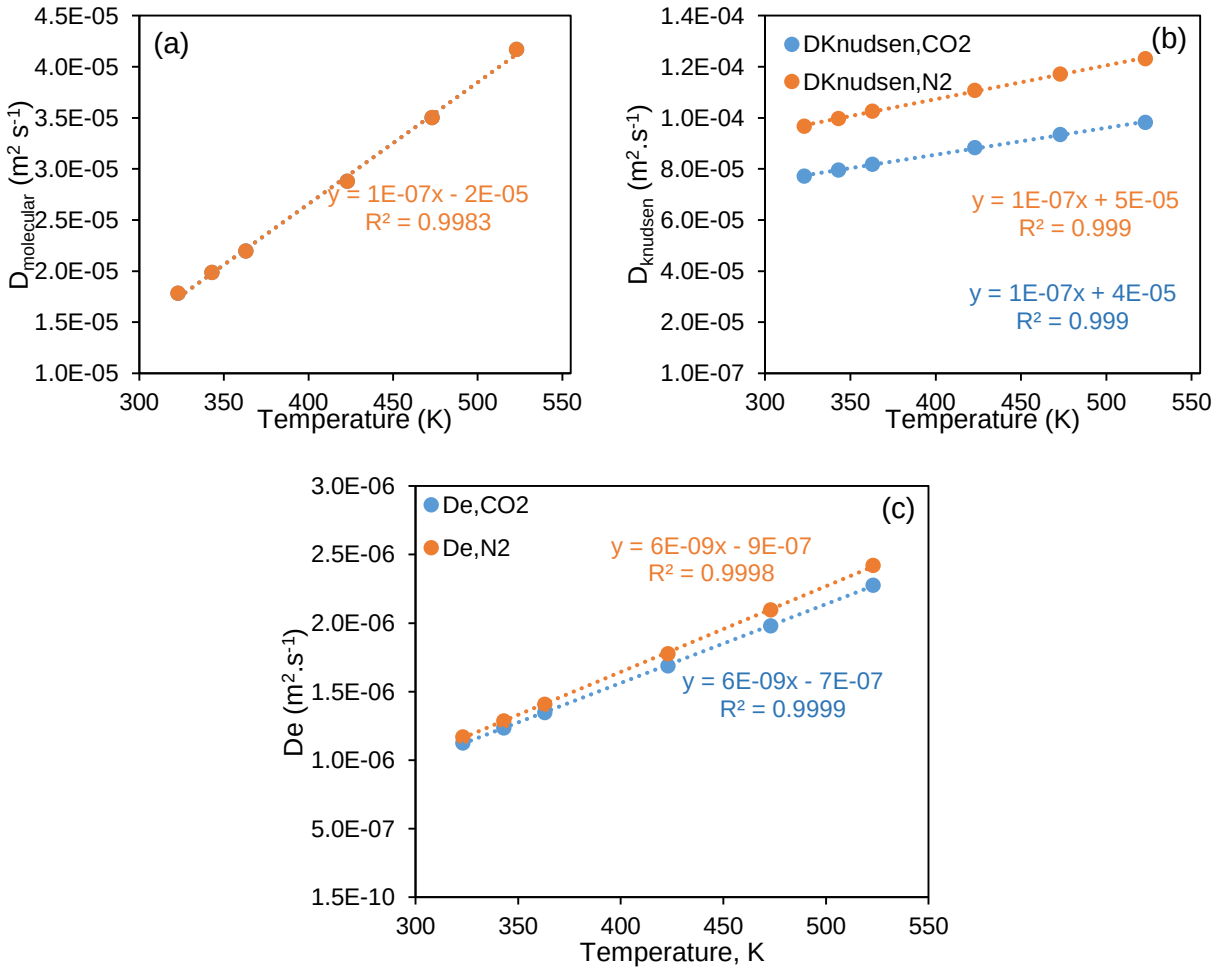

Source: own authorship

4.2.3. Boundary and initial conditions

The boundary conditions for the adsorption, desorption and cooling sections of the moving bed unit are displayed in Tables 6, 7 and 8 respectively. Particularly important to notice that some of the boundary conditions of the sections are connected to one another sequentially e.g., boundary conditions for the solid phase at the top of the adsorption section (z = 1) were assigned based on the variables calculated at the outlet of the cooling section. Similarly, the boundary conditions for the solid and fluid phases at the entrance (z = 0) of the regeneration section were given based on the variables calculated at the exit of the adsorption section (z = 0) and so on. In order to help identify from where the input variable comes from, the subscripts feed (flue gas inlet at the adsorption section), ads (adsorption section), des (desorption section) and cool (cooling section) were utilized.

Table 6. Boundary conditions for the adsorption section

Bottom of the adsorber (z = 0)	Top of the adsorber (z = 1)
$y_{io}\alpha_1 {C_{g,i}}^*\big\rfloor_{feed} = y_{io}\alpha_1 u^* {C_{g,i}}^* - \varepsilon {C_{gT}}^* \frac{\partial y_i}{\partial z^*}\Big\rfloor_{z=0}$	$\frac{\partial {C_{g,i}}^*}{\partial z^*} = 0\Big\rfloor_{z=1}$
$1\rfloor_{feed} = u^*\rfloor_{z=0}$	$\frac{\partial T^*}{\partial z^*} = 0\Big\rfloor_{z=1}$
$\beta_1\rfloor_{feed} = \beta_1 u^* {C_{g,T}}^* T^* - \lambda^* \frac{\partial T^*}{\partial z^*}\Big\rfloor_{z=0}$	$1 = P^*\rfloor_{z=1}$
	${q_{ei}}^*\rfloor_{cool} = {q_{ei}}^*\rfloor_{z=1}$

Source: own authorship

Table 7. Boundary conditions for the desorption section

Top of the regenerator (z = 0)	Bottom of the regenerator (z = 1)
$y_{io}\alpha_1 {C_{g,i}}^*\big\rfloor_{ads} = y_{io}\alpha_1 u^* {C_{g,i}}^* - \varepsilon {C_{gT}}^* \frac{\partial y_i}{\partial z^*}\Big\rfloor_{z=0}$	$\frac{\partial {C_{g,i}}^*}{\partial z^*} = 0\Big\rfloor_{z=1}$
$0\rfloor_{ads} = u^*\rfloor_{z=0}$	$\frac{\partial T^*}{\partial z^*} = 0\Big\rfloor_{z=1}$
$1\rfloor_{ads} = T^*\rfloor_{z=0}$	$1 = P^*\rfloor_{z=1}$
${q_{ei}}^*\rfloor_{ads} = {q_{ei}}^*\rfloor_{z=0}$	

Source: own authorship

Table 8. Boundary conditions for the cooling section

Top of the cooler (z = 0)	Bottom of the cooler (z = 1)
$\frac{\partial C_{g,i}{}^{*}}{\partial z^{*}} = 0\Big\rfloor_{z=0}$	$\frac{\partial C_{g,i}{}^{*}}{\partial z^{*}} = 0\Big\rfloor_{z=1}$
$0\rfloor_{des} = u^{*}\rfloor_{z=0}$	$\frac{\partial T^{*}}{\partial z^{*}} = 0\Big\rfloor_{z=1}$
$1\rfloor_{reg} = T^{*}\rfloor_{z=0}$	$1 = P^{*}\rfloor_{z=1}$
$q_{ei}{}^{*}\rfloor_{reg} = q_{ei}{}^{*}\rfloor_{z=0}$	

Source: own authorship

Equations from 20 to 24 represent the initial conditions.

$$C_{g,T}{}^{*}(z) = 1 \quad (20)$$

$$y_{CO_2}(z) = 0{,}15 \quad (21)$$

$$T^{*}(z) = 1 \quad (22)$$

$$T_w{}^{*}(z) = 1 \quad (23)$$

$$\frac{\partial \overline{q}_i{}^{*}}{\partial z^{*}}(z) = 0 \quad (24)$$

4.2.4. Model parameters

The most relevant model parameters with their support equation (when applicable) and the physical properties of the adsorbent are shown in Table 9 and 10, respectively.

Table 9. Relevant model parameters

Parameter	Symbol	Equation/Value	Auxiliary equation	Reference
Mass axial dispersion coefficient	D_{ax}	$D_{ax} = \sum_{i=1}^{NoC} y_i D_{ax,i}$	$\frac{D_{ax,i}}{D_{m,i}} = 0.7 + 0.5(Sc)(Re)$	(Ruthven 1984)
Molecular diffusivity	$D_{m,i}$	$D_{m,i} = \frac{1 - y_i}{\sum_{\substack{j=1 \\ j \neq i}}^{NoC} \frac{y_j}{D_{ij}}}$	-	(Ruthven 1984)
Binary diffusivity	D_{ij}	$D_{ij} = 0.0018583 \frac{\left[T^3\left(\frac{1}{M_i} + \frac{1}{M_j}\right)\right]^{1/2}}{P\sigma_{ij}^2 \Omega_{D,ij}}$	-	Chapman-Enskog (Bird et al. 2006)

Knudsen diffusivity	$D_{k,i}$	$D_{k,i} = 97\, r_p \sqrt{\frac{T}{M_i}}$		(Do 1998)
Heat axial dispersion coefficient	λ	$\lambda = [7 + 0.5(Pr)(Re)]k_g$	-	(Silva,Rodrigues 2001)
Gas Thermal Conductivity	k_g	$k_g = \sum_{i=1}^{NoC} \frac{y_i k_{g,i}}{\sum_{j=1}^{NoC} y_j \emptyset_{ij}}$	$k_{g,i} = \left(\hat{C}_{pg,i} + \frac{5}{4}\frac{R_g}{M_i}\right)\mu_i$	(Bird et al. 2006)
Film heat transfer coefficient	h_w	$\frac{h_w \times k_g}{d_{in}} = 12.5 + 0.048(Re)$	-	(Wakao,Funazkri 1978)
Average void fraction	ε	$\varepsilon = 1 - (\hat{V}_s + \hat{V}_p) \times \rho_b$	$\rho_b = \frac{w_{ads}(\text{in the section})}{\text{section volume}}$	-
heat exchange area per unit volume	A_v	4.60 m^{-1} (ads) 157.5 m^{-1} (des, cool)		-

Source: own authorship

Table 10. Physical properties of zeolite 13X

Property	Symbol	Value	Unit	Equation/Method/Reference
Solid specific heat	$\hat{C}_{ps}$	820	J kg^{-1} K^{-1}	-
Particle diameter (spheres)	D_p	0.0021	m	-
Tortuosity factor	τ_p	4.5	-	(Nikolaidis et al. 2018, Ko et al. 2005)
Pore radius	r_p	0.294	μm	(Hu et al. 2013)

Source: own authorship

4.2.5. Model solution

The model was solved with the aid of gPROMS Model-Builder software (Process Systems Enterprise Inc., UK). Since the set of the coupled differential equations, implemented in the gPROMS software for each of the sections of the moving bed unit, must be solved simultaneously for a continuous process simulation, the three sections were embedded and connected to each other within a composite model. Different discretization methods, degrees of order and number of intervals were tested for every section of the MBTSA to identify those providing precise and accurate results with the shortest computational time. As a result, the system was discretized according to the centered finite difference method (CFDM) of second order with 400 discretization intervals

for the adsorption section. The desorption section was solved using an orthogonal collocation on finite elements method (OCFEM) of fourth order with 25 discretization intervals and finally, the cooling section by using OCFEM of second order with 25 discretization intervals for the section.

4.2.6. Performance parameters of the MBTSA

The performance of an adsorption process for CO_2 capture from flue gas may be assessed by using the following four key parameters: CO_2 recovery, CO_2 purity, energy consumed per mass of CO_2 recovered and productivity. Purity and recovery are directly related to the efficiency of the separation process and can be often considered as process specifications. Once these requirements are met, the process is then assessed in terms of productivity and energy demand for its commercial viability.

The CO_2 recovery or capture rate is defined as the fraction of CO_2 in the product stream from the amount of CO_2 in the feed stream as shown in Eq. 25. The purity, which is directly related to the selectivity of the adsorbent, is calculated in this study on a molar basis (see Eq. 26). Productivity is defined as the molar rate of CO_2 recovered per mass of adsorbent in the MBTSA system by Eq. 26.

$$\mathrm{CO_2\ recovery} = \frac{\text{mols of } CO_2 \text{ in the Product}}{\text{mols of } CO_2 \text{ in the Feed}} \left[\frac{\text{mol } CO_2}{\text{mol } CO_2}\right] \tag{25}$$

$$CO_2 \text{ purity} = \frac{\text{mols of } CO_2 \text{ in the Product}}{\text{mols of all species in the Product}} \left[\frac{\text{mol } CO_2}{\text{mol all species}}\right] \tag{26}$$

$$\text{Productivity} = \frac{\text{moles per unit time of } CO_2 \text{ in the Product}}{\text{Mass of adsorbent}} \left[\frac{\text{mol } CO_2}{\text{h kg adsorbent}}\right] \tag{27}$$

The energy consumption ($E_{consumption}$), in Eq. 32, contemplates as main energy inputs: the energy required for the adsorbent regeneration $E_{desorption}$ (Eq.28) and the energy required for the water removal from the flue gas E_{drying} (Eq. 29). The upstream drying process was assumed to be performed by a silica guard bed with a required thermal energy (e_{H_2O}) of 8 MJ kg^{-1} H_2O as suggested by Joss et al. (2017). Since the flue gas is

usually saturated with moisture, the volumetric fraction of water in the untreated flue gas relies on the gas stream temperature. The potential energy change to transport the solid (E_{solid}) by the bucket conveyor assuming 50 % of efficiency was estimated according to Eq. 30. Finally, the energy recovered from the hot adsorbent in the cooling section ($E_{recovery}$), assuming a 50% of energy recovery efficiency, was calculated with Eq. 31. Both $E_{desorption}$ and $E_{recovery}$ are calculated by the integration of the overall heat transport coefficient $U_g(z)$ multiplied by the temperature difference across the section, where the term T_{inf} in Eqs. 27 and 30 indicates the regeneration temperature and the cooling temperature, respectively. While for $E_{desorption}$ the energy transfer comes from a heat source at T_{inf} equals to the regeneration temperature, for $E_{recovery}$ the energy is transferred from the solid to a cooling fluid at a assumed T_{inf} of 70 °C.

$$\mathrm{E_{desorption}} = \frac{\int_{z=0}^{z=L} \mathrm{U_g(z)} * \left(\mathrm{T_{inf}} - \mathrm{T_g(z)}\right) * \mathrm{dA(z)}}{\text{mass per unit time of } \mathrm{CO_2} \text{ in the Product}} \left[\frac{\mathrm{MJ}}{\mathrm{kg\ CO_2\ recovered}}\right] \quad (28)$$

$$\mathrm{E_{drying}} = \frac{\mathrm{e_{H_2O}\ u_o y_{H_2O} \rho_{H_2O}}}{\text{mass per unit time of } \mathrm{CO_2} \text{ in the Product}} \left[\frac{\mathrm{MJ}}{\mathrm{kg\ CO_2\ recovered}}\right] \quad (29)$$

$$\mathrm{E_{solid}} = \frac{\mathrm{F_s\ g\ \Delta L}}{\text{mass per unit time of } \mathrm{CO_2} \text{ in the Product}_3} * \frac{1}{50\%} \left[\frac{\mathrm{MJ}}{\mathrm{kg\ CO_2\ recovered}}\right] \quad (30)$$

$$\mathrm{E_{recovery}} = \frac{\int_{z=0}^{z=L} \mathrm{U_g(z)} * \left(\mathrm{T_g(z)} - \mathrm{T_{inf}}\right) * \mathrm{dA(z)}}{\text{mass per unit time of } \mathrm{CO_2} \text{ in the Product}} \left[\frac{\mathrm{MJ}}{\mathrm{kg\ CO_2\ recovered}}\right] \quad (31)$$

$$\mathrm{E_{consumption}} = \mathrm{E_{desorption}} + \mathrm{E_{drying}} + \mathrm{E_{solid}} - 50\% * \mathrm{E_{recovery}} \left[\frac{\mathrm{MJ}}{\mathrm{kg\ CO_2\ recovered}}\right] \quad (32)$$

5. RESULTS

5.1. Gas characterization of the zeolite samples

The N_2 adsorption/desorption isotherms at 77 K for all the samples are shown in Figure 12 (a).

Figure 12. Adsorption-desorption isotherm of: (a) N_2 at 77 K, (b) CO_2 at 273 K on different zeolites (empty symbols for desorption data), (c) and (d) are the same graphs in semi-logarithmic axis.

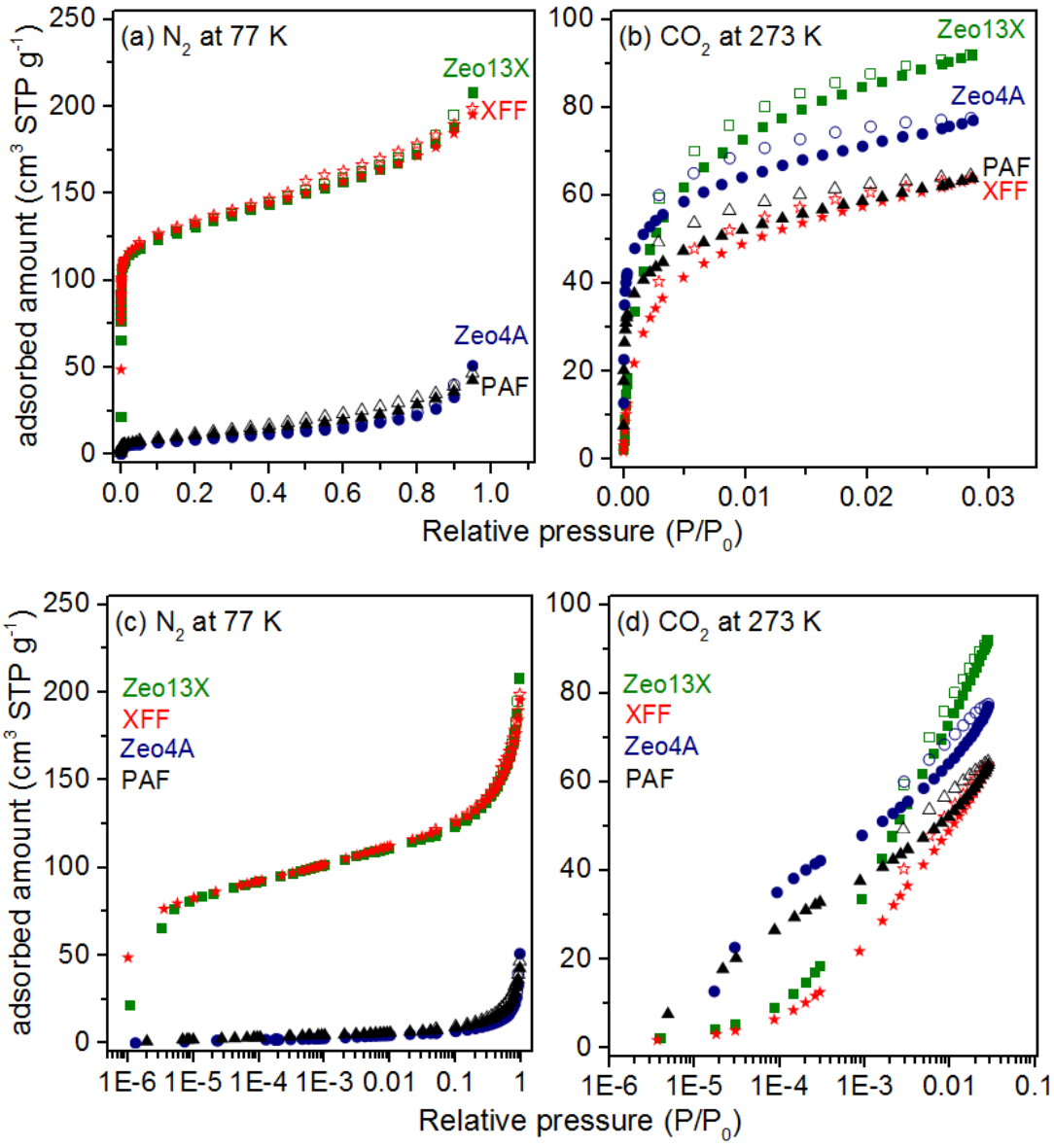

Source: modified from Morales-Ospino et al. (2020)

The synthesized zeolites exhibited almost identical isotherms as the commercial materials. However, Type A zeolites uptake of N_2 at 77 K was significantly lower in comparison with that of type X zeolites. A monitoring of the N_2 adsorption experiment at 77 K indicated that the diffusion of the N_2 molecule into the small pores of the type A zeolites under such conditions seemed to be very slow, turning the equilibration time of these samples particularly high. A potential reason for that phenomenon to occur, might be related to the eventual blocking of the adsorbent pores by the cations of the zeolites so that to the probing N_2 molecules were unable to reach the access point, resulting in little measurable BET surface area (< 30 $m^2.g^{-1}$) (Feng et al. 2018, Liu et al. 2011). Another explanation is that the pore blocking may also be the result of preadsorbed N_2 molecules that can inhibit further adsorption in the region of the ultramicropores (pore widths < 7Å) since a pore width of 7Å corresponds to the bilayer thickness of the N_2 molecule (Lowell et al. 2006). Such experimental limitation makes unviable to estimate the total pore volume and the micropore volume of type A zeolites by N_2 adsorption at 77 K.

In contrast, CO_2 adsorption-desorption isotherms at 273 K were satisfactorily obtained for all the four samples as regarded in Figure 12(b). The N_2 and CO_2 isotherms in Figure 12 can be classified as reversible type I (a) according to IUPAC classification, where no prominent hysteresis loop is perceived as expected in predominantly microporous materials and the micropore filling is observed specially at low coverage (Thommes et al. 2015).

The textural properties for all the adsorbents are summarized in Table 11. The BET surface area was estimated using the Brunauer- Emmett -Teller (BET) equation in a relative pressure interval between 10^{-6} and 10^{-2} with a linearity coefficient R^2=0.999 for both samples 13X and XFF. Although the above pressure range is clearly below the typical pressure range of linearity ($0.05<P/P_o<0.3$) suggested by Brunauer, materials containing micropores have already been reported to show good linearity on the BET plot at relative pressure values smaller than the recommended range, which is more suitable for adsorbents exhibiting type II or IV adsorption isotherms (Rouquerol et al. 2006). The total pore volume was estimated at a relative pressure (P/P_0) of 0.95 and the micropore volume by applying the Dubinin-Radushkevich (DR) equation to both the N_2 and CO_2 isotherm

data. The DR equation was attempted to be applied in a relative pressure range between 10^{-5} and 10^{-1} since linear plots in a variety of microporous materials have been found within this interval of relative pressure (Lowell et al. 2006). For type X zeolites, an interval of relative pressures from 10^{-5} to 10^{-2} worked well for both adsorbates (N_2 and CO_2), whereas for type A zeolites the linearity range was limited to a narrow range of relative pressures as seen in Table 11.

Table 11. Textural characteristics obtained by adsorption-desorption isotherms of N_2 at 77 K and CO_2 at 273 K.

Sample	N_2				CO_2	
	BET surface area ($m^2\,g^{-1}$)	Total pore volume, $\hat{V}_p$ ($cm^3\,g^{-1}$)	Micropore volume, $\hat{V}_{mic}$ ($cm^3\,g^{-1}$)	Range of applicability of DR equation (P/P_o)	Micropore volume, $\hat{V}_{mic}$ ($cm^3\,g^{-1}$)	Range of applicability of DR equation (P/P_o)
Zeo13X	501	0.32	0.18	1.10^{-5}-1.10^{-3}	0.27	2.10^{-5}-3.10^{-3}
XFF	509	0.30	0.18	1.10^{-5}-1.10^{-3}	0.20	2.10^{-5}-3.10^{-3}
Zeo4A	23	-	-		0.22	2.10^{-2}-3.10^{-2}
PAF	28	-	-		0.19	2.10^{-2}-3.10^{-2}

Source: Modified from Morales-Ospino et al. (2020)

According to results shown in Table 11, one can notice that Zeo13X and XFF samples displayed, by N_2 adsorption, similar characteristics. However, CO_2 adsorption characterization at 273 K reveals that Zeo13X sample exhibits a larger volume of micropores than that indicated by N_2 adsorption. Since the saturation pressure of CO_2 at 273 K is relatively high (~35 bar) in comparison with the pressure range at which the CO_2 adsorption isotherm test is performed, diffusion problems often encountered with N_2 adsorption at cryogenic temperatures may be overcome with the CO_2 adsorption essay. As a result, the micropore analysis can be extended to pores of smaller sizes that are reachable to CO_2 molecules, but not to nitrogen. Nevertheless, since the relative pressure is considerably low (P/P_0 = 0.03) at the experiment conditions (isotherm up to 1 bar), the measurable pore size range is limited to pore sizes up to 15 Å (Lowell et al. 2006). This result implies that the micropore volume for the Zeo13X sample was underestimated by N_2 adsorption characterization, and therefore, this additional pore volume should

contribute to a better performance of the material on the adsorption of CO_2 at higher temperatures.

On the other hand, CO_2 adsorption characterization confirms the micropore volume found with N_2 adsorption at 77 K for XFF sample and that the micropore volume of the PAF and Zeo4A samples are comparable. Total pore volume could not be calculated from CO_2 isotherms since the evaluated pressure range is very distant from the saturation pressure of CO_2 at 273 K (P/P_0 up to 0.03) as seen in Figure 12(b), inhibiting the usage of the liquid-state assumption, which is mandatory for the total pore volume estimation.

Gas adsorption characterization was also useful to derive some intrinsic parameters of the adsorbents that are helpful for simulation purposes. The list of the estimated parameters are presented in Table 12.

Table 12. Intrinsic parameters of the adsorbents derived from gas characterization

Parameter	Equation	Zeo13X	XFF	Zeo4A	PAF
Solid volume, V_s ($cm^3\,g^{-1}$)	-	0.48	0.38	0.41	0.45
Solid density, ρ_s ($Kg\,m^{-3}$)	$\rho_s = \frac{1}{\hat{V}_s}$	2096	2632	2442	2235
Particle density, ρ_p ($Kg\,m^{-3}$)	$\rho_p = \frac{1}{\hat{V}_s + \hat{V}_p}$	1252	1467	-	-
Particle porosity, ε_p	$\varepsilon_p = \left(\frac{\hat{V}_p}{\hat{V}_s + \hat{V}_p}\right)$	0.44	0.43	-	-

Source: Own authorship

The blank test with Helium in the magnetic suspension balance allowed to estimate the volume occupied by the components of the balance without adsorbent (V_b= *1.2098 cm³*). The specific solid volume $\hat{V}_s$ was determined according to the Helium essay prior to the adsorption isotherm experiments as described in section 3.2.3. The plots of *(–Δm)* vs. ρ_{He} can be observed in Figure 13. The value of V_s (cm^3) obtained from the subtraction of V_b from the slope of the straight line should be divided by the sample mass employed in the essay to obtain the corresponding specific solid volume $\hat{V}_s$ ($cm^3\,g^{-1}$).

Figure 13. Helium test to estimate the volume of the solid of the four zeolite samples

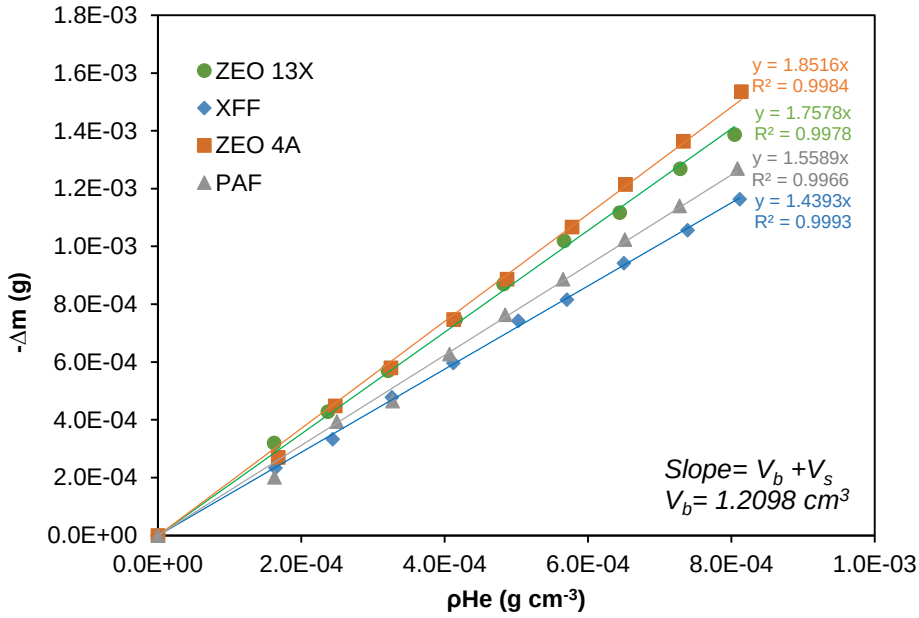

Source: own authorship

The particle density calculation requires the values of both the specific solid volume ($\hat{V}_s$) and the specific total pore volume ($\hat{V}_p$) from N_2 characterization at 77 K. Particle density and solid density are often used interchangeably in the literature, which can be somewhat confusing. For the sake of clarity, in this work, we have defined the particle density (ρ_p) as the mass per volume unit whose volume includes internal pore volume of the particle while the solid density (ρ_s) considers merely the solid skeletal volume discounting the internal pore volume. Consequently, the particle porosity (ε_p) may be defined by the ratio between the total specific pore volume ($\hat{V}_p$) and the total specific particle volume ($\hat{V}_s + \hat{V}_p$) as seen in Table 12.

5.2. Equilibrium data results

5.2.1. CO_2 and N_2 adsorption

Figure 14 and 15 show the CO_2 and N_2 adsorption isotherms of the four samples at the three studied temperatures (50, 70 and 90 °C).

Figure 14. CO2 adsorption isotherms at 50, 70 and 90 °C for (a) Type X zeolites: Zeo13X and XFF and (b) Type A zeolites: Zeo4A and PAF (symbols are experimental points and lines simulated data)

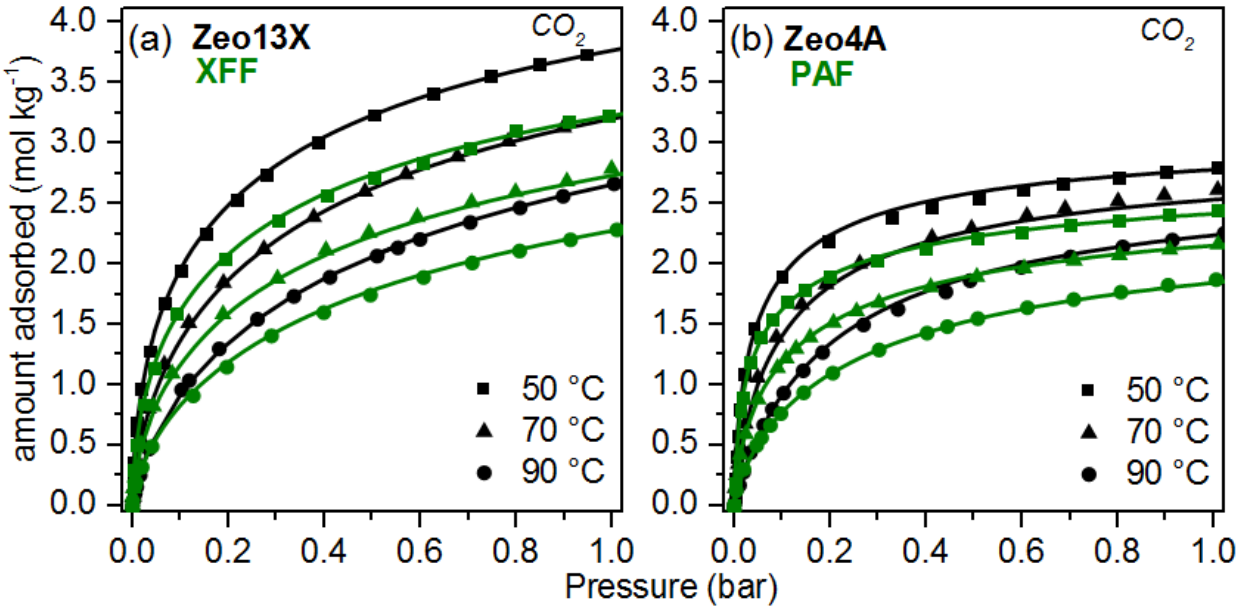

Source: modified from Morales-Ospino et al. (2020)

Figure 15. N_2 adsorption isotherms at 50, 70 and 90 °C for (a) Type X zeolites: Zeo13X and XFF and (b) Type A zeolites: Zeo4A and PAF (symbols are experimental points and lines simulated data)

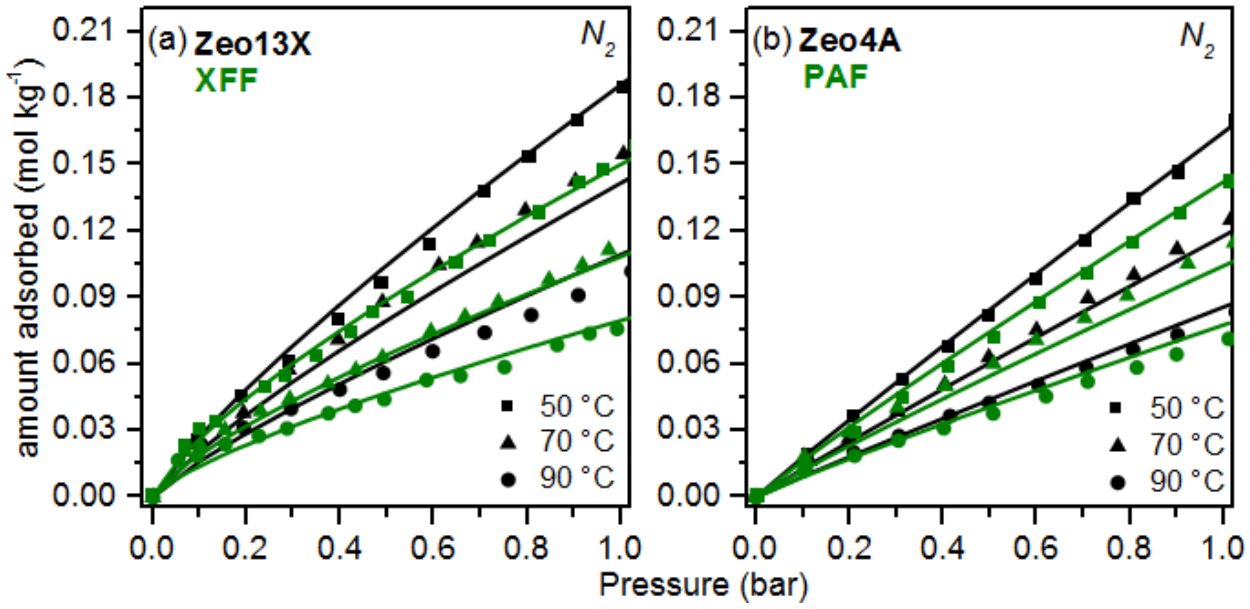

Source: modified from Morales-Ospino et al. (2020)

CO_2 adsorption on zeolites has been widely covered in the literature, showing consensus on the implication of both physisorption and chemisorption as adsorption mechanisms (Bertsch,Habgood 1963, Montanari,Busca 2008). However, the CO_2 experimental isotherm data suggests that physical adsorption might be the predominant adsorption mechanism since an increase in the temperature isotherm results in an adsorption capacity reduction and vice versa. Even if commercial zeolites performed slightly better on both the CO_2 and the N_2 adsorption in the pressure range between 0 and 1 bar as observed in Figure 14 and 15, one may say that the synthesized samples represent a fair match of the commercial materials ratifying the potential of fly ash as starting material for the synthesis of zeolites. Nonetheless, it is worth to highlight that the synthesized samples are in powder form without any binder. In pelletized or bead-shaped zeolite particles, the binder represents at least 20% of the mass percent of the zeolite particle to reach the desired mechanical strength (Bingre et al. 2018). If the synthesized materials were tested in compact form and the binder is assumed to be a non-adsorbent material, the adsorption capacity of the prepared samples per adsorbent mass would likely decrease in a similar proportion as the binder weight percentage in the sample.

The superior CO_2 adsorption uptake of Zeo13X over XFF may also be explained by the larger micropore volume of the commercial zeolite as predicted by the CO_2 characterization at 273 K. A closer look at the equilibrium data also reveals that Type X zeolites showed higher CO_2 adsorption capacity than the type A especially at pressure values closer to 1 bar. Nevertheless, type X zeolites appeared to be more affected by the reduction of isotherm temperature type A zeolites.

Sips model was used to fit the experimental isotherm data due to its accuracy and feasibility to be extended in multicomponent mixtures. The Sips model fittings, also shown in Figure 14 and 15 for the three selected temperatures, showed good agreement with the experimental data for the two adsorbates. The fitting parameters of the Sips model for single adsorption isotherms of CO_2 and N_2 for all the samples are shown in Table 13. The direct multicomponent extension of the Sips model was used to predict the binary adsorption of a gas mixture containing 0.15 CO_2/ 0.85 N_2 by using the single component fitting parameters of the Sips isotherm model as observed in Figure 16.

Table 13. Sips model parameters for CO_2 and N_2 adsorption on commercial and synthesized zeolites.

Adsorbate	Parameters	Zeo13X	XFF	Zeo4A	PAF
CO_2	b_0 (bar^{-1})	3.08	2.56	18.14	14.92
	q_{m0} (mol kg^{-1})	5.75	5.12	3.16	2.90
	n_0	0.57	0.57	0.69	0.59
	Q_i (J mol^{-1})	19204	17618	33640	36397
	k	1.43	1.00	2.09	1.67
	X	1.58	1.54	1.00	1.00
N_2	b_0 (bar^{-1})	1.37E-03	8.15E-04	3.22E-03	2.55E-03
	q_{m0} (mol kg^{-1})	45.18	33.39	41.50	37.75
	n_0	0.83	0.76	0.96	0.93
	Q_i (J mol^{-1})	7000	9000	7000	7000
	k	0	0	0	0
	X	2.36	2.87	3.04	2.72

Source: own authorship

Figure 16. CO_2/N_2 binary isotherm (0.15 CO_2 and 0.85 N_2 v/v) at 50, 70 and 90 °C for (a) Type X zeolites: Zeo13X and XFF and (b) Type A zeolites: Zeo4A and PAF.

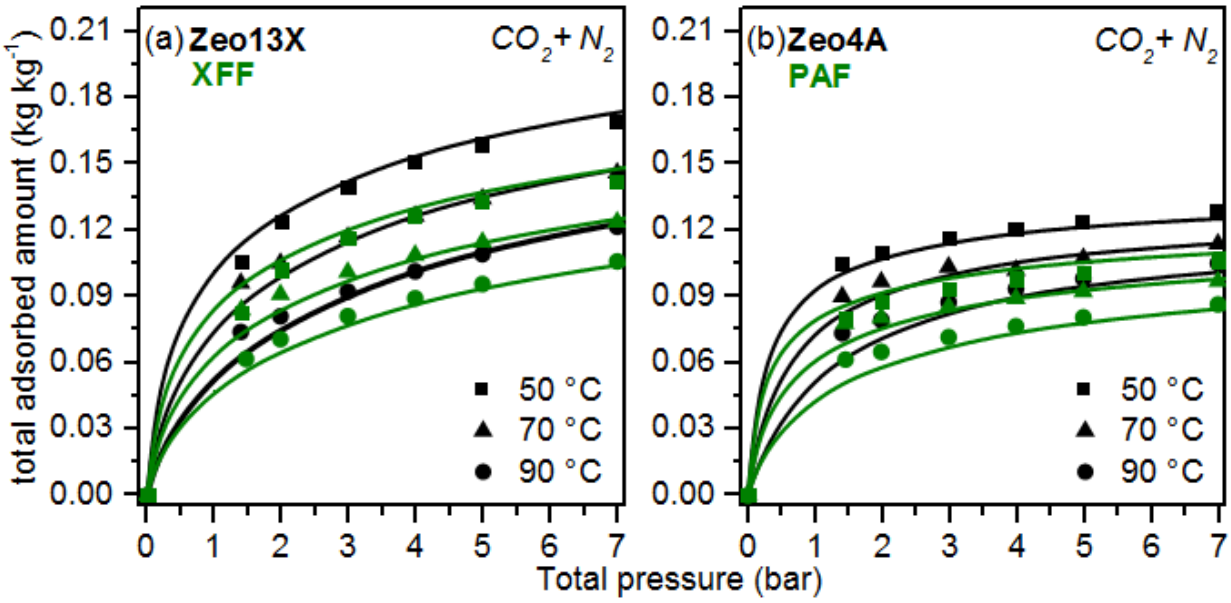

Source: Modified from Morales-Ospino et al. (2020)

According to the Sips model fitting, the CO_2 adsorption capacity at dry post-combustion conditions (i.e., 1 bar of total pressure 0.15 CO_2/ 0.85 N_2 and 50°C) follow the sequence: Zeo13X (0.099 g g^{-1}) > Zeo4A (0.093 g g^{-1}) > XFF (0.083 g g^{-1}) > PAF (0.079 g g^{-1}). For N_2 adsorption, the uptake in decreasing order is Zeo13X (2.8 mg g^{-1}) > XFF (2.4 mg g^{-1}) > PAF (1.3 mg g^{-1}) = Zeo4A (1.3 mg g^{-1}). The graphical results showing the

predicted amount adsorbed of each component in the gas mixture by the Extended Sips model are presented in Appendix D.

The fair agreement between the experimental and the simulated data, for the four adsorbents in Figure 16, enable to apply the Extended Sips model to make an estimation of the ideal CO_2/N_2 selectivity of all the samples at different pressure levels of the gaseous mixture. As shown in Figure 17, type A zeolites displayed by and large greater values of CO_2/N_2 selectivity, nevertheless, this difference is reduced as the temperature increases. Considering again the case of dry post-combustion scenario (50 °C and 1 bar), the performance of the adsorbents, according to their selectivity, follows the sequence: Zeo4A (253) > PAF (216) > Zeo13X (130) > XFF (127) as shown in Figure 17(a). Although Zeo13X was the sample with the highest adsorption uptake under the studied conditions, its equally high N_2 adsorption uptake impaired its selectivity performance. Conversely, sample Zeo4A, also with a similar CO_2 adsorption capacity as Zeo13X, exhibited the highest selectivity to capture CO_2 over N_2 given its poor N_2 adsorption performance in comparison with the other samples, which suggests that its performance in a carbon capture process could potentially lead to a higher purity of the CO_2 enriched stream.

Figure 17. Ideal selectivity for CO_2/N_2 binary setup (0.15/0.85) vs. Total pressure (bar) at (a) 50, (b) 70 and (c) 90 °C.

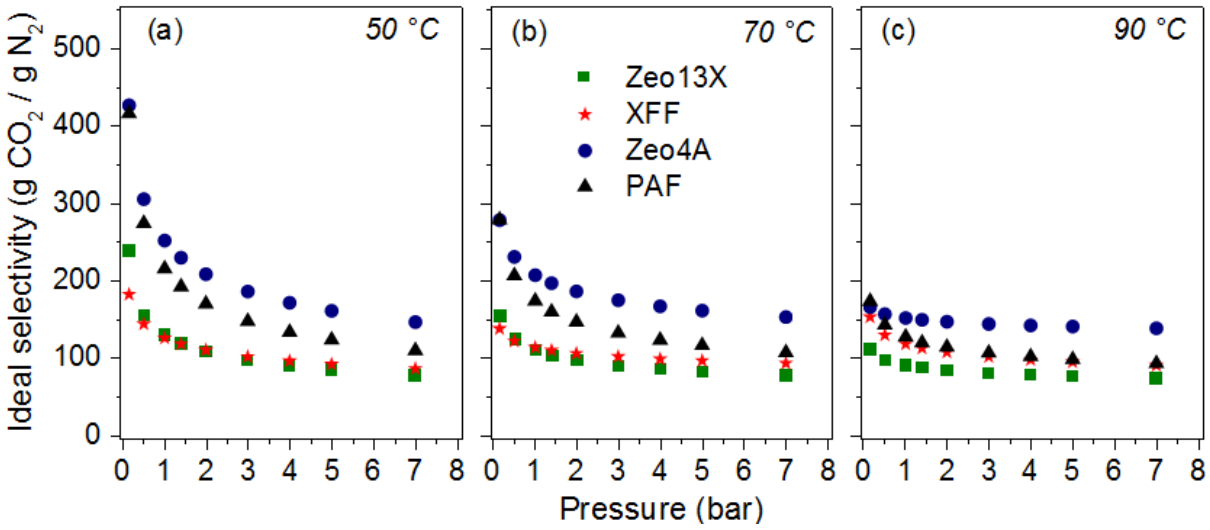

Source: modified from Morales-Ospino et al. (2020)

The isosteric heats of adsorption of CO_2 and N_2, shown in Figure 18 for all the materials, were estimated from the adsorption isotherms at different temperatures (50 to 90 °C) using the Clausius-Clapeyron equation. The isosteres were obtained for different values of the equilibrium absorbed amount ($q_{e,i}$) for the two adsorbates. An example of the isosteres plot is shown in Figure 19 and 20 for selected equilibrium concentrations of CO_2 and N_2 respectively, where the slope of the straight line represents $-\Delta H_{ads,i}/R_g$. The higher the slope of the curve, the higher the isosteric value at a given component loading.

Figure 18. Isosteric heat of adsorption of (a) CO_2 and (b) N_2 vs. adsorbed amount for commercial and synthesized zeolites.

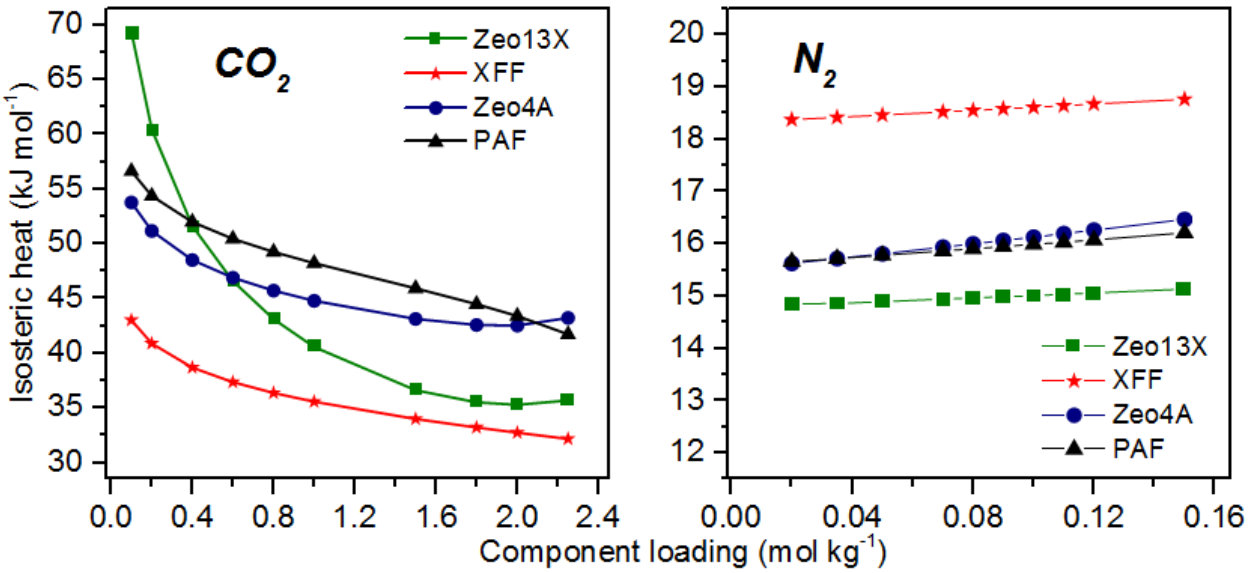

Source: Modified from Morales-Ospino et al. (2020)

The decreasing profile of isosteric heats against the CO_2 uptake indicates strong energetic interaction between the adsorbate and the adsorbent surface especially at low coverage. Meanwhile, the nearly constant N_2 isosteric profile suggests a homogeneous energetic interaction between the adsorbate and the different zeolite samples since the isosteric heat appeared to be independent of the N_2 loading over the studied range. The isosteric heats values of CO_2 and N_2 obtained for the type A and type X zeolites are in accordance with previously reported values in the literature (Li et al. 2009a). Commercial sample Zeo13X happened to be the most energetically heterogeneous sample for CO_2 adsorption once its isosteric heat might reach values up

to 70 kJ mol^{-1} at very low coverage and go down to ca. 35 kJ mol^{-1} at higher adsorbed amounts. Additionally, one can also notice in Figure 18 that CO_2 isosteric heats for type A zeolites are similar in contrast to Type X zeolites. The discrete isosteric heat data may be useful to estimate mean values for this parameter as listed in Table 14.

Figure 19. Adsorption isosteres of CO_2 on different zeolite samples. Points were calculated by numerical interpolation of fitted adsorption isotherms at a $q_{e,CO_2} = 1.5\ mol\ kg^{-1}$. Lines represent linear fit.

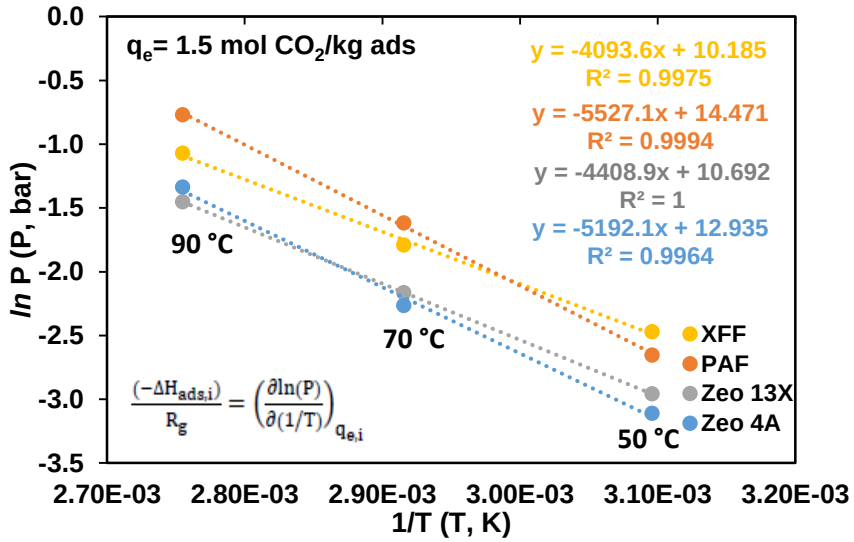

Source: own authorship

Figure 20. Adsorption isosteres of N_2 on different zeolite samples. Points were calculated by numerical interpolation of fitted adsorption isotherms at a $q_{e,N_2} = 0.09\ mol\ kg^{-1}$. Lines represent linear fit.

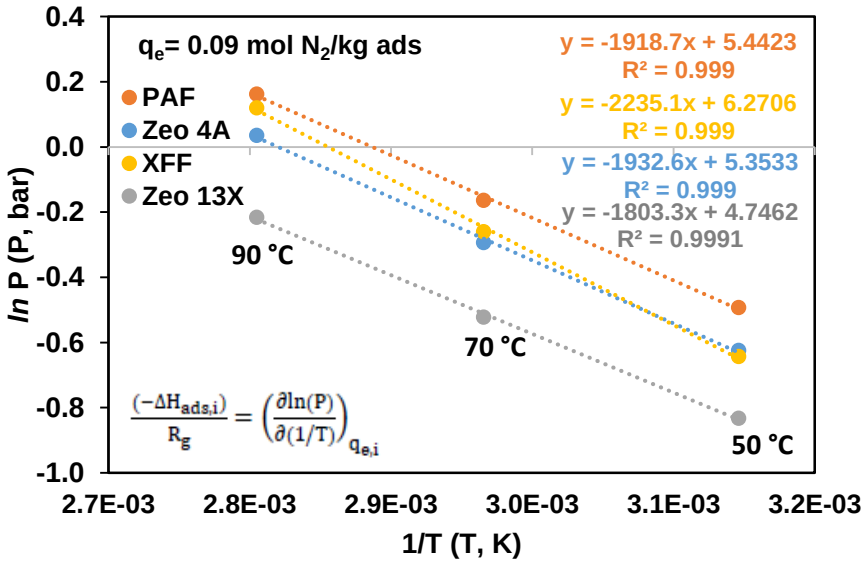

Source: own authorship

Table 14. Average isosteric heats of adsorption of CO_2 and N_2 for commercial and synthesized zeolites.

CO_2	Zeo13X	XFF	Zeo4A	PAF
Average heat of adsorption (kJ mol^{-1})	45.51	36.43	46.26	48.67
N_2	Zeo13X	XFF	Zeo4A	PAF
Average heat of adsorption (kJ mol^{-1})	14.98	18.56	16.02	15.92

Source: Modified from Morales-Ospino et al. (2020)

Nonetheless, due to the typically strong dependence of the isosteric heat on the adsorbate loading, it is highly recommended to employ an empirical equation relating these two variables for process simulation purposes to prevent the under or overestimation of the heats of adsorption unless the isosteric heat remains constant over the whole coverage range.

5.2.2. Water vapor adsorption

The pure water vapor adsorption isotherms for the four studied materials are plotted in Figure 21. The shape of the isotherms may be considered as Type I.

Figure 21. Water vapor adsorption isotherms at 50, 70 and 90 °C for (a) Zeo13X and (b) XFF (c) Zeo4A and (d) PAF.

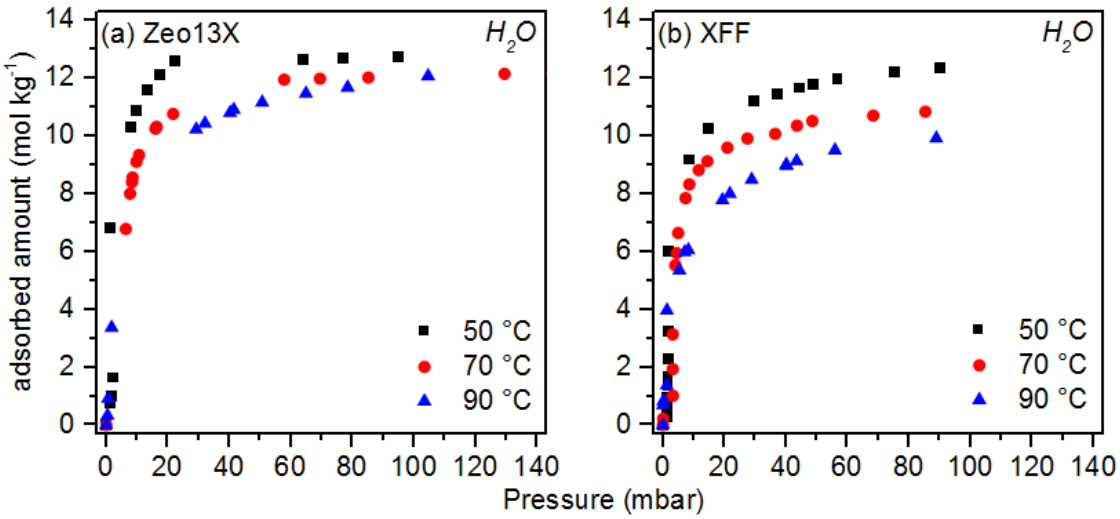

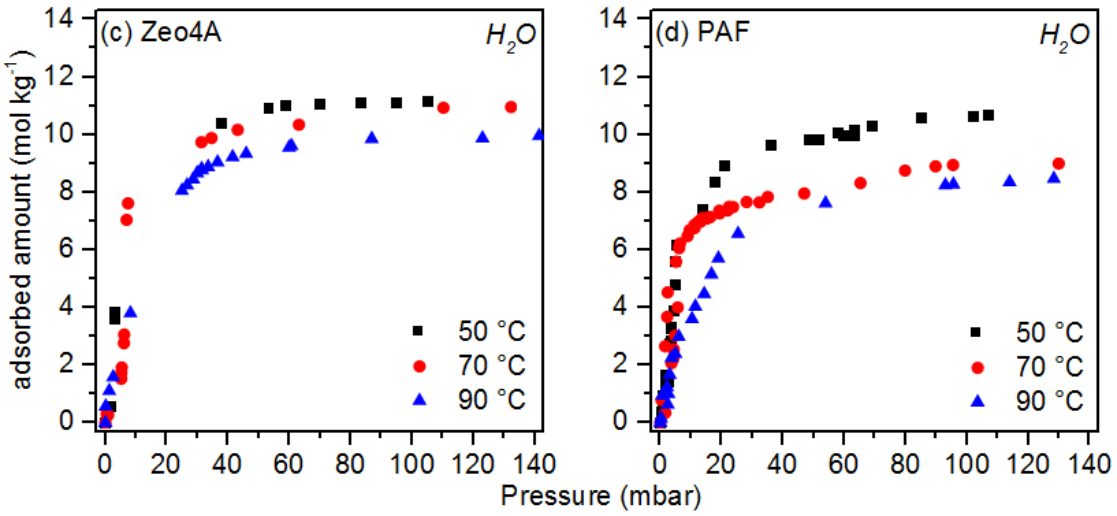

Source: own authorship

At first glance, it is very notorious the particularly steep increase in the initial water adsorption on the zeolite samples at pressures below 40 mbar attaining maximum concentrations of adsorbed water between 8 mol kg $^{-1}$ (for PAF sample) and 13 mol kg^{-1} (for Zeo13X sample). The high affinity of zeolites to capture water at such low pressures is likely to be given by the sharp interplay between the zeolite cations and the polar water molecules (Li et al. 2009b). More precisely, the permanent dipole of the water molecule causes strong interactions with the charges of the adsorbents whose selectivity for CO_2 is the consequence of its quadrupole moment (Joos et al. 2013), which is then reflected in large heats of adsorption as formerly reported by Rege et al. (2001).

Figure 22. Water vapor adsorption isotherms (P/Psat vs. water loading) at 50, 70 and 90 °C for (a) Zeo13X and (b) XFF (c) Zeo4A and (d) PAF.

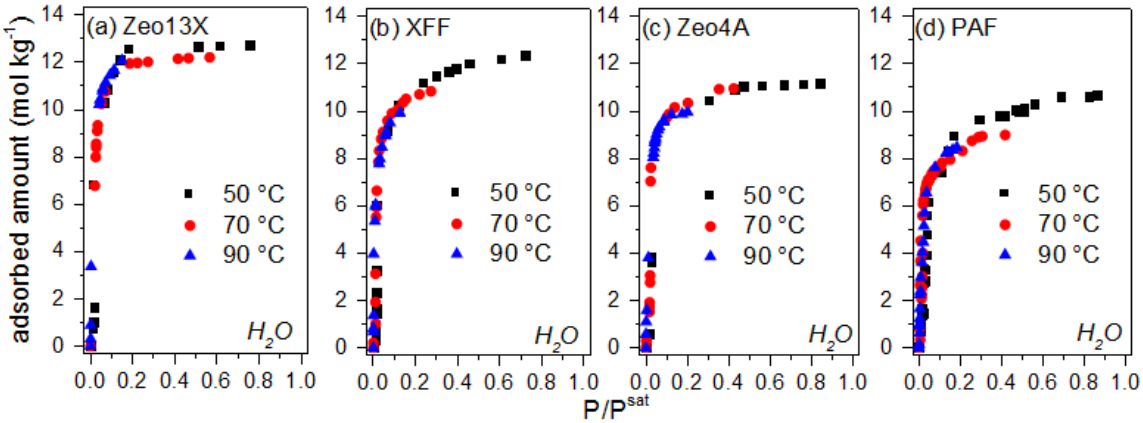

Source: own authorship

The same water isotherms, when plotted against P/P^{sat} instead of P, align perfectly as can be regarded in Figure 22. This isotherm overlapping regardless the temperature of the experiment was also observed by Leppäjärvi et al. (2012)

To assess the influence of the water presence on the CO_2 adsorption capacity of the zeolites, the materials were initially loaded with a water concentration lower than that of the saturation of the material so that it was possible for the adsorbent to adsorb CO_2 afterwards. Once the sample equilibrated with the initial water loading, the CO_2 adsorption isotherm was built and compared against the pure CO_2 isotherm. The concentration at which any of the samples is considered saturated is the water uptake at the plateau of the isotherms presented in Figure 21 while Equation 33 outlines how the initial water loadings are calculated. Let us take into consideration the example of 8 % as initial water loading for commercial zeolite 13X in Figure 21 (a). The maximum water concentration at 50 °C for sample Zeo13X according to Figure 21 (a) is around 13 mol kg^{-1}. Therefore, the initial water loading equivalent to 8 % is around 1 mol H_20 kg^{-1} ads.

$$initial\ water\ loading\ (\%) = \frac{initial\ adsorbed\ amount\ of\ H_2O\ \ [mol\ kg^{-1}]}{maximum\ H_2O\ \ concentration\ [mol\ kg^{-1}]} \times 100 \tag{33}$$

The initial water loadings may differ from sample to sample as shown in Figure 23.

Figure 23.CO_2 adsorption isotherms at 50ºC for: a) Zeo13X and (b) XFF (c) Zeo4A and (d) PAF samples with different “initial water loadings”. The percentages represent the fraction of H_2O from its saturation concentration.

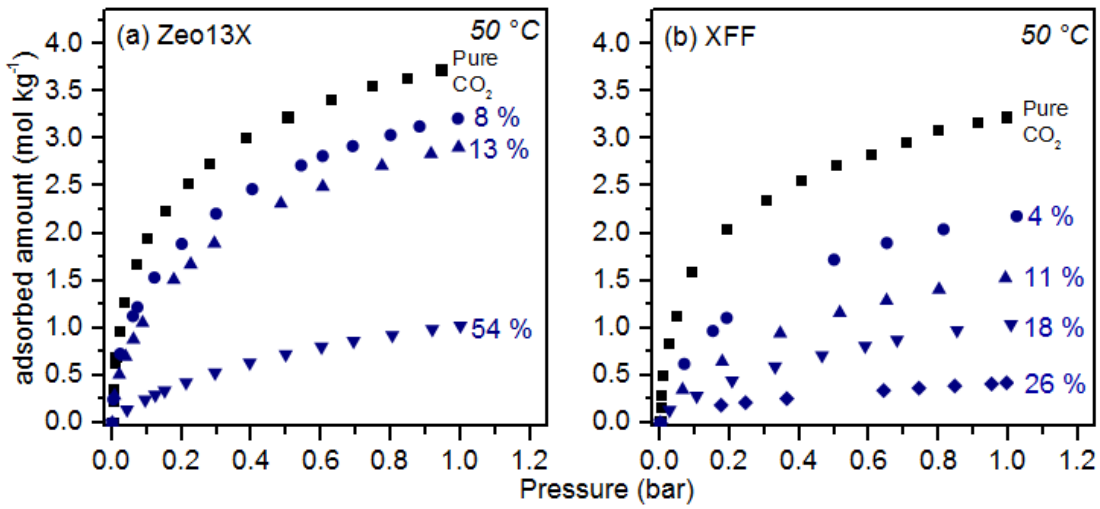

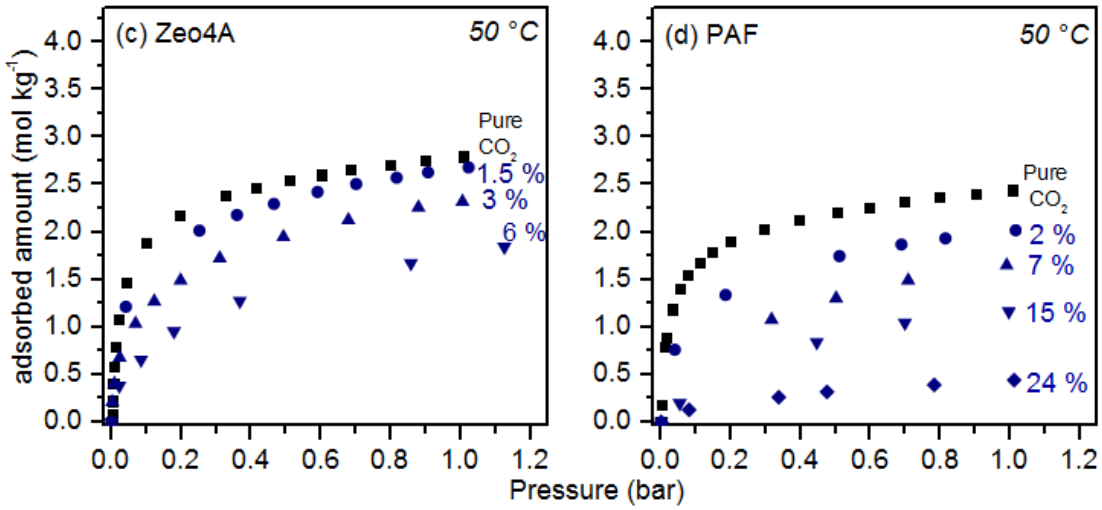

Source: own authorship

Dosing the same amount of water to obtain a specific water loading on each zeolite sample was not a straightforward procedure given the principle of our experimental rig. Since the water dosing was manually made by opening the micrometric valve as previously shown in Figure 9, the level of valve opening and the dosing time affected the amount of water vapor supplied to the balance. In other words, it is not possible to know *a priori* how much water should be dosed to obtain a specific adsorbed amount at equilibrium. Thus, attempting to obtain the same initial water loading for all the samples was hard to achieve. Consequently, some amount of water vapor was simply injected, equilibrated and recorded. Subsequently a series of CO_2 injections were made towards the balance to construct the correspondent CO_2 isotherm.

The decrease of CO_2 adsorption capacity observed in all the samples after some water loading implies that H_2O preferentially takes over the adsorption sites so that the availability of those sites for the CO_2 adsorption is gradually reduced with increasing water loadings. This observation was also described by Joos et al. (2013), whose molecular simulation work estimated that at flue gas conditions (i.e., CO_2 and H_2O partial pressures of around 0.15 and 0.12 bar, respectively) water would probably be adsorbed close to its saturation concentration, while the CO_2 uptake would be reduced by an order of magnitude. In the same way, the expected reduction in the equilibrium capacity for CO_2, by the presence of water, has also been experimentally observed in the works of Brandani and Ruthven (2004) using the zero length column (ZLC) technique.

Despite the notorious deterioration on the CO_2 adsorption performance in all the samples with the presence of moisture, it is worth highlighting that commercial zeolite 13X appeared to display a greater tolerance to cope with water. Meanwhile, type A zeolites and synthesized type X (XFF) were severely affected by the water presence even at low water loadings as observed in Figures 23 (b), (c) and (d). Given the above discussion, the capture of CO_2 on a wet flue gas stream with zeolites, even for zeolite 13X, is greatly discouraged owed to the prominent loss of CO_2 adsorption capacity. In fact, flue gas is generally saturated with moisture at post-combustion conditions and mostly water would be adsorbed on the adsorbent. To illustrate the previous statement, let us consider the CO_2 isotherm of the most "water proof" of the our studied materials (i.e., commercial zeolite 13X) at 54% of the water saturation concentration preloaded at 50 °C as shown in Figure 21 (a). Even at nearly the half of the maximum water concentration for sample Zeo13X, the CO_2 uptake already diminished abruptly. In real conditions, the scenario might be even more concerning once a 12 v/v of water concentration (partial pressure of 0.12 bar) is enough to saturate the adsorbent as can be seen in Figure 21 (a). In other words, dealing with wet CO_2+N_2 gas mixture would affect not only the CO_2 capture rate, but also the other key performance parameters of any CO_2 capture process unit that uses zeolites as adsorbent. The CO_2 recovery decline would force the use of more solids to compensate the poor CO_2 capture performance, hence impairing the productivity. Likewise, the purity percentage of the product stream would drop given the sharp selectivity of zeolites to adsorb water and finally, more energy would probably be required to desorb the wet adsorbent because of the large heat of adsorption of H_2O.

All things considered, in this work, it is suggested the flue gas stream undergo a drying process prior to its injection to the capture system provided that zeolites are used as solid materials. Moreover, as previously described in section 4.2.6., this upstream moisture removal should be taken into account as part of the energy consumption item to understand the extent of the energy penalty imposed by the drying operation.

5.3. Moving Bed Temperature Swing Adsorption (MBTSA) unit simulation

This section is concerned with the issue of the performance of a Moving Bed Temperature Adsorption (MBTSA) system, as the one described in section 4.1, to capture CO_2. The system will be assessed in terms of several key performance indicators through the variation of some process variables and other parameters. In the preceding discussion, four adsorbents were evaluated in terms of characterization and equilibrium data in an attempt to shed light on their eventual performance within a process separation unit. Even if the commercial adsorbents may have displayed an enhanced performance based on the adsorption metrics, the synthesized samples from coal fly ash also showed a promising potential as CO_2 capture adsorbents at dried conditions. However, the prepared samples were tested in powder form and yet need to be tested in bead form (or pellets) as the commercial samples. Adsorbents in powder are not advised for MBTSA units because of the potential loss of mass that can occur.

Based on the adsorption metrics, it seems fair to suggest that, under dry post-combustion scenario, both commercial Zeolite 13X and 4A are promising candidates to capture CO_2 on a MBTSA unit. On the one hand, 13X exhibited a higher CO_2 capacity but 4A happened to be more selective. The selection between these two adsorbents might not be a straightforward task. Nevertheless, in this work, kinetic data were not obtained experimentally and given the availability of reliable diffusion mechanism understanding on zeolites 13X in the literature, as a first attempt the simulations of the MBTSA unit will be run with commercial sample Zeo13X.

5.3.1. Commercial zeolite 13X adsorption isotherms

Since the commercial zeolite 13X was chosen to run the pilot plant tests, another batch of the zeolite 13X from the same manufacturer was purchased. On top of this, we consider fair to undergo this second batch of the adsorbent the same equilibrium experiments once they are key input data for the MBTSA system simulation. The main results are briefly discussed in this section.

The experimental and fitted adsorption isotherms for pure CO_2 and N_2 on zeolite 13X are shown in Figure 24. Sips model parameters, listed in Table 15, were again suitable to fit the experimental data.

Figure 24. Pure CO_2 (a) and N_2 (b) adsorption isotherms on zeolite 13X at different temperatures (between 50 and 250 °C) up to 1 bar. Symbols are experimental data and lines represent the Sips model fittings.

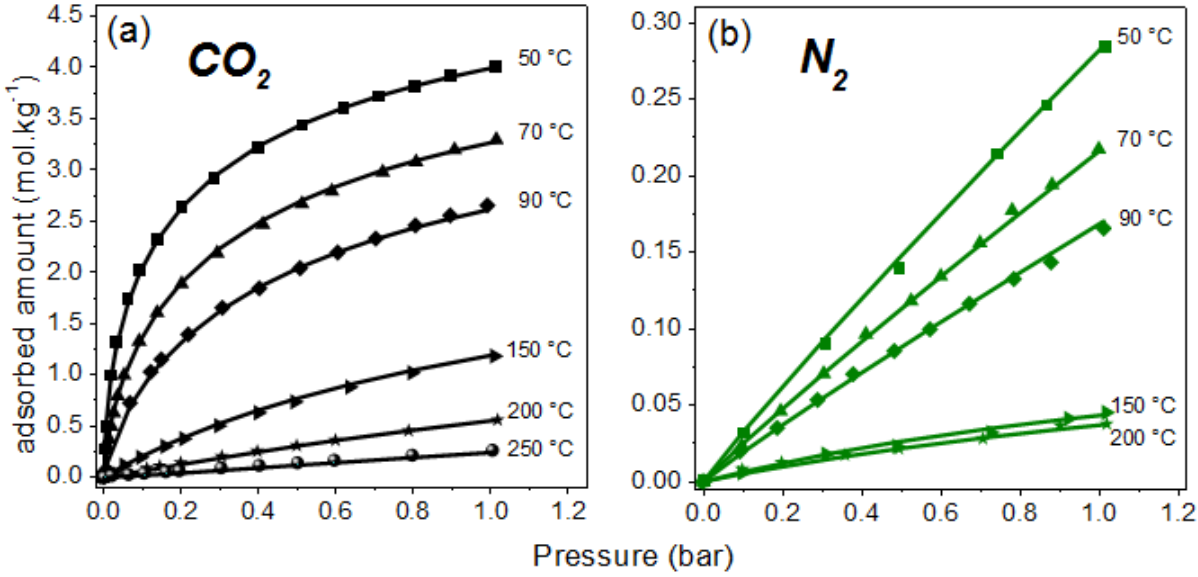

Source:(Morales-Ospino et al. 2021)

Table 15. Sips model parameters for CO_2 and N_2 adsorption on commercial zeolite 13X

Adsorbate	b_o (bar^{-1})	Q_i ($J\ mol^{-1}$)	q_{mo} ($mol\ kg^{-1}$)	X_i	n_o	k
CO_2	3.26	17000	5.99	2.47	0.58	1.62
N_2 (Low T)	0.014	8000	16.51	1.69	0.95	0
N_2 (High T)	1.13	8000	0.121	0	1	0

Source: (Morales-Ospino et al. 2021)

Particularly noteworthy that the temperature range of the adsorption isotherms was spanned on purpose up to 250 °C for CO_2 and to 200 °C for N_2, aiming to cover the whole range of temperature that the MBTSA unit might go through such as the high temperatures in the desorption section. N_2 isotherms were unable to be experimentally obtained over 200 °C because the adsorbed amount of N_2 at such elevated temperatures

was close the limit of detection of the gravimetric equipment, so that N_2 adsorption was practically undetectable under such high-temperature conditions.

Note that in Table 15, the Sips model parameters for N_2 were divided into two regions with different isotherm fittings in order to enhance the accuracy of the fit. As a result, The N_2 isotherm parameters for the lower temperatures (50, 70 and 90 °C) were used for the adsorption and cooling sections of the MBTSA and the higher temperature fitting (150 and 200 °C) was employed in the regeneration section. On the contrary, CO_2 adsorption was represented by a single isotherm fitting over the whole set of temperatures. The isosteric heats of adsorption for each adsorbate ($-\Delta H_{ads,i}$) as function of loading are shown in Figure 25.

Figure 25. Isosteric heats of adsorption for CO_2 and N_2 against each component loading. The points represent the Clapeyron estimated values of isosteric heats and the lines are empirically fitted isosteric heats.

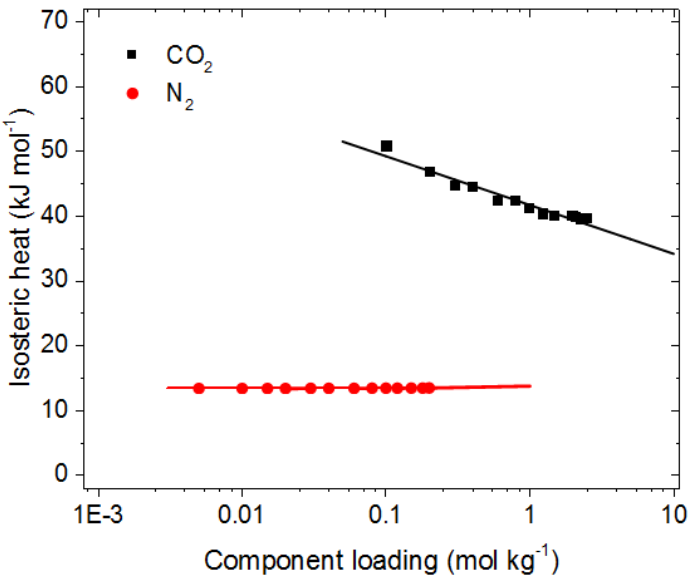

Source: (Morales-Ospino et al. 2021)

The values of the isosteric heats were estimated with the aid of the Clausius-Clapeyron equation from 50 to 250 °C for CO_2 and from 50 to 200 °C for N_2. Note that for N_2, the isosteric heats values remain nearly invariable over the loading range implying a homogeneous energetic interaction between the adsorbate and the adsorbent. For that reason, the N_2 isosteric heat (~ 13.5 kJ mol^{-1}) was held as a constant value independent of the uptake. Conversely, CO_2 isosteric heat showed a significant dependence on the

adsorbate loading. At low coverage, larger isosteric heats of adsorption can be observed suggesting that energetically stronger interactions might take place at the beginning of the adsorption process; however, those interactions become weaker as the CO_2 loading advances. Therefore, the CO_2 isosteric heat dependence (J mol^{-1}) on the CO_2 uptake q_{CO2} (mol kg^{-1}) was mathematically described by an empirical equation (Eq. 34) for simulation purposes.

$$(-\Delta H_{ads,CO_2}) = 3272\ln(q_{CO_2}) + 41724 \quad (34)$$

5.3.2. Flue gas pre-drying

As discussed in section 5.2.2., flue gas should be dried when zeolites are employed as adsorbents to capture CO_2 at post-combustion conditions. Therefore, in this simulation study, flue gas is subjected to an upstream drying operation with a guard bed as the one described in section 4.2.6. The extra energy to dehydrate the flue gas is calculated according to Eq.29. Finally, a complete water removal was equally assumed so that composition of the feed flue gas consists merely of CO_2 and N_2. The results of the water vapor and binary water vapor/CO_2 adsorption isotherms at 50°C for the second batch of the commercial zeolite 13X were very similar to those observed in the first 13X sample. The experimental water isotherms of the second 13X are shown in Appendix E.

5.3.3. MBTSA simulation routine

This section is devoted to describe the simulation procedure to evaluate the effect of some operational and design parameters on the performance of the studied MBTSA process unit. A fundamental assumption in the course of the simulation routine was that the solid mass flowrate (F_s) was held constant for the three sections of the MBTSA. The main input data to run the simulations are listed in Table 16.

Table 16. Simulation main input data

Feed
Flue gas composition: 0.15 CO_2/ 0.85 N_2 (%vol.)
Inlet Temperature: 50 °C
Pressure: 1 atm
Flue gas flowrate ($Nm^3\ h^{-1}m^{-2}$): 100/120/145
Adsorption section
Residence time (s): 25/50/100/200/400
Desorption section
Average void fraction: 0.59
Regeneration temperature (°C): 200/220/240
Cooling section
Average void fraction: 0.59
Cooling temperature: 70 °C

Source: (Morales-Ospino et al. 2021)

As can be noted in Table 16, some input information are fixed values (e.g., flue gas composition or the void fraction in both the desorption and the cooling section) and others are considered variables (e.g., flue gas flowrate or the regeneration temperature). Given these points, the simulation procedure consisted of the sequence described in Figure 26. The solid flowrate was varied gradually and increasingly aiming at identifying the F_s range that would provide the highest CO_2 recovery rates.

Figure 26. MBTSA simulation sequence

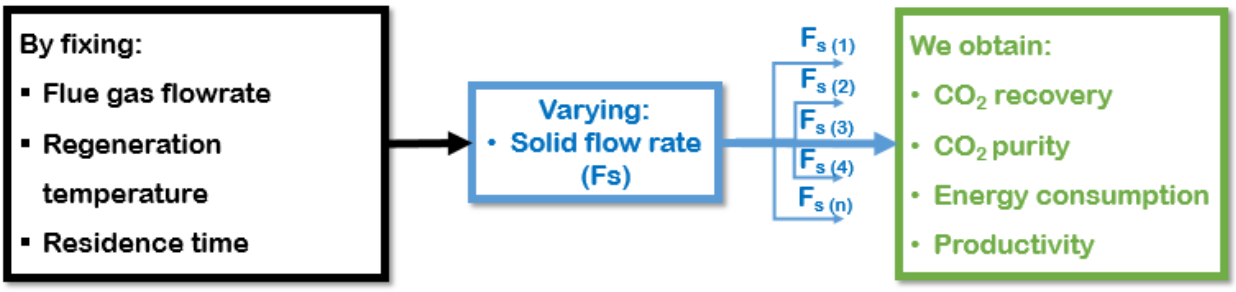

Source:(Morales-Ospino et al. 2021)

Accordingly, if F_s varies and the residence time (t_R) is fixed, the mass of solids (w_{ads}) at an instant in the adsorption section must also change to preserve the same t_R as described in equations 35 and 36.

$$F_s = \frac{u_s \times w_{ads}}{L} \quad (35)$$

$$t_R = \frac{w_{ads}}{F_s} \quad (36)$$

The solid velocity for each section is defined by equation 37.

$$u_s = \frac{L}{t_R} \quad (37)$$

The foregoing procedure was repeated by assigning other values (as in Table 14) for the variables in the left-hand box of Figure 26 (flue gas flowrate, regeneration temperature and residence time). Consequently, a large output dataset was obtained, which can be summarized in terms of process specification (plot of Purity vs. Recovery) and process performance (plot of Energy demand vs. Productivity) as shown in Figure 27.

5.3.4. MBTSA simulation results

5.3.4.1. Effect of feed gas volumetric flowrate

Three volumetric values of feed flue gas have been employed to understand its effect on the performance parameters as can be seen in Figure 27. In the first place, lower volumetric flowrates may lead to both higher purity and recovery values according to Figure 27. CO_2 recovery over 90% can be achieved for the different feed gas flowrates evaluated. However, The CO_2 purity results suggest that there might exist a limiting value (not higher than 92% mol) and it declines as the feed gas flow rate is increased. For instance, at 100 $Nm^3\ h^{-1}m^{-2}$, the lowest feed gas flowrate studied, it is feasible to obtain purity values of around 91%mol with CO_2 recoveries up to 98%. In contrast, at 145 Nm^3

$h^{-1}m^{-2}$, the highest feed gas flowrate studied, 91%mol purity could reduce CO_2 recovery to as low as 50%.

Figure 27. (a) CO_2 purity vs. CO_2 recovery and (b) Productivity vs. Energy consumption at different gas flowrates (100, 120 and 145 $Nm^3\ h^{-1}m^{-2}$)

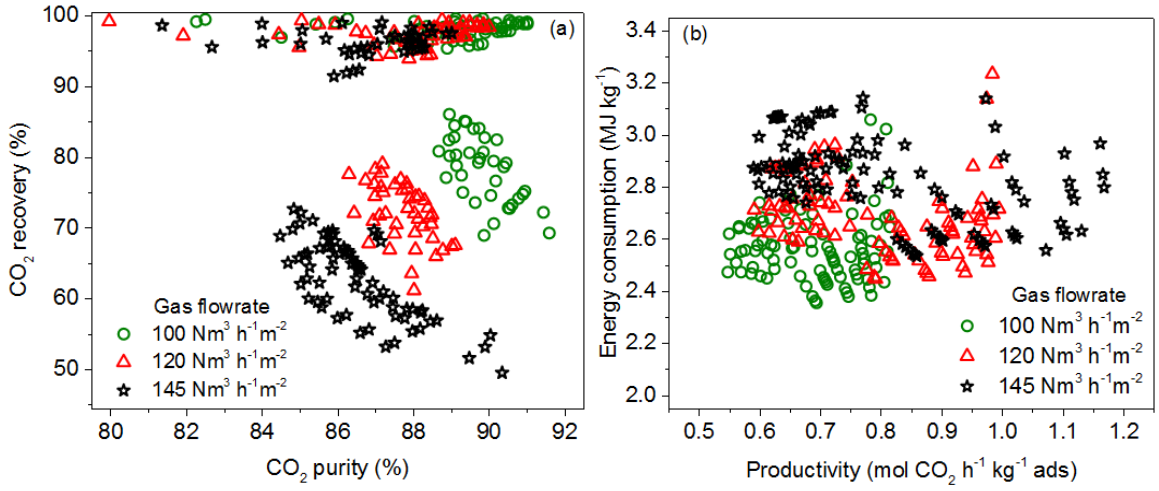

Source:(Morales-Ospino et al. 2021)

Moreover, it has been reported by the US Department of Energy (DOE) that values of CO_2 purity and recovery of at least 95% and 90%, respectively, are recommended as target separation specifications for CCS processes (Nelson et al. 2017).Under the conditions studied in this work, the CO_2 purity in the product stream does not reach the target 95% value. Nevertheless, following the trend of Figure 27(a), it is likely that, by further decreasing the feed gas flowrate, we might reach the purity specification at the expense of a lower throughput of the process unit.

On the other hand, Figure 27 (b) demonstrates that higher productivities can be achieved even when the flue gas flow rate is raised. The former observation suggests that the additional amount of solids required to deal with a larger flue gas flow rate does not increase in the same proportion as the flue gas flow rate. The energy consumption output, assuming a 50% of energy recovery in the cooling section, shows that values between 2.2 and 3.4 kJ kg^{-1} CO_2 can be required under the studied conditions. Furthermore, as can be noted from Figure 27 (b), most of the energy and productivity output for the lowest flue gas flowrate studied relies on the lower limit of both the energy consumption and productivity.

To have a more objective perspective of how performance parameters such as energy consumption and production behave, only the results that presented both purity values above 88% mol and recovery above 90% were analyzed, as shown in Figure 28.

Figure 28. (a) CO_2 purity vs. CO_2 recovery and (b) Productivity vs. Energy consumption at different gas flowrates (100, 120 and 145 $Nm^3\ h^{-1}m^{-2}$) for specification of purities > 88% mol and recoveries > 90%.

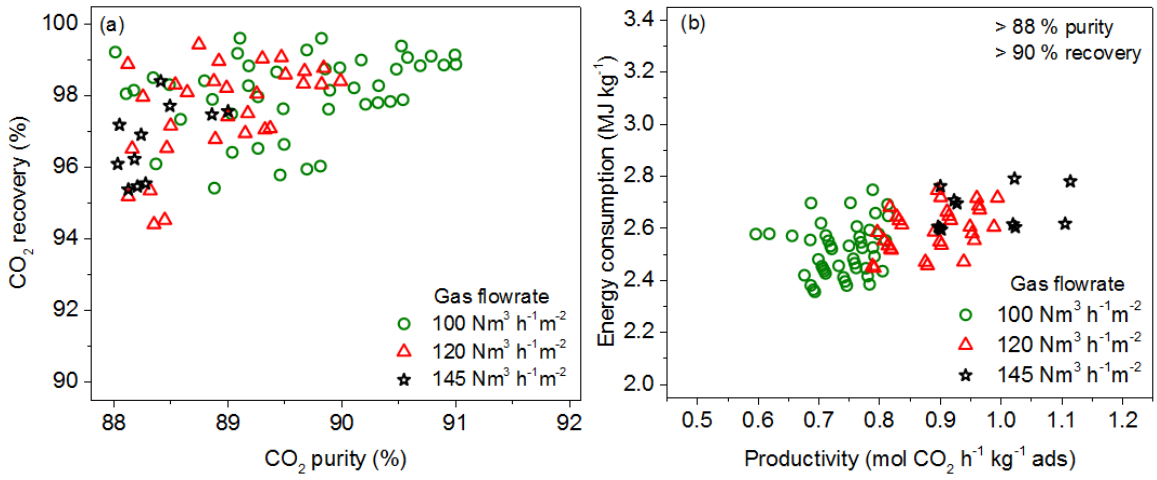

Source:Morales-Ospino et al. (2021)

Figure 28(a) confirms that lower flue gas flowrates may be more advantageous with regards to purity and recovery, whereas Figure 28(b) shows that enhanced productivity numbers can be achieved with higher feed gas flowrates without any apparent extra penalty of energy consumption. In the same fashion, it is worth noticing that results with the poorest purity and recovery performance at 145 $Nm^3\ h^{-1}m^{-2}$ in Figure 27(b) are those with the lowest productivities and largest-energy demand outcome since they disappeared from Figure 27(b) to Figure 28(b).

5.3.4.2. Effect of solid flowrate

Simulations varying the solid flowrate F_s and the adsorbent residence time, as described in Figure 26, but keeping a fixed flue gas flowrate of 100 $Nm^3\ h^{-1}m^2$, were carried out to show the effect of F_s on the performance parameters. A fixed flue gas flowrate allowed to represent the different F_s in terms of solid/gas mass flow ratio (kg of

solid per kg of gas). The results shown in Figure 29 unveil that the four key performance parameters displayed a similar behavior regardless the residence time employed.

Figure 29. Key performance parameters ((a) Recovery, (b) Purity, (c) Energy consumption and (d) Productivity) vs. solid/gas flowrate ratio at 100 $Nm^3\ h^{-1}m^{-2}$, for various adsorbent residence times and regeneration temperature of 240 °C.

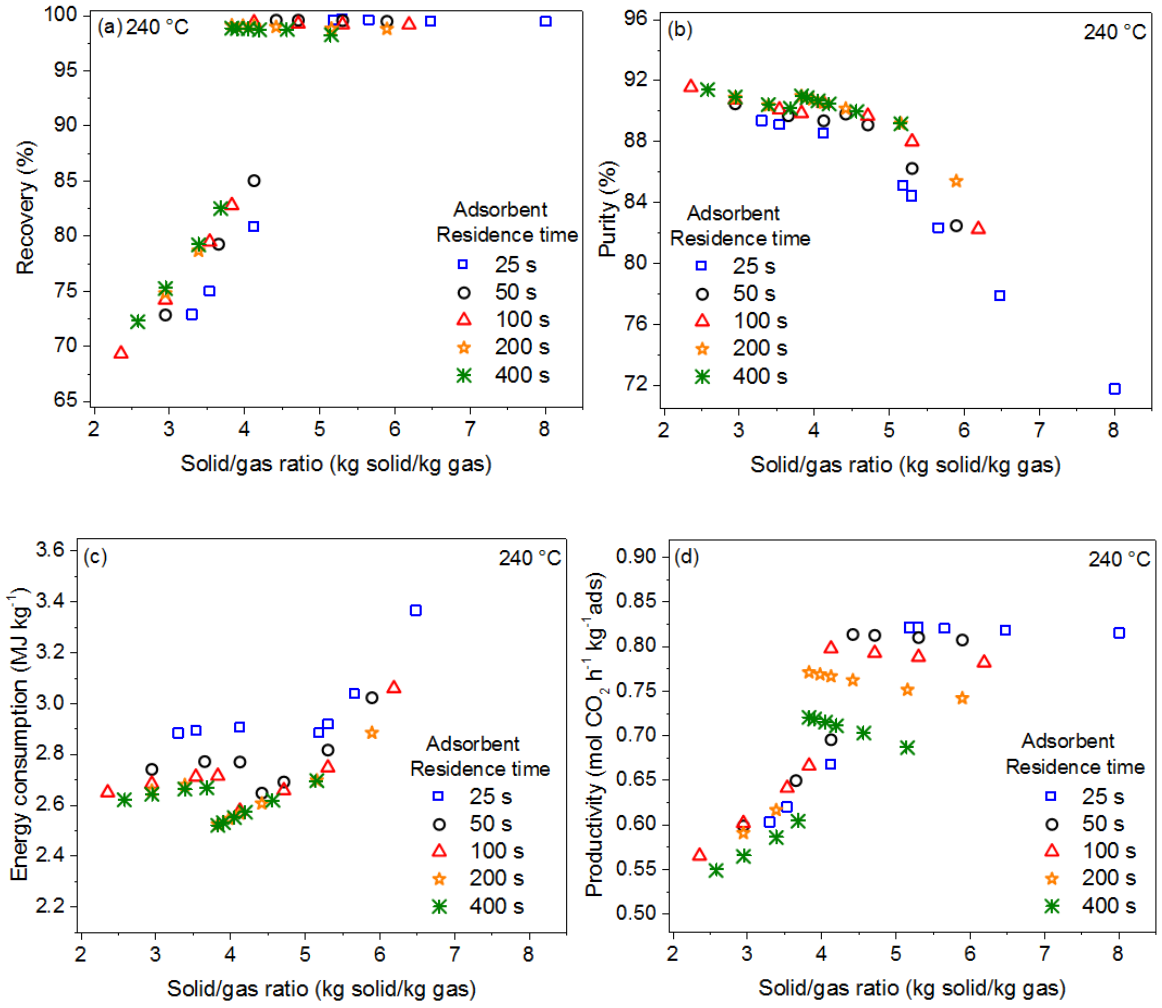

Source:Morales-Ospino et al. (2021)

Additionally, the data gathered in the simulations suggests that CO_2 recovery and productivity trends seemed to have a maximum value while the specific energy consumption a minimum. The solid/gas ratio at which the above observation occurs can be considered as the minimum solid/gas flow rate ratio at which CO_2 recovery is maximized. This “critical solid/gas flowrate ratio” is very similar for all the simulated residence times with the exception of 25 s. For instance, at a regeneration temperature of

240 °C in Figure 29(a), the critical solid/gas flow rate ratio is around 5.3 for a residence time of 25 s but for the others is ca. 4. At that point, it is equally important to note that a subtle increase of the solid/gas flowrate ratio may cause a significant growth in the CO_2 recovery. However, upon further increase of the solid/gas flowrate ratio, the CO_2 recovery stabilizes in a maximum value. Therefore, increasing indefinitely the solid flow rate does not obligatorily yield a better CO_2 capture performance.

Figure 29(b) illustrates how CO_2 purity exhibits a subtle pulse behavior at the critical solid/gas flow rate and then goes down continuously past the optimum solid/gas ratio. For the energy consumption, in Figure 29(c), it is possible to identify that the minimum specific energy demand arises at the optimum solid/gas ratio, which maximizes recovery. Finally, Figure 29(d) indicates that the CO_2 productivity exhibits its highest value at the local optimum solid/gas flow rate ratio. This maximum productivity value decreases as the adsorption residence time is increased. The reason might be related to larger amount of solids required in the whole MBTSA system as the residence time is increased in the adsorption section. As shown above, this “critical” or “optimum” solid/gas flowrate ratio is key to maximize the performance of the MBTSA system. In order to help understand the conditions at which this critical ratio may occur, Figures 30 and 31 might be very helpful.

As exemplified in Figure 30, the solid material and the gas flow in opposite directions. The adsorbent comes in the adsorption section at $z^*=1$ (top of the adsorption section) and T ~ 55 °C and leaves the section at $z^*=0$ (bottom of the adsorption unit) with a temperature between 70 and 85 °C. The temperature profile in Figure 30 shows that the sharp front in the temperature wave is given by the liberation of the CO_2 heat of adsorption. Similarly, the CO_2 molar fraction profile inside the adsorption section in Figure 31 illustrates that the flue gas enters the moving bed at $z^*=0$ with CO_2 molar fraction (y_{CO2}) of 0.15, and is discharged at $z^*=1$ and y_{CO2}~0. In this case, the sharp front in the composition wave corresponds to the rapid uptake of CO_2 by the solid material.

At the conditions shown in Figures 30/31, the optimum solid/gas ratio (~3.83) occurs when the heat generated by the adsorption process is maintained within the adsorber and is not carried away with the effluent gas. This means that CO_2 recovery is maximized when the CO_2 concentration front remains within the adsorption zone but

somewhere closer to the top of the adsorber, as seen in Figure 31; otherwise it would contaminate the N_2 enriched stream. Under these circumstances, both the *T* and y_{CO2} profiles display a “step” shape. Solid/gas mass flow ratios above the optimum will only displace these “step curves” to the left (i.e., towards the gas inlet), but no further improvement in recovery or productivity might be obtained.

Figure 30. Temperature profile within the adsorption section for different solid/gas mass flow ratios.

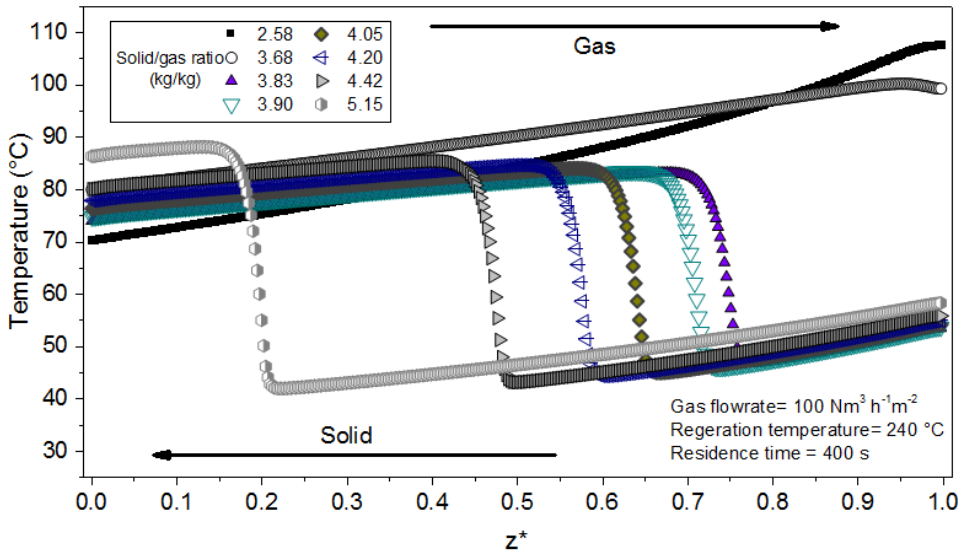

Source:Morales-Ospino et al. (2021)

Figure 31. CO_2 mol fraction profile within the adsorption section for different solid/gas mass flow ratios.

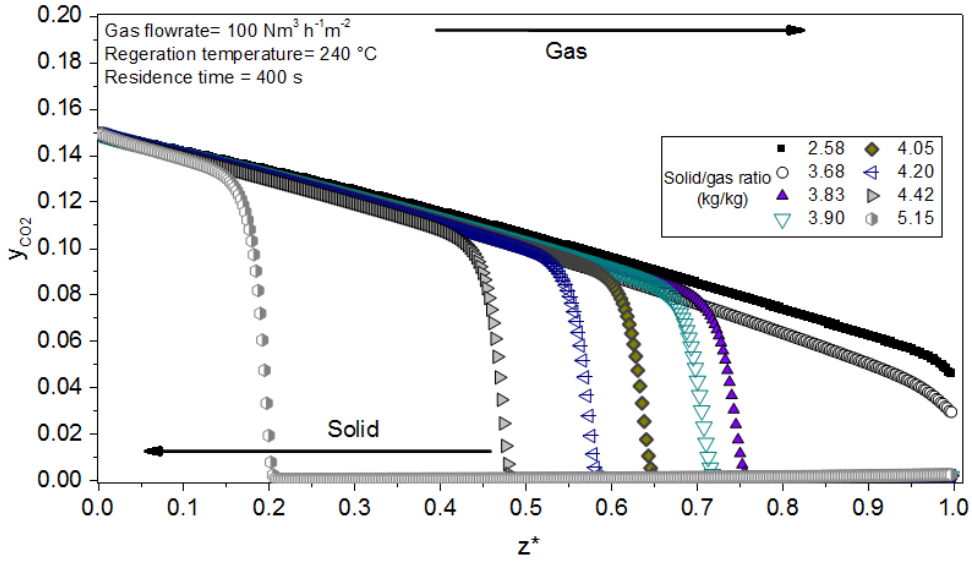

Source:Morales-Ospino et al. (2021)

The optimum solid/gas mass flow ratio for a fixed flue gas flowrate may vary depending on parameters such as the resident time or the regeneration temperature; however, it seems that there is an effective range of solid/gas ratios as can be observed in Figure 32, which is very similar for the three evaluated regeneration temperatures. Similarly, one can appreciate from Figure 32 that as long as the feed gas flowrate is increased, higher solid flowrates are required to reach the optimum solid/gas mass flow ratio.

Figure 32. Adsorbent residence time vs. optimum solid/gas ratio at different gas flowrates (100, 120 and 145 $Nm^3\ h^{-1}m^{-2}$). The points represent the highest CO_2 capture rates at different regeneration temperatures (200, 220 and 240 °C).

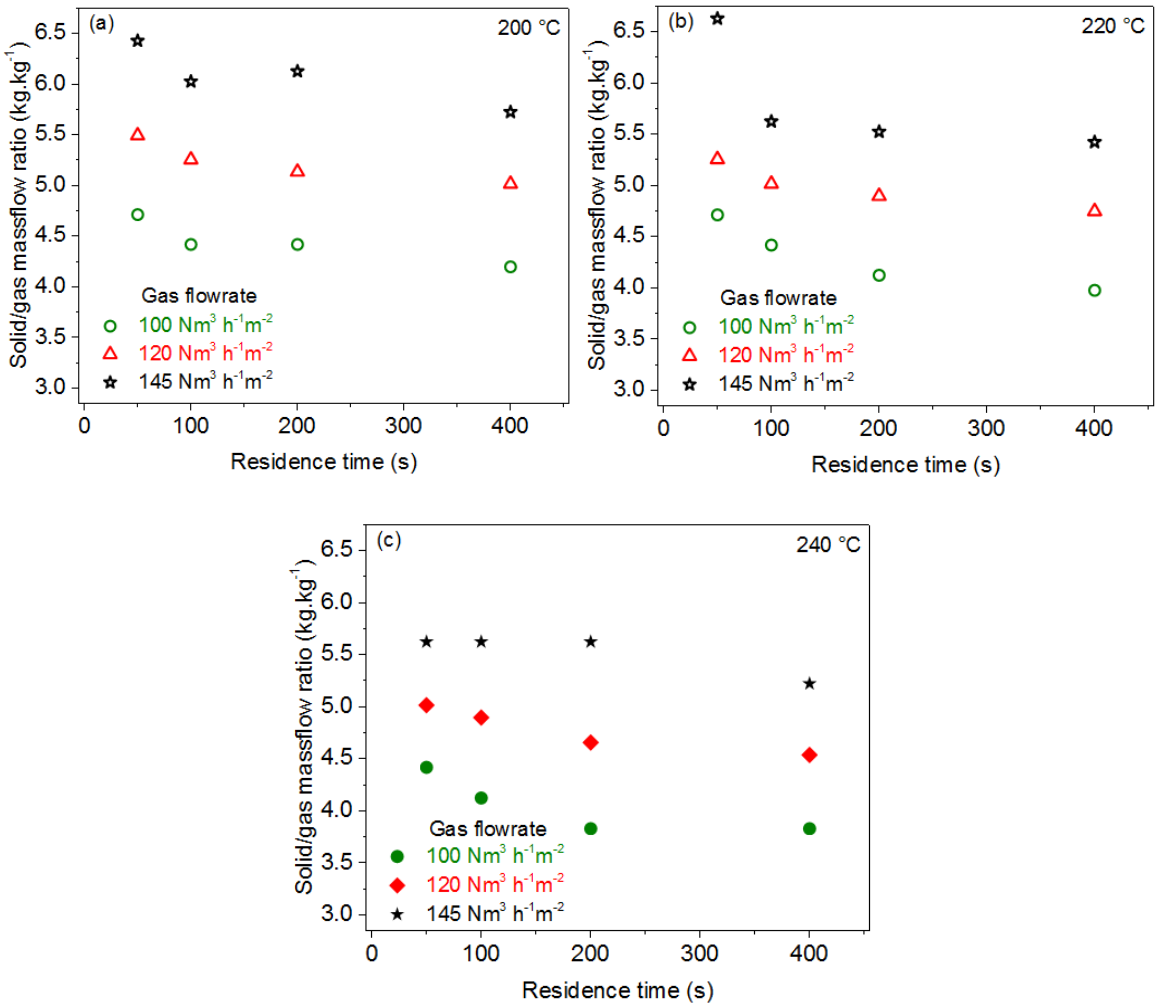

Source:Morales-Ospino et al. (2021)

5.3.4.3. Effect of regeneration temperature

In this section, the discussion will point to the effect of the regeneration temperature, employed in the desorption section, on the performance of the MBTSA and will center on the simulated results at which the solid/gas flow rate ratio is optimum. Since the residence time of 25 s was only beneficial to obtain a slightly improved productivity performance as demonstrated in section 5.3.4.2, it was not included in the ongoing discussion. The simulated results with the highest CO_2 recoveries for each residence time (from 50 to 400 s) at the three selected regeneration temperatures (200, 220 and 240 °C) for a flue gas flowrate of 100 $Nm^3\ h^{-1}m^{-2}$ are shown in Figure 33.

Figure 33. Adsorbent residence time vs. (a) CO_2 purity, (b) CO_2 recovery, (c) energy consumption and (d) productivity at 100 Nm3 h^{-1} m^{-2}. The points represent the highest CO2 recoveries at different regeneration temperatures (200, 220 and 240 °C)

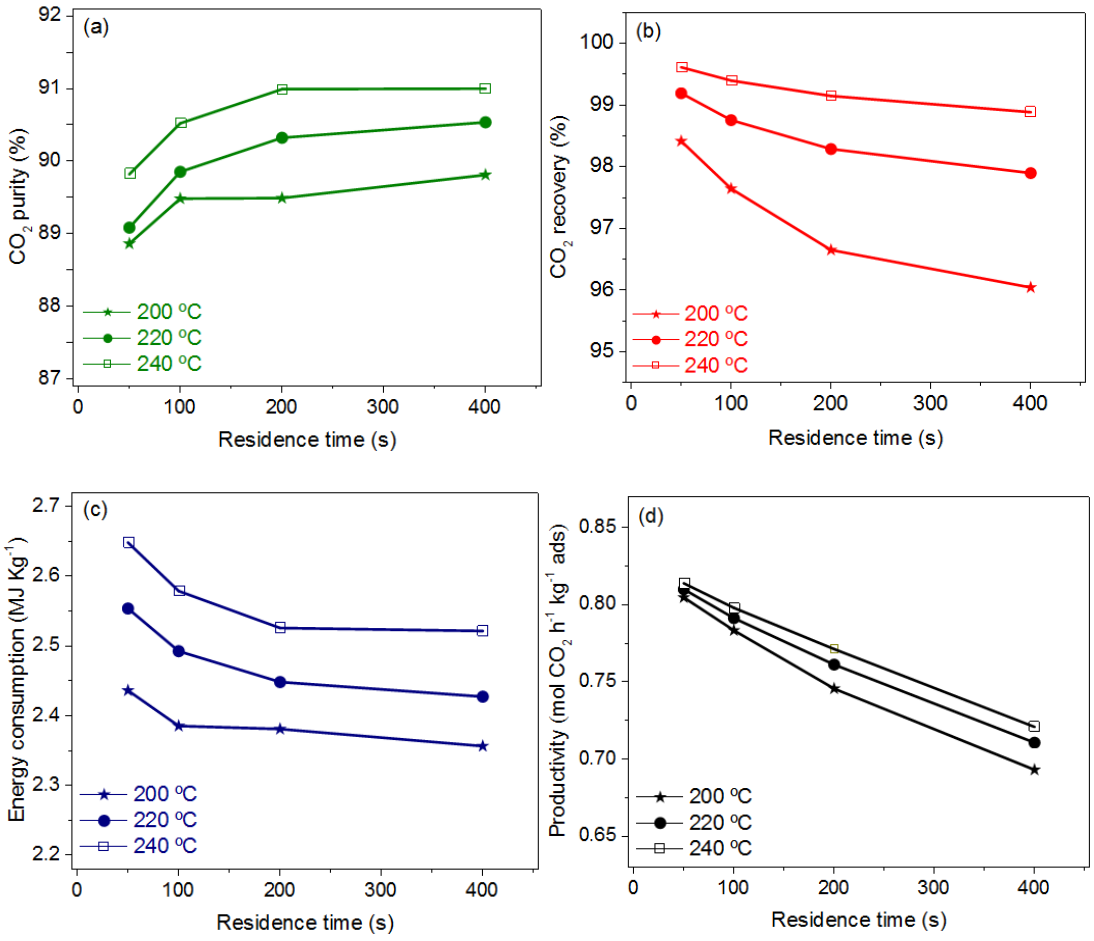

Source:Morales-Ospino et al. (2021)

The results in Figures 33 (a) and (b) prove that higher values of the regeneration temperatures (e.g., 240 °C) are clearly more convenient in terms of both CO_2 recovery and purity at every residence time evaluated. Figure 25 (b) also depicts that CO_2 recovery values up to 99% are achievable at a regeneration temperature of 240 °C though at 200 °C, the values might fall to 95.5%.

The CO_2 purity in the product stream barely changed. For example, Figure 33(a) indicates that purity fluctuates in a narrow range, i.e., between 89 and 91%mol. As previously observed in Figure 27(a), the variables studied in this work appeared to have little impact on the purity values of CO_2. This finding lends support to the claim that purity is likely to be associated with the nature of the solid material, more specifically, the selectivity of adsorbent to capture CO_2 against N_2. Nonetheless, we might reach enhanced purity values at higher regeneration temperatures and lower flue gas flowrates.

According to Figure 33(c) employing a higher outgassing temperature may actually require more energy per kg of CO_2 captured. However, a closer look at the data suggests that the specific energy demand is not considerably penalized by the increase on the regeneration temperature and exhibits a maximum energy consumption difference of ca. 0.3 MJ kg^{-1} between the lowest and highest regeneration temperature. The reason of this performance result may rely on the compensation effect of the energy recovery occurring in the cooling section. Despite a higher desorption temperature can require more energy to carry the CO_2 off the adsorbent, it may well end in a higher energy recovery since the solid abandons the desorption section with a higher temperature.

Similarly, Figure 33(c) shows that all the values of the specific energy consumption obtained in the simulations (between 2.3 and 2.7 MJ kg^{-1} of CO_2) are below typical values of the specific thermal energy for regeneration consumed by amine based-absorption capture systems (i.e., 3.2 – 3.6 MJ kg^{-1} of CO_2) (Sanchez Fernandez et al. 2014). As previously discussed, all our simulations were premised on the assumption that 50% of the sensible energy from the hot adsorbent can be recovered in the cooling zone. Let us now consider several cases on which the percentage of recovery is reduced as illustrated in Figure 34. The results shown in Figure 34 indicate that, up to a 20% of energy recovery, the energy demand values would still be competitive against liquid amine absorption.

Figure 34. Adsorbent residence time vs. Energy consumption at 100 $Nm^3\ h^{-1}\ m^{-2}$. The points represent the highest CO_2 capture rates at a regeneration temperature of 240 °C.

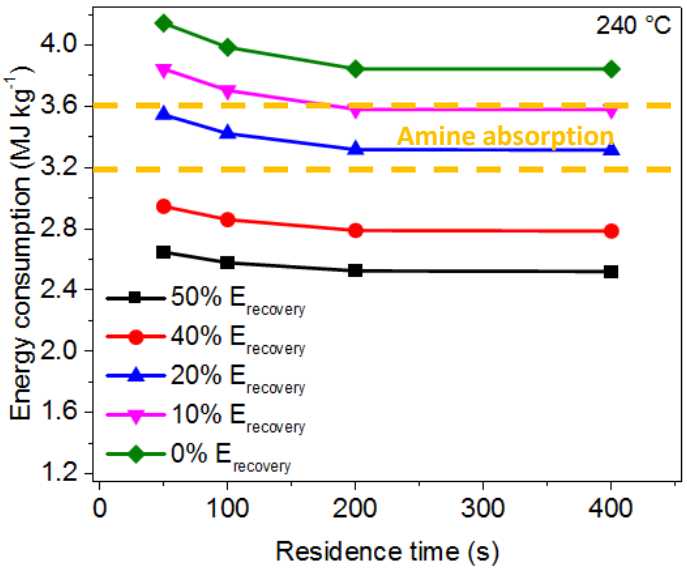

Source:modified from Morales-Ospino et al. (2021)

Moreover, the productivity performance is improved with the increase in the regeneration temperature and shorter residence times as observed in Figure 23 (d). As it is well known, productivity has a determining impact on the capital costs of a plant and, therefore, maximizing it should be an objective of any adsorption separation process. In other words, the higher the productivity, the more efficient the separation process can be, since less adsorbent is required to recover the same amount of CO_2. The key performance parameters obtained at a flue gas flowrate of 100 $Nm^3\ h^{-1}\ m^{-2}$, 240 °C of regeneration temperature and 100 s of residence time were compared to other performance parameters of previously published work in the literature for CO_2 capture as can be observed in Table 17. Although the compilation of references in Table 17 contemplate diverse regeneration strategies, contactor types and even different CO_2 partial pressure in the feed, it is possible to acknowledge that the simulated results of the performance parameters of the studied MBTSA system are promissory. However, since there is not optimized experimental data with a similar moving bed configuration, adsorbent and gas mixture components used in this work available in the literature, it was challenging to validate the model with experimental data. Additionally, moving beds may exhibit different configurations like the number of sections or heat exchanger configurations, which

imposes a greater difficulty to validate the moving bed models from published experimental data.

Table 17. Comparison of key performance parameters of selected published works for CO_2 capture

Regeneration mode	CO_2 conc. (% vol.)	Contactor Type	CO_2 purity (%)	CO_2 recovery (%)	Energy (MJ/kg)	Productivity (kg/ h m^3 ads)	Reference
Two-stage VSA (Coal)	16.5	Fixed	95.6	90.2	2.44[b]	65.2[b]	Wang et al. (2013)
VSA-two-stage	15	Fixed	96.5	93.4	2.64[a,c]	20.9[c]	Wang et al. (2012)
TSA-direct-CO_2	15	Fixed	91	83.6	4.50[c]	32.9[c]	Ntiamoah et al. (2016)
TSA-heat integration for sensible heat recovery	15	Simulated moving	-	-	2.53[c]	-	Jung et al. (2018)
VPSA-three-bed seven-step	15	Fixed	85	79	2.37[b]	83.7b	Liu et al. (2012)
TSA-indirect	12	Fixed	0.97	0.77	4.07[c]	46.5[c]	Joss et al. (2017)
TSA-indirect with steam purge	14	Fixed-monolith	95.6	85.4	3.59[c]	228.4[c]	Plaza et al. (2017b)
TSA-steam + CO_2 Heat integration in adsorber and desorber (Coal)	13.8	Circulating bubbling fluidized	-	-	2.49[c]	42[c]	Zhang et al. (2017a)
TSA-indirect with vacuum and heat pump- CO_2 purge	13.4	Multistage fluidized	96	90	2.8[a,c]	68.3[b]	(Zaabout et al. 2017, Dhoke et al. 2020)
Thermally couple column-TSA (Coal)	13.2	Fast fluidized bed	-	85	1.73[c]	-	(Vogtenhuber et al. 2018)
VSA-membrane	12.6	Fixed bed membrane	95	-	4.1[b]	10.8[b]	(Warmuzinski et al. 2015)
TSA- indirect	12.5	Fixed	99	79	-	-	(Tlili et al. 2009)
VPSA-two-stage	10	Fixed	95.3	74.4	3.61[a,c]	26.8[c]	(Shen et al. 2012)
TSA-indirect with purge-optimized	10	Fixed	95	81	3.23[c]	43.1[c]	(Clausse et al. 2011)
TSA-indirect with steam (without heat integration)	5.15	Moving	95.1	96	2.21[c]	-	(Mondino et al. 2019)
TSA-indirect with steam with heat integration)	5.15	Moving	95.1	96	1.46[c]	-	(Mondino et al. 2019)

TSA-steam + CO_2 Heat integration in adsorber and desorber (natural gas)	4.1	Circulating bubbling fluidized	-	-	2.54[c]	42[c]	Zhang et al. (2017a)
TSA-indirect (with energy recovery)	15	Moving	90	99	2.6[c]	44.1[c]	This work

a*Electric efficiency of 20% is assumed in the conversion of electrical energy to thermal energy for regeneration, excluding electricity required forcompression and pressure drop.* ***b****Experimental measurement.* ***c****Model prediction*.
Source: Information taken from Dhoke et al. (2021)

In fact, most of the available studies addressing moving beds for Carbon Capture are based mainly on simulated results such as the works of Kim et al. (2013), Son et al. (2014), Grande et al. (2017), Mondino et al. (2017), Mondino et al. (2019), Zhao et al. (2021). Some exceptions include the experimental bench tests reported in the works of Okumura et al. (2017) & Okumura et al. (2014), which demonstrated that values of CO_2 recoveries ca. 90% can be achieved by using an impregnated porous material with an amine compound. However, no further details regarding the adsorbent is provided neither the equilibrium nor the kinetic data, heat exchange configuration and sizing, and so on, which hinders the possibility to replicate the experimental results by simulations.

To the best of my knowledge, the only work reporting both experimental data from lab scale tests and simulations is the study carried out by Son et al. (2016). Nevertheless, their study proposed an intermittently moving bed adsorption process so that the solid is moving discontinuously through the operation of on–off valves instead of the traditional uninterrupted solid moving. This fact implies a different modelling approach to incorporate the operational sequence of the valves for the solid migration from one section to another. Additionally this moving bed displayed a different configuration. There is only two sections instead of three, since the adsorbent cooling step is performed in the adsorption section itself with an integrated heat exchanger. In summary, this would imply making so many adjustments to the original model that it would blur the original idea of validating the model proposed in the manuscript with experimental data. However, we can relate some patterns observed in the simulations of this work with the results obtained in the mentioned study. Son et al. (2016) validated their model by comparing the model's purity and recovery values with the experimental data. Once validated, other topics with simulations were explored in the work. For instance, the concentration profiles in the adsorption section of the moving bed in Figure 6 below is consistent with the molar fraction profiles shown in this research.

Once validated, other topics with simulations were explored. For instance, the concentration profiles in the adsorption section of the moving bed in Figure 6 below is consistent with the molar fraction profiles shown in our work. On this particular point, Son et al. (2016) commented the following statement: "*When the profile front is in a top region, a small change in the bed height may incur a large decrease in CO_2 recovery as in the operation policies P7 and P8. When the profile front is in a middle region by a moderate cycle time (moderate solid velocity), a change in the bed height has only a minor effect on the separation performance as in the operation policies P3 and P4."* The policies in their work represent a set of operating conditions.

The top region shown in Figure 36 (a) is when the CO_2 front is still conveyed outwards, so the CO_2 capture rate decreases; nevertheless, a subtle increase in the solid flowrate can lead to a more enhanced CO_2 recovery as we demonstrated with with our results.

Figure 35.Steady state concentration profiles for (a) low and (b) high solid velocities

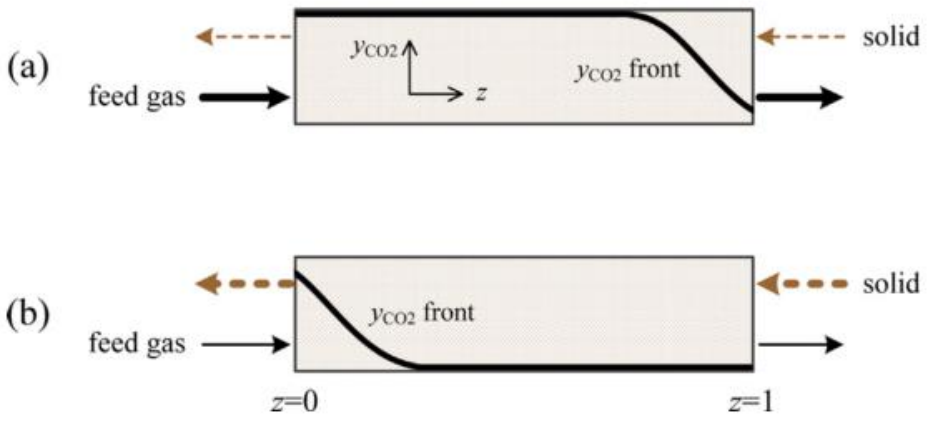

Source: Son et al. (2016)

The results shown in Figure 37 also agreed with the purity and recovery trends shown in our simulations. While purity has a continuous decreasing profile as the solid velocity increases, the CO_2 recovery is gradually increasing until stabilizing at a maximum value. For the sake of clarity, in this research, this trend was presented with the solid flowrate instead of the solid velocity. However, it was equally defined the solidflowrate in

terms of the solid velocity by Equation 35, where it is evident that increasing the solid velocity also implicates the rise of the solid flowrate.

Figure 36. Purity and recovery trend preformance against solid velocity

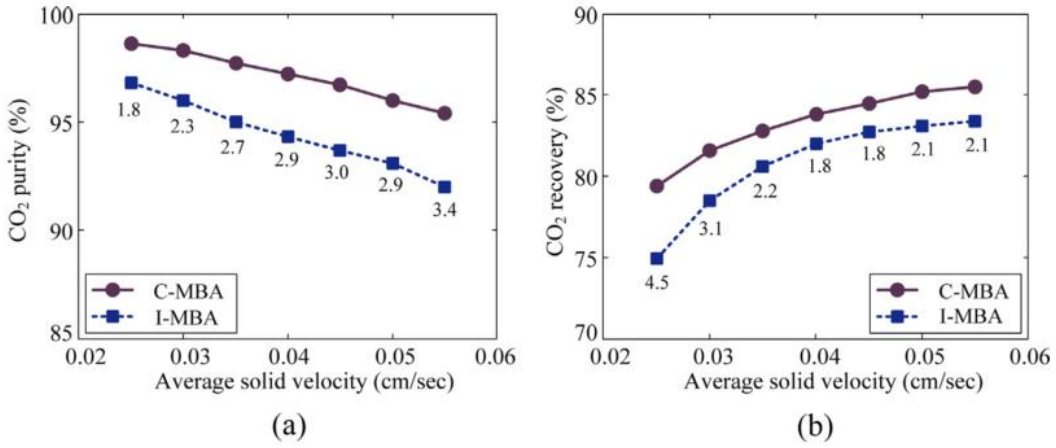

Source: Son et al. (2016)

From the bench tests of the works of Okumura (2014) & (2017), it was possible to confirm that by adequate operating conditions in a moving bed, 99% of CO_2 recovery can be reached. Given these points, despite the previous comparison of trends regarding purity, recovery and the concentration front of CO_2 might not be a “true” validation of the simulation results, several of the observations made in the work of Son et al (2016) are in agreement with the findings of our study. Additionally, the plant tests of Okumura (2014) & (2017) confirm the possibility to obtain capture rates as to values of 99% as equally shown in this work simulations. Consequently, these similarities might be a good indication that the proposed model responds logically according to previous validated/experimental moving bed data.

5.3.4.4. Effect of the feed temperature

The gas temperature at inlet was equally evaluated through a set of simulations with some fixed input variables, as shown in Figure 38, but varying the standard inlet temperature (50 °C) for a lower value (30 °C) and a higher value (70 °C). The results shown in Figure 38 suggest that using a lower feed temperature did not yield a prominent enhanced performance on the MBTSA unit as we could intuitively expect. Actually, with

the exception of the specific energy requirement, little disparity on the key performance parameter performance was observed.

Figure 37. Effect of the feed temperature on the MBTSA key performance parameters: (a) CO_2 recovery and purity, and (b) Energy consumption and productivity.

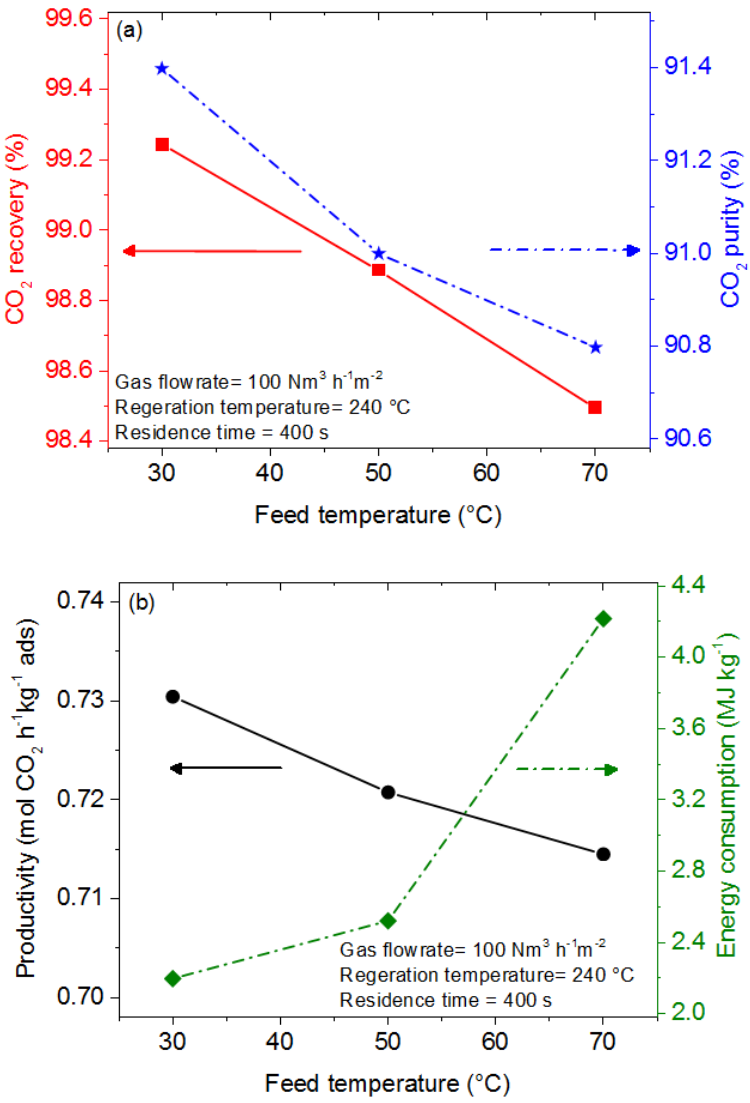

Source: Morales-Ospino et al. (2021)

The abrupt escalation in the specific energy consumption at a feed temperature of 70 °C is due to the greater energy penalty imposed by the flue gas drying process as shown in Table 18. Since the post-combustion flue gas is expected to be saturated with water vapor, the more elevated the inlet temperature, the higher the partial pressure of

the water in the flue gas. For that reason, a larger amount of moisture shall be removed, which inexorably involves a more energy-demanding drying operation. The breakdown of the energy duty provided in Table 18 also shows that the major energy demand is that required to desorb the CO_2 from the solid material ($E_{desorption}$) while the energy duty to transport back the adsorbent to the top of the adsorption section displayed the lowest energetic requirement. In the same way, one can notice the importance of the energy recovered from the hot adsorbent ($E_{recovery}$) to preserve the MBTSA energetic requirements competitive against absorption-based carbon capture processes.

Table 18. Breakdown of the energy duty items

Inlet temperature	Net energy consumption	$E_{desorption}$	E_{drying}	$E_{potential}$	$E_{recovery}$
°C	(MJ kg^{-1})	(MJ kg^{-1})	(MJ kg^{-1})	(MJ kg^{-1})	(MJ kg^{-1})
30	2.20	+3.39	+0.04	+1.74E-06	-1.23
50	2.52	+3.53	+0.32	+1.89E-06	-1.32
70	4.22	+3.60	+1.99	+1.43E-02	-1.37

Source: own authorship

The poor utility of adsorbents like zeolite 13X under wet ideal conditions (CO_2 + N_2 + H_2O) and the probably expensive drying operation required by zeolite 13X for post-combustion CO_2 capture has already been suggested by (Joos et al. (2013)). While this may possibly be true, as a rebuttal to this point, it might be argued that in this work we have put forward the operating conditions at which this can certainly apply for a specific separation process. According to the results generated by this study, in a MBTSA CO_2 capture process, it is feasible to obtain promising performance to separate CO_2 even with a pre-drying of the flue gas provided that the temperature of the feed gaseous mixture is around 50 °C or below.

6. CONCLUSIONS

In this work, Type X and type A zeolites synthesized from coal fly ash via ash fusion method followed by hydrothermal reaction were evaluated as potential adsorbents to capture CO_2. The samples were later compared to benchmark adsorbents for CO_2 capture such as commercial zeolite 13X and 4A, so that all the four samples underwent the same gas characterization and equilibrium experiements. Afterwards, commercial zeolite 13X was selected among the four adsorbents to carry out a parametric study of a Moving Bed Temperature Swing Adsorption (MBTSA) unit for post-combustion CO_2 capture under different operating conditions by means of process simulations. Based on our findings, herein the most outstanding conclusions were divided into two main groups: firstly, those related to the synthesis and characterization of the zeolitic materials and secondly, the conclusions derived from the adsorption-based separation process simulation.

From the gas characterization and adsorption metrics results, the main conclusions can be summarized as follows:.

- The micropore volume of the XFF sample obtained from the N_2 and CO_2 gas adsorption characterization displayed similar values suggesting that the volume of ultramicropores is practically negligible for this sample. Conversely, commercial zeolite 13X micropore volume from CO_2 adsorption essay was greater than that obtained from N_2 experiments, indicating the existence of smaller pores that were not reached during the N_2 characterization test at 77K.
- The synthesized zeolites displayed slightly lower CO_2 adsorption uptakes than the commercial samples between 50 and 70 °C and up to 1 bar. Moreover, Type A zeolites happened to be more selective to capture CO_2 over N_2 than type X especially at low temperatures (e.g., 50°C).
- The water vapor/CO_2 adsorption study on the samples proved that the hydrophilic character of the zeolites inhibit them to be employed under real post-combustion conditions due to the severe drop of the CO_2 adsorption capacity with the presence of moisture. An upstream drying process aiming at dehydrating the flue gas is recommended to enable the utilization these adsorbents in a CO_2 capture process facility.

In summary, on the basis of the characterization, CO_2 uptakes and selectivity results, the synthesized adsorbents can be considered as promissory materials to capture CO_2 under

dried post-combustion scenario. Not only they matched well the characteristics of their commercial counterparts but also they were prepared from a widely available and cheap precursor such as the fly ash from coal-fired power plants.

From the MBTSA simulations with the sample Zeo13X, the most significant conclusions, under the studied conditions, are described below:

- CO_2 recovery rates of 99% and purities around 91 %mol were attained. Furthermore, it was possible to corroborate that decreasing the feed gas flowrate may lead to reach CCS specification targets; though, it reduces the flue gas volumetric processing capacity of the MBTSA unit.
- CO_2 purity in the product stream appeared to be a less flexible parameter than CO_2 recovery through the variation of the studied process variables. Purity fluctuation occurred in a relatively narrow range, mostly between 82 and 92%mol, which might indicate that this parameter is closely related to the selectivity of the adsorbent.
- Once an energy recovery configuration has been considered in the cooling section, the use of higher regeneration temperatures for the degasification of the adsorbent does not impose any substantial energy penalty as one could expect. In fact, the net energy consumption is more sensitive to increasing the feed temperature due to the greater amount of water vapor that must be removed from the flue gas.
- The estimated specific energy consumption is comparable to the values reported in the literature for amine absorption processes when at least 20% of the energy recovery in the cooling section is assumed, suggesting the MBTSA process could be an attractive alternative for post-combustion CO_2 capture.
- Determining an optimal solid/gas mass flow ratio for a particular set of operating conditions is decisive, because there is a limit to maximizing both CO_2 recovery and productivity by raising the solid/gas ratio in the adsorber. Additionally working with solid/gas ratios beyond the optimal appears to rise the net energy consumption.
- At reasonably low feed gas flowrates, i.e., 100 $Nm^3.h^{-1}m^{-2}$, higher regeneration temperatures (240 ^oC), and a gas/solid mass flow ratio ratio between 3.5 and 4.5 (depending on the adsorbent residence time) lead to a relatively improved performance.

REFERENCES

AHMARUZZAMAN, M. A review on the utilization of fly ash. **Progress in Energy and Combustion Science**, v. 36, n. 3, p. 327-363, 2010.

AQUINO, T. **Synthesis of type X zeolites from mineral coal fly and bottom ashes for CO2 capture**. 2018. (Doctorate in Chemical Engineering). UFSC. 2018.

AQUINO, T. F. d.*, et al.* CO2 adsorption capacity of zeolites synthesized from coal fly ashes. **Fuel**, v. 276, p. 118143, 2020.

BAE, T.-H.*, et al.* Evaluation of cation-exchanged zeolite adsorbents for post-combustion carbon dioxide capture. **Energy Environ. Sci.**, v. 6, n. 1, p. 128-138, 2013.

BAHAMON, D. and VEGA, L. F. Systematic evaluation of materials for post-combustion CO2 capture in a Temperature Swing Adsorption process. **Chemical Engineering Journal**, v. 284, p. 438-447, 2016.

BELVISO, C. State-of-the-art applications of fly ash from coal and biomass: A focus on zeolite synthesis processes and issues. **Progress in Energy and Combustion Science**, v. 65, p. 109-135, 2018a.

BELVISO, C. Ultrasonic vs hydrothermal method: Different approaches to convert fly ash into zeolite. How they affect the stability of synthetic products over time? **Ultrason Sonochem**, v. 43, p. 9-14, 2018b.

BEN-MANSOUR, R.*, et al.* Carbon capture by physical adsorption: Materials, experimental investigations and numerical modeling and simulations – A review. **Applied Energy**, v. 161, p. 225-255, 2016.

BERG, C. **The Hypersorption Process for Gas Fractionation**, in *3rd World Petroleum Congress*. 1951, World Petroleum Congress: The Hague, the Netherlands. p. 12.

BERTSCH, L. and HABGOOD, H. W. An Infrared Spectroscopic Study of Adsorption of Water and Carbon Dioxide by Linde Milecular Sieve X. **Journal of Physical Chemistry**, v. 67, n. 8, p. 1621-&, 1963.

BHATTACHARYYA, D. and MILLER, D. C. Post-combustion CO 2 capture technologies — a review of processes for solvent-based and sorbent-based CO 2 capture. **Current Opinion in Chemical Engineering**, v. 17, p. 78-92, 2017.

BHOWN, A. S. and FREEMAN, B. C. Analysis and status of post-combustion carbon dioxide capture technologies. **Environ Sci Technol**, v. 45, n. 20, p. 8624-32, 2011.

BINGRE, R., LOUIS, B., and NGUYEN, P. An Overview on Zeolite Shaping Technology and Solutions to Overcome Diffusion Limitations. **Catalysts**, v. 8, n. 4, p. 163, 2018.

BIRD, R. B., STEWART, W. E., and LIGHTFOOT, E. N. **Transport Phenomena**. New York: Wiley International, 2006.

BRANDANI, F. and RUTHVEN, D. M. The effect of water on the adsorption of CO2 and C3H8 on type X zeolites. **Industrial & Engineering Chemistry Research**, v. 43, n. 26, p. 8339-8344, 2004.

BRUNAUER, S., EMETT, P. H., and TELLER, E. Adsorption of gases in multimolecular layers. **Journal of the American Chemical Society**, v. 60, p. 309–319, 1938.

BRUNETTI, A.*, et al.* Membrane engineering for environmental protection and sustainable industrial growth: Options for water and gas treatment. **Environmental Engineering Research**, v. 20, n. 4, p. 307-328, 2015.

BUI, M.*, et al.* Carbon capture and storage (CCS): the way forward. **Energy & Environmental Science**, v. 11, n. 5, p. 1062-1176, 2018.

BUKALAK, D., MAJCHRZAK-KUCĘBA, I., and NOWAK, W. Assessment of the sorption capacity and regeneration of carbon dioxide sorbents using thermogravimetric methods. **Journal of Thermal Analysis and Calorimetry**, v. 113, n. 1, p. 157-160, 2013.

CAZORLA-AMORÓS, D.*, et al.* CO2 As an Adsorptive To Characterize Carbon Molecular Sieves and Activated Carbons. **Langmuir**, v. 14, n. 16, p. 4589-4596, 1998.

CLAUSSE, M., MEREL, J., and MEUNIER, F. Numerical parametric study on CO2 capture by indirect thermal swing adsorption. **International Journal of Greenhouse Gas Control**, v. 5, n. 5, p. 1206-1213, 2011.

CHESTER, A. W. and DEROUANE, E. G. **Zeolite Characterization and Catalysis, A tutorial.** Springer, 2009.

CHU, F.*, et al.* CO2 capture using MEA (monoethanolamine) aqueous solution in coal-fired power plants: Modeling and optimization of the absorbing columns. **Energy**, v. 109, p. 495-505, 2016.

DANACI, D.*, et al.* Exploring the limits of adsorption-based CO2 capture using MOFs with PVSA – from molecular design to process economics*.* **Molecular Systems Design & Engineering**, v. 5, n. 1, p. 212-231, 2020.

DAVIDSON, O.*, et al.* **IPCC Special Report on Carbon Dioxide Capture and Storage**. New York, 2005. 442 p.

DENG, L., XU, Q., and WU, H. Synthesis of Zeolite-like Material by Hydrothermal and Fusion Methods Using Municipal Solid Waste Fly Ash*.* **Procedia Environmental Sciences**, v. 31, p. 662-667, 2016.

DHOKE, C.*, et al.* Review on Reactor Configurations for Adsorption-Based CO2 Capture*.* **Industrial & Engineering Chemistry Research**, v. 60, n. 10, p. 3779-3798, 2021.

DHOKE, C.*, et al.* Demonstration of the Novel Swing Adsorption Reactor Cluster Concept in a Multistage Fluidized Bed with Heat-Transfer Surfaces for Postcombustion CO2 Capture*.* **Industrial & Engineering Chemistry Research**, v. 59, n. 51, p. 22281-22291, 2020.

DINDI, A.*, et al.* Applications of fly ash for CO2 capture, utilization, and storage*.* **Journal of CO2 Utilization**, v. 29, p. 82-102, 2019.

DO, D. D. **Adsorption Analysis: Equilibria and Kinetics**. London: Imperial College Press, 1998.

DO, D. D. and WANG, K. A new model for the description of adsorption kinetics in heterogeneous activated carbon*.* **Carbon**, v. 36, n. 10, p. 1539-1554, 1998.

DREISBACH, F., SEIF, A. H. R., and LOSCH, H. W. Measuring techniques for gas-phase adsorption equilibria*.* **Chemie Ingenieur Technik**, v. 74, n. 10, p. 1353-1366, 2002.

DUBININ, M. M. The Potential Theory of Adsorption of Gases and Vapors for Adsorbents with Energetically Nonuniform Surfaces*.* **Chemical Reviews**, v. 60, n. 2, p. 235-241, 1960.

DUBININ, M. M. and RADUSHKEVICH, L. V. The equation of the characteristic curve of activated charcoal*.* **Doklady Akademii Nauk USSR (Proceedings of the Russian Academy of Sciences)**, v. 55, p. 327-329, 1947.

FENG, W*., et al.* Synthesis of high quality zeolites from coal fly ash: Mobility of hazardous elements and environmental applications*.* **Journal of Cleaner Production**, v. 202, p. 390-400, 2018.

FIGUEROA, J. D*., et al.* Advances in CO2 capture technology—The U.S. Department of Energy's Carbon Sequestration Program*.* **International Journal of Greenhouse Gas Control**, v. 2, n. 1, p. 9-20, 2008.

FLORES, C. G*., et al.* Potassic zeolites from Brazilian coal ash for use as a fertilizer in agriculture*.* **Waste Manag**, v. 70, p. 263-271, 2017.

FOO, K. Y. and HAMEED, B. H. Insights into the modeling of adsorption isotherm systems*.* **Chemical Engineering Journal**, v. 156, n. 1, p. 2-10, 2010.

FUKASAWA, T*., et al.* Utilization of incineration fly ash from biomass power plants for zeolite synthesis from coal fly ash by microwave hydrothermal treatment*.* **Advanced Powder Technology**, v. 29, n. 3, p. 450-456, 2018.

FUKASAWA, T*., et al.* Utilization of incineration fly ash from biomass power plants for zeolite synthesis from coal fly ash by hydrothermal treatment*.* **Fuel Processing Technology**, v. 167, p. 92-98, 2017.

GIACCIO, G. M. and MALHOTRA, V. M. Concrete incorporating high volumes of ASTM Class F fly ash*.* **Cement, Concrete and Aggregates**, v. 10, n. 2, p. 88-95, 1988.

GOLLAKOTA, A. R. K., VOLLI, V., and SHU, C. M. Progressive utilisation prospects of coal fly ash: A review*.* **Sci Total Environ**, v. 672, p. 951-989, 2019.

GRANDE, C. A*., et al.* Development of Moving Bed Temperature Swing Adsorption (MBTSA) Process for Post-combustion CO 2 Capture: Initial Benchmarking in a NGCC Context*.* **Energy Procedia**, v. 114, p. 2203-2210, 2017.

GUTTIKUNDA, S. K. and JAWAHAR, P. Atmospheric emissions and pollution from the coal-fired thermal power plants in India*.* **Atmospheric Environment**, v. 92, p. 449-460, 2014.

HARLICK, P. J. E. and TEZEL, F. H. An experimental adsorbent screening study for CO2 removal from N-2*.* **Microporous and Mesoporous Materials**, v. 76, n. 1-3, p. 71-79, 2004.

HEDIN, N.*, et al.* Adsorbents for the post-combustion capture of CO2 using rapid temperature swing or vacuum swing adsorption. **Applied Energy**, v. 104, p. 418-433, 2013.

HENMI, T. Synthesis of Hydroxy-Sodalite (“Zeolite”) from Waste Coal Ash. **Soil Science and Plant Nutrition**, v. 33, n. 3, p. 517-521, 1987.

HOSSEINI, T., DE GIROLAMO, A., and ZHANG, L. Energy Evaluation and Techno-economic Analysis of Low-Rank Coal (Victorian Brown Coal) Utilization for the Production of Multi-products in a Drying–Pyrolysis Process. **Energy & Fuels**, v. 32, n. 3, p. 3211-3224, 2018.

HU, X.*, et al.* Diffusion mechanism of CO2 in 13X zeolite beads. **Adsorption**, v. 20, n. 1, p. 121-135, 2013.

HUAMAN, R. and LOURENCO, S. A Review on: CO2 Capture Technology on Fossil Fuel Power Plant. **Fundamentals of Renewable Energy and Applications**, v. 5, n. 3, p. 2015.

IQBAL, A.*, et al.* Synthesis and characterization of pure phase zeolite 4A from coal fly ash. **Journal of Cleaner Production**, v. 219, p. 258-267, 2019.

IZIDORO, J. d. C.*, et al.* Synthesis of zeolites X and A from fly ashes for cadmium and zinc removal from aqueous solutions in single and binary ion systems. **Fuel**, v. 103, p. 827-834, 2013.

IZIDORO, J. d. C.*, et al.* Characteristics of Brazilian coal fly ashes and their synthesized zeolites. **Fuel Processing Technology**, v. 97, p. 38-44, 2012.

JOOS, L., SWISHER, J. A., and SMIT, B. Molecular Simulation Study of the Competitive Adsorption of H2O and CO2 in Zeolite 13X. **Langmuir**, v. 29, n. 51, p. 15936-15942, 2013.

JOSS, L., GAZZANI, M., and MAZZOTTI, M. Rational design of temperature swing adsorption cycles for post-combustion CO 2 capture. **Chemical Engineering Science**, v. 158, p. 381-394, 2017.

JUNG, W.*, et al.* Simulated moving bed adsorption process based on a polyethylenimine-silica sorbent for CO2 capture with sensible heat recovery. **Energy**, v. 150, p. 950-964, 2018.

KIM, K.*, et al.* Performance Comparison of Moving and Fluidized bed Sorption Systems for an Energy-efficient Solid Sorbent-Based Carbon Capture Process*.* **Energy Procedia**, v. 63, p. 1151-1161, 2014.

KIM, K.*, et al.* Moving bed adsorption process with internal heat integration for carbon dioxide capture*.* **International Journal of Greenhouse Gas Control**, v. 17, p. 13-24, 2013.

KITTEL, J.*, et al.* Corrosion in MEA units for CO2 capture: Pilot plant studies*.* **Energy Procedia**, v. 1, n. 1, p. 791-797, 2009.

KNAEBEL, K. S. **TEMPERATURE SWING ADSORPTION SYSTEM**. 2013, Kent S. Knaebel & Associates, Inc.: USA. p. 12.

KO, D., SIRIWARDANE, R., and BIEGLER, L. Optimization of Pressure Swing Adsorption and Fractionated Vacuum Pressure Swing Adsorption Processes for CO2 Capture*.* **Industrial & Engineering Chemistry Research**, v. 44, p. 8084-8094, 2005.

KOYTSOUMPA, E. I., BERGINS, C., and KAKARAS, E. The CO 2 economy: Review of CO 2 capture and reuse technologies*.* **The Journal of Supercritical Fluids**, v. 132, p. 3-16, 2018.

LANGMUIR, I. The constitution and fundamental properties of solids and liquids*.* **American Chemical Society**, v. 38, n. 11, p. 2221-2295, 1918.

LE MOULLEC, Y.*, et al.* Process Modifications for Solvent-based Post Combustion CO2 Capture*.* **Energy Procedia**, v. 63, p. 1470-1477, 2014.

LEE, K.-M. and JO, Y.-M. Synthesis of zeolite from waste fly ash for adsorption of CO2*.* **Journal of Material Cycles and Waste Management**, v. 12, n. 3, p. 212-219, 2010.

LEPPÄJÄRVI, T.*, et al.* Utilization of Pisat temperature-dependency in modelling adsorption on zeolites*.* **Chemical Engineering Science**, v. 69, n. 1, p. 503-513, 2012.

LEUNG, D. Y. C., CARAMANNA, G., and MAROTO-VALER, M. M. An overview of current status of carbon dioxide capture and storage technologies*.* **Renewable and Sustainable Energy Reviews**, v. 39, p. 426-443, 2014.

LI, G., XIAO, P., and WEBLEY, P. Binary adsorption equilibrium of carbon dioxide and water vapor on activated alumina*.* **Langmuir**, v. 25, n. 18, p. 10666-75, 2009a.

LI, G.*, et al.* Competition of CO2/H2O in adsorption based CO2 capture. **Energy Procedia**, v. 1, n. 1, p. 1123-1130, 2009b.

LIANG, Z.*, et al.* Review on current advances, future challenges and consideration issues for post-combustion CO2 capture using amine-based absorbents. **Chinese Journal of Chemical Engineering**, v. 24, n. 2, p. 278-288, 2016.

LIANG, Z.*, et al.* Recent progress and new developments in post-combustion carbon-capture technology with amine based solvents. **International Journal of Greenhouse Gas Control**, v. 40, p. 26-54, 2015.

LIOR, N. Sustainable energy development: The present (2009) situation and possible paths to the future. **Energy**, v. 35, n. 10, p. 3976-3994, 2010.

LIU, L.*, et al.* Zeolite synthesis from waste fly ash and its application in CO2 capture from flue gas streams. **Adsorption**, v. 17, n. 5, p. 795-800, 2011.

LIU, Z.*, et al.* Onsite CO2 Capture from Flue Gas by an Adsorption Process in a Coal-Fired Power Plant. **Industrial & Engineering Chemistry Research**, v. 51, n. 21, p. 7355-7363, 2012.

LOCKWOOD, T. A Compararitive Review of Next-generation Carbon Capture Technologies for Coal-fired Power Plant. **Energy Procedia**, v. 114, p. 2658-2670, 2017.

LOWELL, S.*, et al.* **Characterization of porous solids and powders: Surface area, porosity and density (Particle technology series)**. The Netherlands: Springer, 2006.

MA'MUN, S.*, et al.* Selection of new absorbents for carbon dioxide capture. **Energy Conversion and Management**, v. 48, n. 1, p. 251-258, 2007.

MAJCHRZAK-KUCĘBA, I. and NOWAK, W. A thermogravimetric study of the adsorption of CO2 on zeolites synthesized from fly ash. **Thermochimica Acta**, v. 437, n. 1-2, p. 67-74, 2005.

MALEK, A. and FAROOQ, S. Comparison of isotherm models for hydrocarbon adsorption on activated carbon. **AIChE Journal**, v. 42, n. 11, p. 3191-3201, 1996.

MELO, C. R.*, et al.* Synthesis of 4A zeolites from kaolin for obtaining 5A zeolites through ionic exchange for adsorption of arsenic. **Materials Science and Engineering: B**, v. 177, n. 4, p. 345-349, 2012.

MODAK, A. and JANA, S. Advancement in porous adsorbents for post-combustion CO2 capture. **Microporous and Mesoporous Materials**, v. 276, p. 107-132, 2019.

MONDAL, M. K., BALSORA, H. K., and VARSHNEY, P. Progress and trends in CO2 capture/separation technologies: A review. **Energy**, v. 46, n. 1, p. 431-441, 2012.

MONDINO, G., GRANDE, C. A., and BLOM, R. Effect of Gas Recycling on the Performance of a Moving Bed Temperature-Swing (MBTSA) Process for CO2 Capture in a Coal Fired Power Plant Context. **Energies**, v. 10, n. 6, p. 745, 2017.

MONDINO, G.*, et al.* Moving bed temperature swing adsorption for CO2 capture from a natural gas combined cycle power plant. **International Journal of Greenhouse Gas Control**, v. 85, p. 58-70, 2019.

MONDINO, G.*, et al.* Initial operation of a continuous lab-scale MBTSA pilot using activated carbon adsorbent. in *15th International Conference on Greenhouse Gas Control Technologies, GHGT-15*. 2021. Abu Dhabi, UAE.

MONTANARI, T. and BUSCA, G. On the mechanism of adsorption and separation of CO2 on LTA zeolites: An IR investigation. **Vibrational Spectroscopy**, v. 46, n. 1, p. 45-51, 2008.

MORALES-OSPINO, R.*, et al.* Assessment of the potential use of zeolites synthesized from power plant fly ash to capture CO2 under post-combustion scenario. **Adsorption**, v. 26, n. 7, p. 1153-1164, 2020.

MORALES-OSPINO, R.*, et al.* Parametric Analysis of a Moving Bed Temperature Swing Adsorption (MBTSA) Process for Postcombustion CO2 Capture. **Industrial & Engineering Chemistry Research**, v. 60, n. 29, p. 10736-10752, 2021.

MURAYAMA, N., YAMAMOTO, H., and SHIBATA, J. Mechanism of zeolite synthesis from coal fly ash by alkali hydrothermal reaction. **International Journal of Mineral Processing**, v. 64, n. 1, p. 1-17, 2002.

MYERS, A. L. and PRAUSNITZ, J. M. Thermodynamics of Mixed-Gas Adsorption. **AIChE Journal**, v. 11, n. 1, p. 121-127, 1965.

NELSON, T. O.*, et al.* RTI's Solid Sorbent-Based CO2 Capture Process: Technical and Economic Lessons Learned for Application in Coal-fired, NGCC, and Cement Plants. **Energy Procedia**, v. 114, p. 2506-2524, 2017.

NIE, L.*, et al.* Recent developments and consideration issues in solid adsorbents for CO2 capture from flue gas*.* **Chinese Journal of Chemical Engineering**, v. 26, n. 11, p. 2303-2317, 2018.

NIKOLAIDIS, G. N., KIKKINIDES, E. S., and GEORGIADIS, M. C. A model-based approach for the evaluation of new zeolite 13X-based adsorbents for the efficient post-combustion CO 2 capture using P/VSA processes*.* **Chemical Engineering Research and Design**, v. 131, p. 362-374, 2018.

NTIAMOAH, A.*, et al.* CO2 Capture by Temperature Swing Adsorption: Use of Hot CO2-Rich Gas for Regeneration*.* **Industrial & Engineering Chemistry Research**, v. 55, n. 3, p. 703-713, 2016.

OKUMURA, T.*, et al.* CO2 Capture Test for A Moving-bed System Utilizi g Low-temperature Steam*.* **Energy Procedia**, v. 63, p. 2249-2254, 2014.

OKUMURA, T.*, et al.* Parametric Testing of a Pilot-scale Design for a Moving-bed CO 2 Capture System Using Low-temperature Steam*.* **Energy Procedia**, v. 114, p. 2322-2329, 2017.

OLAJIRE, A. A. CO2 capture and separation technologies for end-of-pipe applications – A review*.* **Energy**, v. 35, n. 6, p. 2610-2628, 2010.

PIRES, M. and QUEROL, X. Characterization of Candiota (South Brazil) coal and combustion by-product. *.* **Fuel and Energy Abstracts**, v. 46, n. 4, p. 210, 2005.

PLAZA, M. G.*, et al.* Adsorption-based Process Modelling for Post-combustion CO 2 Capture*.* **Energy Procedia**, v. 114, p. 2353-2361, 2017a.

PLAZA, M. G., RUBIERA, F., and PEVIDA, C. Evaluating the Feasibility of a TSA Process Based on Steam Stripping in Combination with Structured Carbon Adsorbents To Capture CO2from a Coal Power Plant*.* **Energy & Fuels**, v. 31, n. 9, p. 9760-9775, 2017b.

PRASAD, B. and MONDAL, K. K. R. Environmental impact of manganese due to its leaching from coal fly ash*.* **Journal of Environmental Science and Engineering**, v. 51, n. 1, p. 27-32, 2009.

QUEROL, X.*, et al.* Synthesis of zeolites from coal fly ash: an overview*.* **International Journal of Coal Geology**, v. 50, n. 1, p. 413-423, 2002.

REGE, S. U.*, et al.* Air-prepurification by pressure swing adsorption using single/layered beds*.* **Chemical Engineering Science**, v. 56, n. 8, p. 2745-2759, 2001.

RESTREPO, Á., BAZZO, E., and MIYAKE, R. A life cycle assessment of the Brazilian coal used for electric power generation*.* **Journal of Cleaner Production**, v. 92, p. 179-186, 2015.

ROUQUEROL, F.*, et al.* **Adsorption by Powders and Porous Solids**. London: Academic Pres, 2014.

ROUQUEROL, J., LLEWELLYN, P., and ROUQUEROL, F. Is the BET equation applicable to microporous adsorbents? **Characterization of Porous Solids Vii - Proceedings of the 7th International Symposium on the Characterization of Porous Solids (Cops-Vii), Aix-En-Provence, France, 26-28 May 2005**, v. 160, p. 49-56, 2006.

RUBIN, E. S. and RAO, A. B. **A Technical, Economic and Environmental Assessment of Amine-based CO2 Capture Technology for Power Plant Greenhouse Gas Control**. 2002. 18 p.

RUTHVEN, D. M. **Principles of Adsorption and Adsorption Processes**. New York: Wiley, 1984.

SAMANTA, A.*, et al.* Post-Combustion CO2 Capture Using Solid Sorbents: A Review*.* **Industrial & Engineering Chemistry Research**, v. 51, n. 4, p. 1438-1463, 2011.

SANCHEZ FERNANDEZ, E.*, et al.* Thermodynamic assessment of amine based CO2 capture technologies in power plants based on European Benchmarking Task Force methodology*.* **Fuel**, v. 129, p. 318-329, 2014.

SHEN, C.*, et al.* Two-Stage VPSA Process for CO2 Capture from Flue Gas Using Activated Carbon Beads*.* **Industrial & Engineering Chemistry Research**, v. 51, n. 13, p. 5011-5021, 2012.

SIDDIQUE, R. Performance characteristics of high-volume Class F fly ash concrete*.* **Cement and Concrete Research**, v. 34, n. 3, p. 487-493, 2004.

SILVA, F. A. and RODRIGUES, A. Vacuum Swing Adsorption for Propylene/Propane Separation with 4A Zeolite*.* **Ind. Eng. Chem. Res.**, v. 40, n. 24, p. 5758-5774, 2001.

SIPS, R. Combined form of Langmuir and Freundlich equations. **Chem. Phys.**, v. 16, p. 385-471, 1948.

SIRCAR, S. Basic Research Needs for Design of Adsorptive Gas Separation Processes. **Industrial & Engineering Chemistry Research**, v. 45, n. 16, p. 5435-5448, 2006.

SMITH, K. R.*, et al.* Energy and Human Health. **Annual Review of Public Health**, v. 34, n. 1, p. 159-188, 2013.

SOE, J. T.*, et al.* CO2Capture and Ca2+Exchange Using Zeolite A and 13X Prepared from Power Plant Fly Ash. **Bulletin of the Korean Chemical Society**, v. 37, n. 4, p. 490-493, 2016.

SON, Y., KIM, K., and LEE, K. S. Feasibility Study of a Moving-Bed Adsorption Process with Heat Integration for CO2 Capture through Energy Evaluation and Optimization. **Energy & Fuels**, v. 28, n. 12, p. 7599-7608, 2014.

SON, Y.*, et al.* An intermittently moving bed adsorption process for carbon dioxide capture. **International Journal of Greenhouse Gas Control**, v. 49, p. 34-46, 2016.

SONG, C. F., KITAMURA, Y., and LI, S. H. Evaluation of Stirling cooler system for cryogenic CO2 capture. **Applied Energy**, v. 98, p. 491-501, 2012.

SONGOLZADEH, M., RAVANCHI, M. T., and SOLEIMANI, M. Carbon Dioxide Capture and Storage: A general review on adsorbents. **International Journal of Chemical, Molecular, Nuclear, Materials and Metallurgical Engineering**, v. 6, n. 10, p. 900-907, 2012.

SONGOLZADEH, M.*, et al.* Carbon dioxide separation from flue gases: a technological review emphasizing reduction in greenhouse gas emissions. **ScientificWorldJournal**, v. 2014, p. 828131, 2014.

STORTI, G.*, et al.* Adsorption separation processes: Countercurrent and simulated countercurrent operations. **Computers & Chemical Engineering**, v. 12, n. 5, p. 475-482, 1988.

SUA-IAM, G. and MAKUL, N. Utilization of coal- and biomass-fired ash in the production of self-consolidating concrete: a literature review. **Journal of Cleaner Production**, v. 100, p. 59-76, 2015.

SUN, H., SHEN, B., and LIU, J. N-Paraffins adsorption with 5A zeolites: The effect of binder on adsorption equilibria. **Separation and Purification Technology**, v. 64, n. 1, p. 135-139, 2008.

TAUANOV, Z.*, et al.* Hydrothermal synthesis of zeolite production from coal fly ash: A heuristic approach and its optimization for system identification of conversion. **Journal of Cleaner Production**, v. 182, p. 616-623, 2018.

THIRUVENKATACHARI, R.*, et al.* Post combustion CO2 capture by carbon fibre monolithic adsorbents. **Progress in Energy and Combustion Science**, v. 35, n. 5, p. 438-455, 2009.

THOMMES, M.*, et al.* Physisorption of gases, with special reference to the evaluation of surface area and pore size distribution (IUPAC Technical Report). **Pure and Applied Chemistry**, v. 87, n. 9-10, p. 2015.

TLILI, N., GRÉVILLOT, G., and VALLIÈRES, C. Carbon dioxide capture and recovery by means of TSA and/or VSA. **International Journal of Greenhouse Gas Control**, v. 3, n. 5, p. 519-527, 2009.

TOTH, J. State Equations of Solid-Gas Interface Layers. **Acta Chimica Academiae Scientarium Hungaricae**, v. 69, n. 3, p. 311-&, 1971.

VOGTENHUBER, H.*, et al.* Process simulation of an efficient temperature swing adsorption concept for biogas upgrading. **Energy**, v. 162, p. 200-209, 2018.

WAKAO, N. and FUNAZKRI, T. Effect of fluid dispersion coefficients on particle-to-fluid mass transfer coefficients in packed beds Correlation of Sherwood numbers. **Chemical Engineering Science**, v. 33, p. 1375-1384, 1978.

WANG, L.*, et al.* CO2 capture from flue gas by two successive VPSA units using 13XAPG. **Adsorption**, v. 18, n. 5-6, p. 445-459, 2012.

WANG, L.*, et al.* CO2Capture from Flue Gas in an Existing Coal-Fired Power Plant by Two Successive Pilot-Scale VPSA Units. **Industrial & Engineering Chemistry Research**, v. 52, n. 23, p. 7947-7955, 2013.

WANG, Y. and LEVAN, M. D. Adsorption Equilibrium of Binary Mixtures of Carbon Dioxide and Water Vapor on Zeolites 5A and 13X. **Journal of Chemical & Engineering Data**, v. 55, n. 9, p. 3189-3195, 2010.

WARMUZINSKI, K., TANCZYK, M., and JASCHIK, M. Experimental study on the capture of CO2 from flue gas using adsorption combined with membrane separation. **International Journal of Greenhouse Gas Control**, v. 37, p. 182-190, 2015.

WEBLEY, P. A. and DANACI, D. **Chapter 5 CO2 Capture by Adsorption Processes, in Carbon Capture and Storage**. The Royal Society of Chemistry, 2020. 106-167.

WU, X.*, et al.* The Advances of Post-combustion CO2 Capture with Chemical Solvents: Review and Guidelines. **Energy Procedia**, v. 63, p. 1339-1346, 2014.

YANG, L.*, et al.* Green synthesis of zeolite 4A using fly ash fused with synergism of NaOH and Na2CO3. **Journal of Cleaner Production**, v. 212, p. 250-260, 2019.

ZAABOUT, A.*, et al.* Thermodynamic assessment of the swing adsorption reactor cluster (SARC) concept for post-combustion CO 2 capture. **International Journal of Greenhouse Gas Control**, v. 60, p. 74-92, 2017.

ZGUREVA, D. Carbon Dioxide Adsorption Studies on Fly Ash Zeolites. **Coal Combustion and Gasification Products**, v. 8, p. 54-59, 2016.

ZHANG, W.*, et al.* Process simulations of post-combustion CO 2 capture for coal and natural gas-fired power plants using a polyethyleneimine/silica adsorbent. **International Journal of Greenhouse Gas Control**, v. 58, p. 276-289, 2017a.

ZHANG, Z.*, et al.* Waste is a Misplayed Resource: Synthesis of Zeolites from Fly Ash for CO2 Capture. **Energy Procedia**, v. 114, p. 2537-2544, 2017b.

ZHAO, R.*, et al.* Comparative study on energy efficiency of moving-bed adsorption for carbon dioxide capture by two evaluation methods. **Sustainable Energy Technologies and Assessments**, v. 44, p. 101042, 2021.

APPENDIX A- X-RAY DIFFRACTION (XRD) RESULT OF THE FLY ASHES: JORGE LACERDA (LEFT) AND PECÉM (RIGHT) FLY ASH SAMPLES

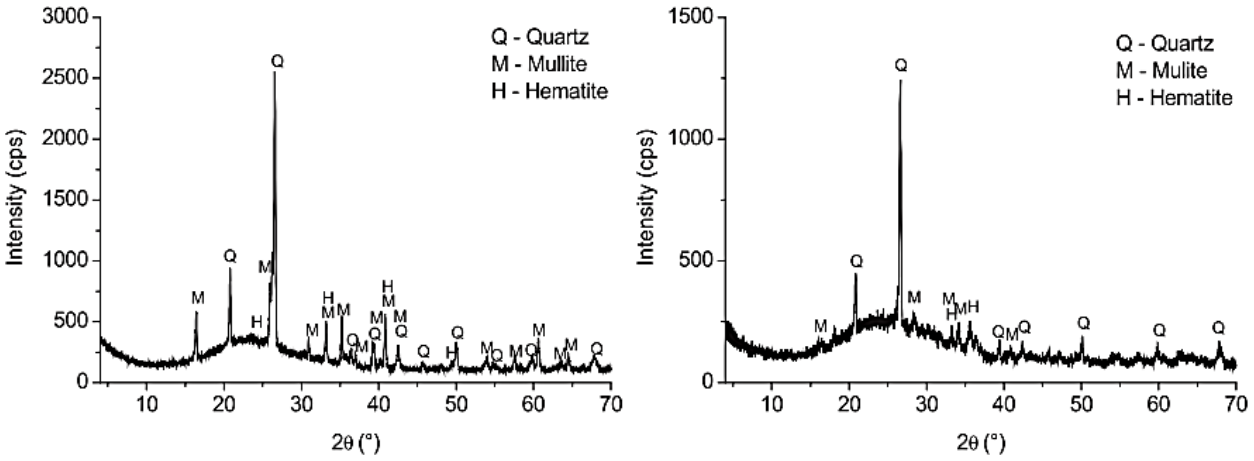

Source: Aquino et al. (2020)

APPENDIX B– MASS AND ENERGY BALANCE DERIVATION

- **Mass balance of component *i***

The mass balance in a moving bed is analogous to that of a fixed with the difference that the movement of the particle should be taken into consideration. The fluid phase mass balance was applied in an arbitrary control volume ($A\Delta z$) within the moving bed. In this case, the mass flux (F_m) per cross sectional area (A) of the recipient goes through a small bed length fraction (Δz). The mass balance was accomplished by differential formulation as follows:

$$Mass\ \mathrm{Flux_{in}} - \mathrm{Mass\ Flux_{out}} = \mathrm{Mass\ accumulation}$$

$$\varepsilon A F_m|_z - \varepsilon A F_m|_{z+\Delta z} = A \Delta z \frac{dC_i}{dt} \quad (1)$$

Dividing between $\varepsilon A \Delta z$ and applying limit function when $\Delta z \rightarrow 0$:

$$-\frac{\partial F_m}{\partial z} = \frac{1}{\varepsilon}\frac{dC_i}{dt} \quad (2)$$

C_i (mol m^{-3}) is total concentration of component *i* in system and ε is the bed voidage.

The total concentration (C_i) in the accumulation term of Eq.2 can be defined as follows:

$$C_i = \left[\varepsilon C_{g,i} + (1-\varepsilon)(\varepsilon_p C_{g,i} + \rho_p \bar{q}_i)\right] \quad (3)$$

Once the portion of the inlet flux gas, that accumulates in control volume, is distributed within the void fraction of the bed $\varepsilon C_{g,i}$, inside the particle porosity $(1-\varepsilon)\varepsilon_p C_{g,i}$ and on the material surface in adsorbed phase $(1-\varepsilon)\rho_p \bar{q}_i$. Being ρ_p the particle density in kg m^{-3} and $\bar{q}_i$ the average adsorbed of of component *i* in mol per kg of adsorbent.
Therefore, replacing Eq.3 in Eq. 2:

$$-\frac{\partial F_m}{\partial z} = \frac{\partial C_{g,i}}{\partial t} + \frac{(1-\varepsilon)}{\varepsilon}\varepsilon_p \frac{dC_{g,i}}{dt} + \frac{(1-\varepsilon)}{\varepsilon}\rho_p \frac{d\bar{q}_i}{dt} \quad (4)$$

Note that the accumulations terms that implicate the movement of the solid maintain the total derivative while the gas concentration accumulation in the void fraction of the bed is transformed into partial derivative. Now F_m can be divided into a convective flux contribution and a dispersive flux contribution respectively in the following way:

$$\mathrm{F_m} = v\mathrm{C_{g,i}} + \mathrm{F_{dispersive}} \tag{5}$$

here v represents intersticial gas velocity. The dispersive flux ($F_{dispersive}$) can be expressed in terms of axial mass dispersion ($D_{ax,i}$) analogous to Fick's First Law:

$$\mathrm{F_{dispersive}} = -\mathrm{D_{ax,i}}\frac{\partial \mathrm{C_{g,i}}}{\partial \mathrm{z}} \tag{6}$$

Substituting Eq.6 in Eq. 7 yields:

$$\mathrm{F_m} = -\left[\mathrm{D_{ax,i}}\frac{\partial \mathrm{C_{g,i}}}{\partial \mathrm{z}} - v\mathrm{C_{g,i}}\right] \tag{7}$$

Then applying partial derivation:

$$-\frac{\partial \mathrm{F_m}}{\partial \mathrm{z}} = \left[\mathrm{D_{ax,i}}\frac{\partial^2 \mathrm{C_{g,i}}}{\partial \mathrm{z}^2} - \frac{\partial}{\partial \mathrm{z}}(v\mathrm{C_{g,i}})\right] \tag{8}$$

Finally substituing Eq.8 in Eq.4, we obtain:

$$\mathrm{D_{ax,i}}\frac{\partial^2 \mathrm{C_{g,i}}}{\partial \mathrm{z}^2} - \frac{\partial}{\partial \mathrm{z}}(v\mathrm{C_{g,i}}) = \frac{\partial \mathrm{C_{g,i}}}{\partial \mathrm{t}} + \frac{(1-\varepsilon)}{\varepsilon}\varepsilon_\mathrm{p}\frac{\mathrm{dC_{g,i}}}{\mathrm{dt}} + \frac{(1-\varepsilon)}{\varepsilon}\rho_\mathrm{p}\frac{\mathrm{d}\overline{\mathrm{q_i}}}{\mathrm{dt}} \tag{9}$$

Rearranging and opening the terms of total derivative, we have:

$$\varepsilon D_{ax,i}\frac{\partial}{\partial z}\left(C_{g,T}\frac{\partial y_i}{\partial z}\right)-\frac{\partial}{\partial z}(uC_{g,i})-\varepsilon\frac{\partial C_{g,i}}{\partial t}-(1-\varepsilon)\varepsilon_p\left(\frac{\partial C_{g,i}}{\partial t}+u_s\frac{\partial C_{g,i}}{\partial z}\right)-(1-\varepsilon)\rho_p\left(\frac{\partial q_i}{\partial t}+u_s\frac{\partial q_i}{\partial z}\right)=0 \quad (10)$$

Here u is the superficial velocity, $u = v\varepsilon$

The overall mass balance is the sum of Eq. 10 for *n* components *i* in the gas mixture:

$$-\frac{\partial}{\partial z}\left(u_g C_{g,T}\right)=\varepsilon\frac{\partial C_{g,T}}{\partial t}+(1-\varepsilon)\rho_p\sum\left(\frac{\partial q_i}{\partial t}+u_s\frac{\partial q_i}{\partial z}\right)+(1-\varepsilon)\varepsilon_p\left(\frac{\partial C_{g,T}}{\partial t}+u_s\frac{\partial C_{g,T}}{\partial z}\right) \quad (11)$$

- **Overall energy balance**

Contributions in the energy balance:

Internal energy accumulation term in time, $\left(\frac{\partial U_x}{\partial t}\right)$*:* gas phase interparticle (g)+ solid (s) + adsorbed phase (a) + internal gas phase intraparticle (g) =

+Net flux of enthalpy in z direction, $-\left(\frac{\partial H_x}{\partial z}\right)$: gas phase interparticle + solid + adsorbed phase + adsorbed phase + gas phase intraparticle

-Energy exchange between the gas and the wall

+Dispersive energy flux

$$\varepsilon\frac{\partial}{\partial t}\left[C_{g,T}U_g\right]+(1-\varepsilon)\rho_p\frac{\partial U_s}{\partial t}+(1-\varepsilon)\rho_p\frac{\partial}{\partial t}\left[\sum\bar{q}_i U_{a,i}\right]+(1-\varepsilon)\varepsilon_p\frac{\partial}{\partial t}\left[C_{g,T}U_g\right]=-\frac{\partial}{\partial z}\left(u_g C_{g,T}H_g\right)-$$
$$(1-\varepsilon)\rho_p\frac{\partial}{\partial z}(u_s H_s)-(1-\varepsilon)\rho_p\frac{\partial}{\partial z}\left(u_s\sum\bar{q}_i H_{a,i}\right)-(1-\varepsilon)\varepsilon_p\frac{\partial}{\partial z}\left(u_s C_{g,T}H_g\right)-h_w A_v(T-T_w)+\frac{\partial}{\partial z}\left(\lambda\frac{\partial T}{\partial z}\right) \quad (12)$$

The first term in the right-hand side of the Eq. 12 (in red) can be open in the following way:

$$\frac{\partial}{\partial z}\left(u_g C_{g,T}H_g\right)=H_g\frac{\partial}{\partial z}\left(u_g C_{g,T}\right)+u_g C_{g,T}\frac{\partial}{\partial z}\left(H_g\right) \quad (13)$$

where the term in red corresponds to that in the left-hand side of the overall mass balance (Eq. 1). Substituting the overall mass balance (Eq. 11) in Eq 13. and subsequently Eq.13 in Eq. 12 gives Eq.14:

$$\boldsymbol{\varepsilon}\frac{\partial}{\partial t}\left[C_{g,T}U_g\right]+(1-\varepsilon)\rho_p\frac{\partial U_s}{\partial t}+(1-\varepsilon)\rho_p\frac{\partial}{\partial t}\left[\sum\bar{q}_i\,U_{a,i}\right]+(1-\varepsilon)\varepsilon_p\frac{\partial}{\partial t}\left[C_{g,T}U_g\right]=+H_g\left[\varepsilon\frac{\partial C_{g,T}}{\partial t}+(1-\varepsilon)\rho_p\sum\frac{d\bar{q}_i}{dt}+(1-\varepsilon)\varepsilon_p\left(\frac{\partial C_{g,T}}{\partial t}+u_s\frac{\partial C_{g,T}}{\partial z}\right)\right]-u_gC_{g,T}\frac{\partial}{\partial z}\left(H_g\right)-(1-\varepsilon)\rho_pu_s\frac{\partial}{\partial z}\left(H_s\right)-(1-\varepsilon)\rho_pu_s\frac{\partial}{\partial z}\left(\sum\bar{q}_i\,H_{a,i}\right)-(1-\varepsilon)\varepsilon_pu_s\frac{\partial}{\partial z}\left(C_{g,T}H_g\right)-h_wA_v(T-T_w)+\frac{\partial}{\partial z}\left(\lambda\frac{\partial T}{\partial z}\right) \quad (14)$$

Rearranging Eq.14:

$$\boldsymbol{\varepsilon}U_g\frac{\partial}{\partial t}\left[C_{g,T}\right]+\boldsymbol{\varepsilon}C_{g,T}\frac{\partial}{\partial t}\left[U_g\right]+(1-\varepsilon)\rho_p\frac{\partial U_s}{\partial t}+(1-\varepsilon)\rho_p\frac{\partial}{\partial t}\left[\sum\bar{q}_i\,U_{a,i}\right]+(1-\varepsilon)\varepsilon_p\frac{\partial}{\partial t}\left[C_{g,T}U_g\right]=+H_g\varepsilon\frac{\partial C_{g,T}}{\partial t}+H_g(1-\varepsilon)\rho_p\sum\frac{d\bar{q}_i}{dt}+(1-\varepsilon)\varepsilon_pH_g\left(\frac{\partial C_{g,T}}{\partial t}+u_s\frac{\partial C_{g,T}}{\partial z}\right)-u_gC_{g,T}\frac{\partial}{\partial z}\left(H_g\right)-(1-\varepsilon)\rho_pu_s\frac{\partial}{\partial z}\left(H_s\right)-(1-\varepsilon)\rho_pu_s\frac{\partial}{\partial z}\left(\sum\bar{q}_i\,H_{a,i}\right)-(1-\varepsilon)\varepsilon_pu_s\frac{\partial}{\partial z}\left(C_{g,T}H_g\right)-h_wA_v(T-T_w)+\frac{\partial}{\partial z}\left(\lambda\frac{\partial T}{\partial z}\right) \quad (15)$$

The terms in red in Eq. 15 can be summed in the following way:

$$(1-\varepsilon)\rho_p\left[H_g\sum\frac{d\bar{q}_i}{dt}-\frac{\partial}{\partial t}\left[\sum\bar{q}_i\,U_{a,i}\right]\right] \quad (16)$$

Assuming that $U_{a,i}=H_{a,i}$ and that the isosteric heat of adsorption may be expressed as $(-\Delta H_{ads,i})=H_{g,i}-H_{a,i}$, Eq. 16 can be rearranged as follows:

$$(1-\varepsilon)\rho_p\left[\sum\frac{d\bar{q}_i(-\Delta H_{ads,i})}{dt}+\sum\frac{d\bar{q}_iH_{a,i}}{dt}-\frac{\partial}{\partial t}\left(\sum\bar{q}_i\,H_{a,i}\right)\right] \quad (17)$$

By taking into account the particle movement in the z-axis, the total derivative can become:

$$\frac{d\bar{q}_i}{dt}=\frac{\partial\bar{q}_i}{\partial t}+u_s\frac{\partial\bar{q}_i}{\partial z}$$

Replacing the above term in Eq. 17:

$$(1-\varepsilon)\rho_p\left[\sum\frac{d\bar{q}_i(-\Delta H_{ads,i})}{dt}+\sum\frac{\partial\bar{q}_iH_{a,i}}{\partial t}+u_s\sum\frac{\partial\bar{q}_iH_{a,i}}{\partial z}-\frac{\partial}{\partial t}\left(\sum\bar{q}_i\,H_{a,i}\right)\right]$$

Cancelling the terms in red, give us:

$$(1-\varepsilon)\rho_p\left[\sum\frac{d\bar{q}_i(-\Delta H_{ads,i})}{dt}+u_s\sum\frac{\partial\bar{q}_iH_{a,i}}{\partial z}\right] \quad (18)$$

Assuming that $U_s = H_s$ *and* $H_g = (U_g + PV) = (U_g + RT)$. The Eq. 18 can be now incorporated in Eq. 15 to yield Eq.19.

$$\varepsilon U_g \frac{\partial}{\partial t}[C_{g,T}] + \varepsilon C_{g,T} \frac{\partial}{\partial t}[U_g] + (1-\varepsilon)\rho_p \frac{\partial H_s}{\partial t} + (1-\varepsilon)\varepsilon_p \frac{\partial}{\partial t}[C_{g,T} U_g] = (U_g + RT)\varepsilon \frac{\partial C_{g,T}}{\partial t} + (1-\varepsilon)\rho_p \left[\sum \frac{d\bar{q}_i(-\Delta H_{ads,i})}{dt} + u_s \sum \frac{\partial \bar{q}_i H_{a,i}}{\partial z}\right] + (1-\varepsilon)\varepsilon_p H_g \left(\frac{\partial C_{g,T}}{\partial t} + u_s \frac{\partial C_{g,T}}{\partial z}\right) - u_g C_{g,T} \frac{\partial}{\partial z}(H_g) - (1-\varepsilon)\rho_p u_s \frac{\partial}{\partial z}(H_s) - (1-\varepsilon)\rho_p u_s \frac{\partial}{\partial z}\left(\sum \bar{q}_i H_{a,i}\right) - (1-\varepsilon)\varepsilon_p u_s \frac{\partial}{\partial z}(C_{g,T} H_g) - h_w A_v (T - T_w) + \frac{\partial}{\partial z}\left(\lambda \frac{\partial T}{\partial z}\right) \quad (19)$$

The sum of the terms in red and blue respectively equals zero. Thus, rearranging Eq. 19 yields:

$$\varepsilon C_{g,T} \frac{\partial}{\partial t}[U_g] + (1-\varepsilon)\rho_p \frac{\partial H_s}{\partial t} + (1-\varepsilon)\varepsilon_p \frac{\partial}{\partial t}[C_{g,T} U_g] = RT\varepsilon \frac{\partial C_{g,T}}{\partial t} + (1-\varepsilon)\rho_p \sum \frac{d\bar{q}_i(-\Delta H_{ads,i})}{dt} + (1-\varepsilon)\varepsilon_p H_g \left(\frac{\partial C_{g,T}}{\partial t} + u_s \frac{\partial C_{g,T}}{\partial z}\right) - u_g C_{g,T} \frac{\partial}{\partial z}(H_g) - (1-\varepsilon)\rho_p u_s \frac{\partial}{\partial z}(H_s) - (1-\varepsilon)\rho_p u_s \frac{\partial}{\partial z}(C_{g,T} H_g) - h_w A_v (T - T_w) + \frac{\partial}{\partial z}\left(\lambda \frac{\partial T}{\partial z}\right) \quad (20)$$

The terms in red in Eq. 20 can be open in the following way:

$$\varepsilon C_{g,T} \frac{\partial}{\partial t}[U_g] + (1-\varepsilon)\rho_p \frac{\partial H_s}{\partial t} + (1-\varepsilon)\varepsilon_p C_{g,T} \frac{\partial}{\partial t}[U_g] + (1-\varepsilon)\varepsilon_p U_g \frac{\partial}{\partial t}[C_{g,T}] = RT\varepsilon \frac{\partial C_{g,T}}{\partial t} + (1-\varepsilon)\rho_p \sum \frac{d\bar{q}_i(-\Delta H_{ads,i})}{dt} + (1-\varepsilon)\varepsilon_p H_g \left(\frac{\partial C_{g,T}}{\partial t} + u_s \frac{\partial C_{g,T}}{\partial z}\right) - u_g C_{g,T} \frac{\partial}{\partial z}(H_g) - (1-\varepsilon)\rho_p u_s \frac{\partial}{\partial z}(H_s) - (1-\varepsilon)\rho_p u_s C_{g,T} \frac{\partial}{\partial z}(H_g) - (1-\varepsilon)\rho_p u_s H_g \frac{\partial}{\partial z}(C_{g,T}) - h_w A_v (T_g - T_w) + \frac{\partial}{\partial z}\left(\lambda \frac{\partial T}{\partial z}\right) \quad (21)$$

The term U_g in red in Eq. 46 can be transformed into $U_g = H_g - RT$:

$$\varepsilon C_{g,T} \frac{\partial}{\partial t}[U_g] + (1-\varepsilon)\rho_p \frac{\partial H_s}{\partial t} + (1-\varepsilon)\varepsilon_p C_{g,T} \frac{\partial}{\partial t}[U_g] + (1-\varepsilon)\varepsilon_p H_g \frac{\partial}{\partial t}[C_{g,T}] - (1-\varepsilon)\varepsilon_p RT \frac{\partial}{\partial t}[C_{g,T}] = RT\varepsilon \frac{\partial C_{g,T}}{\partial t} + (1-\varepsilon)\rho_p \sum \frac{d\bar{q}_i(-\Delta H_{ads,i})}{dt} + (1-\varepsilon)\varepsilon_p H_g \frac{\partial C_{g,T}}{\partial t} + (1-\varepsilon)\varepsilon_p u_s H_g \frac{\partial C_{g,T}}{\partial z} - u_g C_{g,T} \frac{\partial}{\partial z}(H_g) - (1-\varepsilon)\rho_p u_s \frac{\partial}{\partial z}(H_s) - (1-\varepsilon)\rho_p u_s C_{g,T} \frac{\partial}{\partial z}(H_g) - (1-\varepsilon)\rho_p u_s H_g \frac{\partial}{\partial z}(C_{g,T}) - h_w A_v (T - T_w) + \frac{\partial}{\partial z}\left(\lambda \frac{\partial T}{\partial z}\right) \quad (22)$$

The sum of the terms in red and blue respectively equals zero. Thus, rearranging Eq. 23 yields:

$$\boldsymbol{\varepsilon}\mathrm{C_{g,T}}\frac{\partial}{\partial \mathrm{t}}\left[\mathrm{U_g}\right]+(1-\varepsilon)\rho_{\mathrm{p}}\frac{\partial \mathrm{H_s}}{\partial \mathrm{t}}+(1-\varepsilon)\varepsilon_{\mathrm{p}}\mathrm{C_{g,T}}\frac{\partial}{\partial \mathrm{t}}\left[\mathrm{U_g}\right]-(1-\varepsilon)\varepsilon_{\mathrm{p}}\mathrm{RT}\frac{\partial}{\partial \mathrm{t}}\left[\mathrm{C_{g,T}}\right]=\mathrm{RT}\varepsilon\frac{\partial C_{g,T}}{\partial t}+(1-\varepsilon)\rho_p\sum\frac{d\bar{q}_i(-\Delta H_{ads,i})}{dt}+-\mathrm{u_g}\mathrm{C_{g,T}}\frac{\partial}{\partial \mathrm{z}}\left(\mathrm{H_g}\right)-(1-\varepsilon)\rho_{\mathrm{p}}\mathrm{u_s}\frac{\partial}{\partial \mathrm{z}}\left(\mathrm{H_s}\right)-(1-\varepsilon)\rho_{\mathrm{p}}\mathrm{u_s}\mathrm{C_{g,T}}\frac{\partial}{\partial \mathrm{z}}\left(\mathrm{H_g}\right)-\mathrm{h_w}\mathrm{A_v}(T-\mathrm{T_w})+\frac{\partial}{\partial \mathrm{z}}\left(\lambda\frac{\partial \mathrm{T}}{\partial \mathrm{z}}\right) \tag{23}$$

Assuming $\mathrm{U_g}=C_{v,g}T$; $H_g=C_{p,g}T$; $H_s=C_{p,s}T$ and thermal equilibrium between the solid and phase so that T=T_s=T_g, Eq. 23 can be rewritten as:

$$\boldsymbol{\varepsilon}C_{v,g}\mathrm{C_{g,T}}\frac{\partial \mathrm{T}}{\partial \mathrm{t}}+(1-\varepsilon)\rho_{\mathrm{p}}C_{p,s}\frac{\partial \mathrm{T}}{\partial \mathrm{t}}+(1-\varepsilon)\varepsilon_{\mathrm{p}}C_{v,g}\mathrm{C_{g,T}}\frac{\partial \mathrm{T}}{\partial \mathrm{t}}-(1-\varepsilon)\varepsilon_{\mathrm{p}}\mathrm{RT}\frac{\partial \mathrm{C_{g,T}}}{\partial \mathrm{t}}=\varepsilon\mathrm{RT}\frac{\partial C_{g,T}}{\partial t}+(1-\varepsilon)\rho_p\sum\frac{d\bar{q}_i(-\Delta H_{ads,i})}{dt}+-\mathrm{u_g}C_{p,g}\mathrm{C_{g,T}}\frac{\partial \mathrm{T}}{\partial \mathrm{z}}-(1-\varepsilon)\rho_{\mathrm{p}}C_{p,s}\mathrm{u_s}\frac{\partial \mathrm{T}}{\partial \mathrm{z}}-(1-\varepsilon)\rho_{\mathrm{p}}\mathrm{u_s}C_{p,g}\mathrm{C_{g,T}}\frac{\partial \mathrm{T}}{\partial \mathrm{z}}-\mathrm{h_w}\mathrm{A_v}(\mathrm{T}-\mathrm{T_w})+\frac{\partial}{\partial \mathrm{z}}\left(\lambda\frac{\partial \mathrm{T}}{\partial \mathrm{z}}\right) \tag{24}$$

Summing the terms of equal colors of Eq. 24 and rearranging, we obtain the overall energy balance below:

$$\frac{\partial}{\partial z}\left(\boldsymbol{\lambda}\frac{\partial \boldsymbol{T}}{\partial z}\right)-\boldsymbol{u_g}\boldsymbol{C_{g,T}}\boldsymbol{C_{pg}}\frac{\partial \boldsymbol{T}}{\partial z}+\left[\boldsymbol{\varepsilon}+(\mathbf{1}-\boldsymbol{\varepsilon})\boldsymbol{\varepsilon_p}\right]\boldsymbol{R_g}\boldsymbol{T}\frac{\partial \boldsymbol{C_{g,T}}}{\partial \boldsymbol{t}}-\boldsymbol{A_v}(\boldsymbol{h_w})(\boldsymbol{T}-\boldsymbol{T_w})+(\mathbf{1}-\boldsymbol{\varepsilon})\boldsymbol{\rho_p}\sum_{i=1}^{n}(-\Delta\boldsymbol{H_{ads,i}})\frac{d\bar{q}_i}{dt}-\boldsymbol{\varepsilon}\boldsymbol{C_{vg}}\boldsymbol{C_{g,T}}\frac{\partial \boldsymbol{T}}{\partial \boldsymbol{t}}-(\mathbf{1}-\boldsymbol{\varepsilon})\boldsymbol{\rho_p}\boldsymbol{C_{ps}}\left[\frac{\partial \boldsymbol{T}}{\partial \boldsymbol{t}}+\boldsymbol{u_s}\frac{\partial \boldsymbol{T}}{\partial z}\right]-(\mathbf{1}-\boldsymbol{\varepsilon})\boldsymbol{\varepsilon_p}\boldsymbol{C_{g,T}}\left[\frac{\boldsymbol{C_{vg}}\partial \boldsymbol{T}}{\partial \boldsymbol{t}}+\boldsymbol{u_s}\frac{\boldsymbol{C_{pg}}\partial \boldsymbol{T}}{\partial z}\right]=\mathbf{0} \tag{25}$$

APPENDIX C – DIMENSIONLESS EQUATION DERIVATION.

1. Mass balance

Original component mass balance equation:

$$\boldsymbol{\varepsilon D_{ax,i}\,\frac{\partial}{\partial z}\left(C_{g,T}\frac{\partial y_i}{\partial z}\right)-\frac{\partial}{\partial z}\left(uC_{g,i}\right)-\varepsilon\frac{\partial C_{g,i}}{\partial t}-(1-\varepsilon)\varepsilon_p\left(\frac{\partial C_{g,i}}{\partial t}+u_s\frac{\partial C_{g,i}}{\partial z}\right)-(1-\varepsilon)\rho_p\frac{d\bar{q}_i}{dt}=0}$$

If $z^* = \frac{z}{L}$; $C_{g,T}{}^* = \frac{C_{g,T}}{C_{g,To}}$; $u^* = \frac{u}{u_o}$; $C_{g,i}{}^* = \frac{C_{g,i}}{C_{g,io}}$; $t^* = t\,K_{LDF,i}$; $\bar{q}_i{}^* = \frac{\bar{q}_i}{q_{m,i}}$

$$\frac{\varepsilon D_{ax,i}C_{g,To}}{L^2}\,\frac{\partial}{\partial z^*}\left(C_{g,T}{}^*\frac{\partial y_i}{\partial z^*}\right)-\frac{u_o C_{g,io}}{L}\frac{\partial}{\partial z^*}\left(u^* C_{g,i}{}^*\right)-\varepsilon C_{g,io}K_{LDF,i}\frac{\partial C_{g,i}{}^*}{\partial t^*}$$
$$-(1-\varepsilon)\varepsilon_p C_{g,io}\left(K_{LDF,i}\frac{\partial C_{g,i}{}^*}{\partial t^*}+u_s\frac{1}{L}\frac{\partial C_{g,i}{}^*}{\partial z^*}\right)-K_{LDF,i}(1-\varepsilon)\rho_p q_{m,i}\frac{d\bar{q}_i{}^*}{dt^*}=0$$

Dividing all the equation by $\frac{D_{ax,i}C_{g,To}}{L^2}$ and $y_{io} = \frac{C_{g,io}}{C_{g,To}}$

$$\varepsilon\frac{\partial}{\partial z^*}\left(C_{g,T}{}^*\frac{\partial y_i}{\partial z^*}\right)-\frac{u_o L}{D_{ax,i}}y_{io}\frac{\partial}{\partial z^*}\left(u^* C_{g,i}{}^*\right)-\frac{L^2K_{LDF,i}}{D_{ax,i}}y_{io}\frac{\partial C_{g,i}{}^*}{\partial t^*}$$
$$-(1-\varepsilon)\varepsilon_p y_{io}\frac{L^2}{D_{ax,i}}\left(K_{LDF,i}\frac{\partial C_{g,i}{}^*}{\partial t^*}+u_s\frac{1}{L}\frac{\partial C_{g,i}{}^*}{\partial z^*}\right)-(1-\varepsilon)\frac{L^2K_{LDF,i}}{D_{ax,i}}\frac{\rho_p q_{m,i}}{C_{g,To}}\frac{d\bar{q}_i{}^*}{dt^*}=0$$

If $\alpha_1 = \frac{u_o L}{D_{ax,i}}$; $\alpha_2 = \frac{L^2K_{LDF,i}}{D_{ax,i}}$; $\alpha_3 = \frac{u_s L}{D_{ax,i}}$; $\alpha_4 = \frac{\rho_p q_{m,i}}{C_{g,To}}$, we obtain:

***Dimensionless component mass balance equation*:**

$$\boldsymbol{\varepsilon\frac{\partial}{\partial z^*}\left(C_{g,T}{}^*\frac{\partial y_i}{\partial z^*}\right)-\alpha_1 y_{io}\frac{\partial}{\partial z^*}\left(u^* C_{g,i}{}^*\right)-\alpha_2 y_{io}\frac{\partial C_{g,i}{}^*}{\partial t^*}}$$
$$\boldsymbol{-(1-\varepsilon)\varepsilon_p y_{io}\left(\alpha_2\frac{\partial C_{g,i}{}^*}{\partial t^*}+\alpha_3\frac{\partial C_{g,i}{}^*}{\partial z^*}\right)-(1-\varepsilon)\alpha_2\alpha_4\frac{d\bar{q}_i{}^*}{dt^*}=0}$$

The total mass balance is obtained by summing the preceding equation for all the components of the mixture:

$$\boldsymbol{\alpha_5 \frac{\partial}{\partial z^*}\left(u^* C_{g,T}{}^*\right) + \alpha_6 \frac{\partial C_{g,T}{}^*}{\partial t^*} + (1-\varepsilon)\varepsilon_p\left(\alpha_6 \frac{\partial C_{g,T}{}^*}{\partial t^*} + \alpha_7 \frac{\partial C_{g,T}{}^*}{\partial z^*}\right) + (1-\varepsilon)\alpha_6\alpha_8 \sum_{i=1}^{NoC} \frac{d\bar{q}_i{}^*}{dt^*} = 0}$$

Where $\alpha_5 = u_o L$; $\alpha_6 = L^2 K_{LDF,i}$; $\alpha_7 = u_s L$; $\alpha_8 = \frac{\rho_p \sum q_{m,i}}{C_{g,To}}$

2. Linear driving force:

Original adsorbed phase mass balance:

$$\boldsymbol{\frac{d\bar{q}_i}{dt} = \frac{\partial \bar{q}_i}{\partial t} + u_s \frac{\partial \bar{q}_i}{\partial z} = K_{LDF,i}(q_{ei} - \bar{q}_i)}$$

If $z^* = \frac{z}{L}$; $t^* = t\, K_{LDF,i}$; $\bar{q}_i{}^* = \frac{\bar{q}_i}{q_{m,i}}$; $q_{ei}^* = \frac{q_{ei}}{q_{m,i}}$, then

$$q_{mi} K_{LDF,i} \frac{d\bar{q}_i{}^*}{dt^*} = q_{mi} K_{LDF,i} \frac{\partial \bar{q}_i{}^*}{\partial t^*} + u_s \frac{q_{mi}}{L} \frac{\partial \bar{q}_i{}^*}{\partial z^*} = K_{LDF,i} q_{mi} (q_{ei}^* - \bar{q}_i{}^*)$$

If we divide the preceding equation by $q_{mi} K_{LDF,i}$

$$\frac{d\bar{q}_i{}^*}{dt^*} = \frac{\partial \bar{q}_i{}^*}{\partial t^*} + \frac{u_s}{L K_{LDF,i}} \frac{\partial \bar{q}_i{}^*}{\partial z^*} = (q_{ei}^* - \bar{q}_i{}^*)$$

If $\theta = \frac{u_s}{K_{LDF,i} L}$, we obtain:

Dimensionless adsorbed phase mass balance:

$$\boldsymbol{\frac{d\bar{q}_i{}^*}{dt^*} = \frac{\partial \bar{q}_i{}^*}{\partial t^*} + \theta \frac{\partial \bar{q}_i{}^*}{\partial z^*} = K_{LDF,i}{}^* (q_{ei}^* - \bar{q}_i{}^*)}$$

3. Energy Balance

Original energy balance equation:

$$\boldsymbol{\frac{\partial}{\partial z}\left(\lambda \frac{\partial T}{\partial z}\right) - u C_{g,T} C_{pg} \frac{\partial T}{\partial z} + \left[\varepsilon + (1-\varepsilon)\varepsilon_p\right] R_g T \frac{\partial C_{g,T}}{\partial t} - A_v(h_w)(T - T_w)}$$
$$\boldsymbol{+ (1-\varepsilon)\rho_p \sum_{i=1}^{n} \left(-\Delta H_{ads,i}\right) \frac{d\bar{q}_i}{dt} - \varepsilon C_{vg} C_{g,T} \frac{\partial T}{\partial t} - (1-\varepsilon)\rho_p C_{ps} \left[\frac{\partial T}{\partial t} + u_s \frac{\partial T}{\partial z}\right]}$$
$$\boldsymbol{- (1-\varepsilon)\varepsilon_p C_{g,T} \left[\frac{C_{vg} \partial T}{\partial t} + u_s \frac{C_{pg} \partial T}{\partial z}\right] = 0}$$

If $z^* = \frac{z}{L}$; $C_{g,T}{}^* = \frac{C_{g,T}}{C_{g,T0}}$; $u^* = \frac{u}{u_o}$; $C_{g,i}{}^* = \frac{C_{g,i}}{C_{g,io}}$; $t^* = t\,K_{LDF,1}$; $\bar{q}_i{}^* = \frac{\bar{q}_i}{q_{m,i}}$; $T^* = \frac{T}{T_0}$; $T_w^* = \frac{T_w}{T_0}$; $h_w{}^* = \frac{h_w}{h_{w_0}}$ $\lambda = \frac{\lambda}{\lambda_0}$ where h_{w_0} and λ_0 are function of $u_0, \rho_0(T_0, P_0)$

$$\frac{T_0\lambda_0}{L^2}\frac{\partial}{\partial z^*}\left(\lambda\frac{\partial T^*}{\partial z^*}\right) - \frac{u_0 C_{g,T0} C_{pg}\, T_0}{L}\, u^* C_{g,T}{}^* \frac{\partial T^*}{\partial z^*} + \left[\varepsilon + (1-\varepsilon)\varepsilon_p\right] R_g T_0 C_{g,T0}\, K_{LDF,1} T^* \frac{\partial C_{g,T}{}^*}{\partial t^*}$$
$$- A_v(h_{w_0}) T_0 h_w{}^* (T^* - T_w{}^*)$$
$$+ (1-\varepsilon)\rho_p \sum_{i=1}^{n} (-\Delta H_{ads,i}) K_{LDF,1}\, q_{mi} \frac{d\bar{q}_i{}^*}{dt^*} - \varepsilon C_{vg} C_{g,T0} T_0\, K_{LDF,1}\, C_{g,T}{}^* \frac{\partial T^*}{\partial t^*}$$
$$- (1-\varepsilon)\rho_p C_{ps} \left[K_{LDF,1} T_0 \frac{\partial T^*}{\partial t^*} + u_s \frac{T_0}{L}\frac{\partial T^*}{\partial z^*}\right]$$
$$- (1-\varepsilon)\varepsilon_p C_{g,T}{}^* C_{g,T0} \left[C_{vg} K_{LDF,1} T_0 \frac{\partial T^*}{\partial t^*} + C_{pg} u_s \frac{T_0}{L}\frac{\partial T^*}{\partial z^*}\right] = 0$$

Dividing all the equation by $\frac{T_0\lambda_0}{L^2}$ and adding the unity term $\frac{\boldsymbol{C_{pg}}}{\boldsymbol{C_{pg}}}$ in some cases for mathematical rearrangement:

$$\frac{\partial}{\partial z^*}\left(\lambda\frac{\partial T^*}{\partial z^*}\right) - \frac{u_0 C_{g,T0} C_{pg}\, L}{\lambda_0}\, u^* C_{g,T}{}^* \frac{\partial T^*}{\partial z^*} + \left[\varepsilon + (1-\varepsilon)\varepsilon_p\right] \frac{R_g C_{g,T0} L^2 K_{LDF,i}}{\lambda_0} \frac{\boldsymbol{C_{pg}}}{\boldsymbol{C_{pg}}} T^* \frac{\partial C_{g,T}{}^*}{\partial t^*}$$
$$- \frac{A_v(h_{w_0}) L^2}{\lambda_0} h_w{}^* (T^* - T_w{}^*)$$
$$+ (1-\varepsilon)\rho_p \sum_{i=1}^{n} (-\Delta H_{ads,i}) \frac{q_{mi} L^2 K_{LDF,i}}{\lambda_0 T_0} \frac{d\bar{q}_i{}^*}{dt^*} - \varepsilon \frac{C_{vg} C_{g,T0} L^2 K_{LDF,i}}{\lambda_0} \frac{\boldsymbol{C_{pg}}}{\boldsymbol{C_{pg}}} C_{g,T}{}^* \frac{\partial T^*}{\partial t^*}$$
$$- (1-\varepsilon) \frac{\rho_p C_{ps} L^2}{\lambda_0} \left[K_{LDF,i} \frac{\partial T^*}{\partial t^*} + \frac{u_s}{L}\frac{\partial T^*}{\partial z^*}\right]$$
$$- (1-\varepsilon)\varepsilon_p C_{g,T}{}^* \frac{C_{g,T0} L^2}{\lambda_0} \frac{\boldsymbol{C_{pg}}}{\boldsymbol{C_{pg}}} \left[C_{vg} K_{LDF,i} \frac{\partial T^*}{\partial t^*} + C_{pg} \frac{u_s}{L}\frac{\partial T^*}{\partial z^*}\right] = 0$$

If $\gamma = \frac{C_{pg}}{C_{vg}}; (C_{pg} - C_{vg}) = R_g; \beta_1 = \frac{u_0 C_{g,T0} C_{pg}\, L}{\lambda_0}$; $\beta_2 = \frac{\lambda_0}{C_{pg} C_{g,T0} L^2 K_{LDF,1}}$; $\beta_3 = \frac{A_v(h_{w_0}) L^2}{\lambda_0}$; $\beta_4 = \rho_p \sum_{i=1}^{n} (-\Delta H_{ads,i}) \frac{q_{mi} L^2 K_{LDF,1}}{\lambda_0 T_0}$; $\beta_5 = \frac{\rho_p C_{ps} L^2 K_{LDF,1}}{\lambda_0}$; $\beta_6 = \frac{u_s \rho_p C_{ps} L}{\lambda_0}$; $\beta_7 = \frac{u_s C_{g,T0} C_{pg}\, L}{\lambda_0}$, we obtain:

Dimensionless energy balance equation:

$$\frac{\partial}{\partial z^*}\left(\lambda\frac{\partial T^*}{\partial z^*}\right) - \beta_1 u^* {C_{g,T}}^* \frac{\partial T^*}{\partial z^*} + \left[\varepsilon + (1-\varepsilon)\varepsilon_p\right]\frac{(\gamma-1)}{\gamma\beta_2} T^* \frac{\partial {C_{g,T}}^*}{\partial t^*} - \beta_3 {h_w}^* (T^* - {T_w}^*) + (1-\varepsilon)\beta_4 \frac{d\bar{q}_i^*}{dt^*} - \frac{\varepsilon}{\gamma\beta_2} {C_{g,T}}^* \frac{\partial T^*}{\partial t^*} - (1-\varepsilon)\left[\beta_5 \frac{\partial T^*}{\partial t^*} + \beta_6 \frac{\partial T^*}{\partial z^*}\right] - (1-\varepsilon)\varepsilon_p {C_{g,T}}^* \left[\frac{1}{\gamma\beta_2}\frac{\partial T^*}{\partial t^*} - \beta_7 \frac{\partial T^*}{\partial z^*}\right] = 0$$

4. Energy wall balance

Original energy wall balance equation:

$$\rho_w C_{pw} \frac{\partial T_w}{\partial t} = \left({}^1/_{e_w}\right) h_w (T - T_w) - \left({}^1/_{e_w}\right) U_g (T_w - T_{inf})$$

If $T^* = \frac{T}{T_0}$; $t^* = t\,K_{LDF,1}$; $T_w^* = \frac{T_w}{T_0}$; ${h_w}^* = \frac{h_w}{h_{w_0}}$; $U_g^* = \frac{U_g}{U_o}$ where $U_0 = f(h_{w0})$

$$\rho_w C_{pw} T_0 K_{LDF,1} \frac{\partial {T_w}^*}{\partial t^*} = \left({}^1/_{e_w}\right) h_{w_0} T_0 h_w^* (T^* - {T_w}^*) - \left({}^1/_{e_w}\right) U_o T_0 U^* ({T_w}^* - {T_{inf}}^*)$$

Dividing all the equation by $\rho_w C_{pw} T_0 K_{LDF,1}$

$$\frac{\partial {T_w}^*}{\partial t^*} = \frac{\left({}^1/_{e_w}\right) h_{w0} h_w^*}{\rho_w C_{pw} K_{LDF,1}} (T^* - {T_w}^*) - \frac{\left({}^1/_{e_w}\right) U_o}{\rho_w C_{pw} K_{LDF,1}} U^* ({T_w}^* - {T_{inf}}^*)$$

If $\emptyset_1 = \frac{\left({}^1/_{e_w}\right) h_{w_0}}{\rho_w C_{pw} K_{LDF,1}}$; $\emptyset_2 = \frac{\left({}^1/_{e_w}\right) U_o}{\rho_w C_{pw} K_{LDF,1}}$, we obtain:

Dimensionless energy wall balance equation:

$$\frac{\partial {T_w}^*}{\partial t^*} = \emptyset_1 h_w^* (T^* - {T_w}^*) - \emptyset_2 U^* \left({T_w}^* - {T_{inf}}^*\right)$$

5. Momentum Balance

Original pressure drop equation:

$$-\frac{\partial P}{\partial z} = K_D \times u$$

If $z^* = \frac{z}{L}$; $P^* = \frac{P}{P_0}$; $u^* = \frac{u}{u_o}$

$$-\frac{P_0}{L}\frac{\partial P^*}{\partial z^*} = K_D \times u_0 u^*$$

If $\delta = \frac{K_D u_0 L}{P_0}$, we obtain:

Dimensionless pressure drop equation

$$-\frac{\partial P^*}{\partial z^*} = \delta u^*$$

APPENDIX D – BINARY ADSORPTION ISOTHERMS OF CO_2 (15% vol.) AND N_2 (85% vol.)

SAMPLE ZEO13X

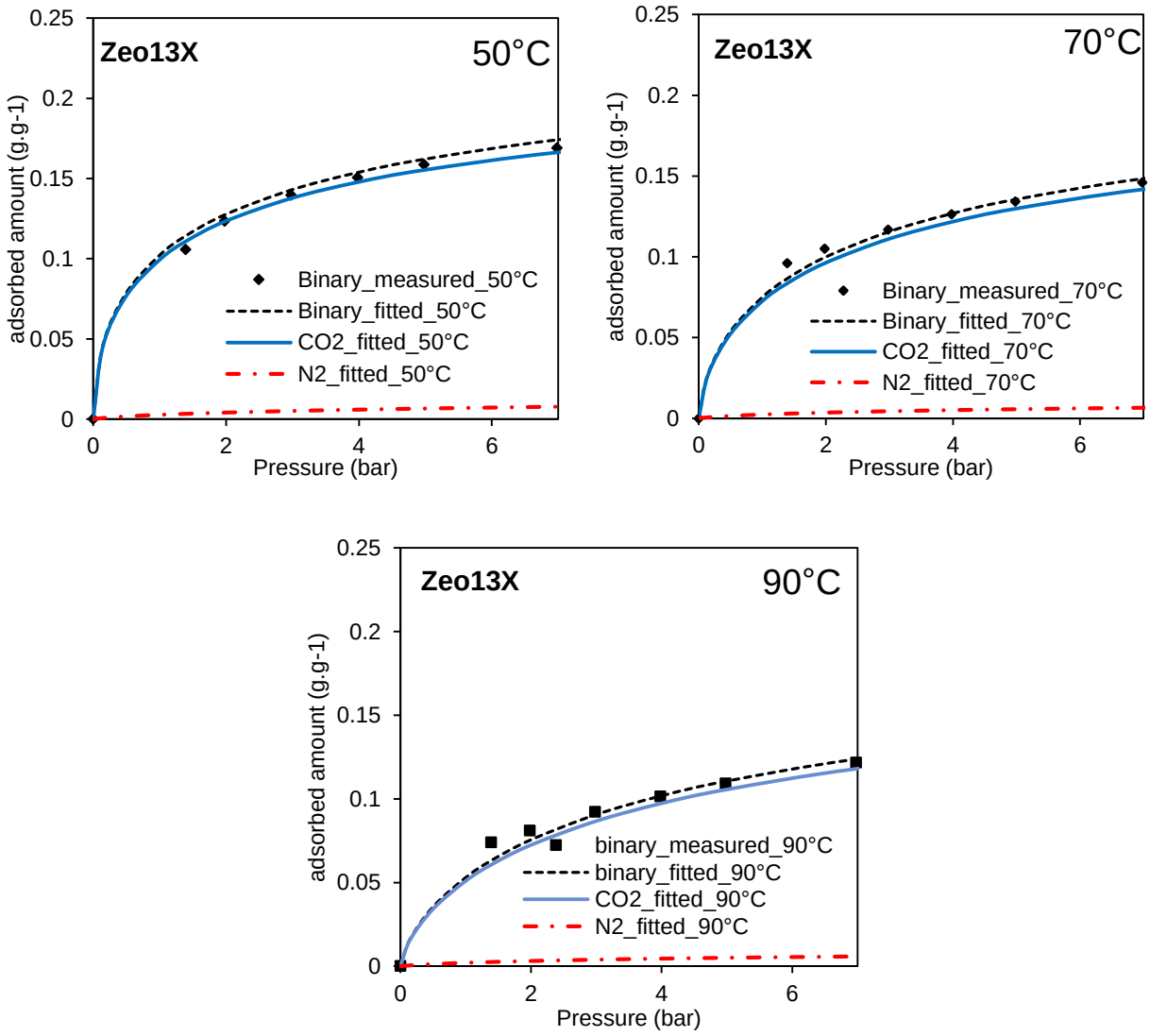

Source: own authorship

SAMPLE XFF

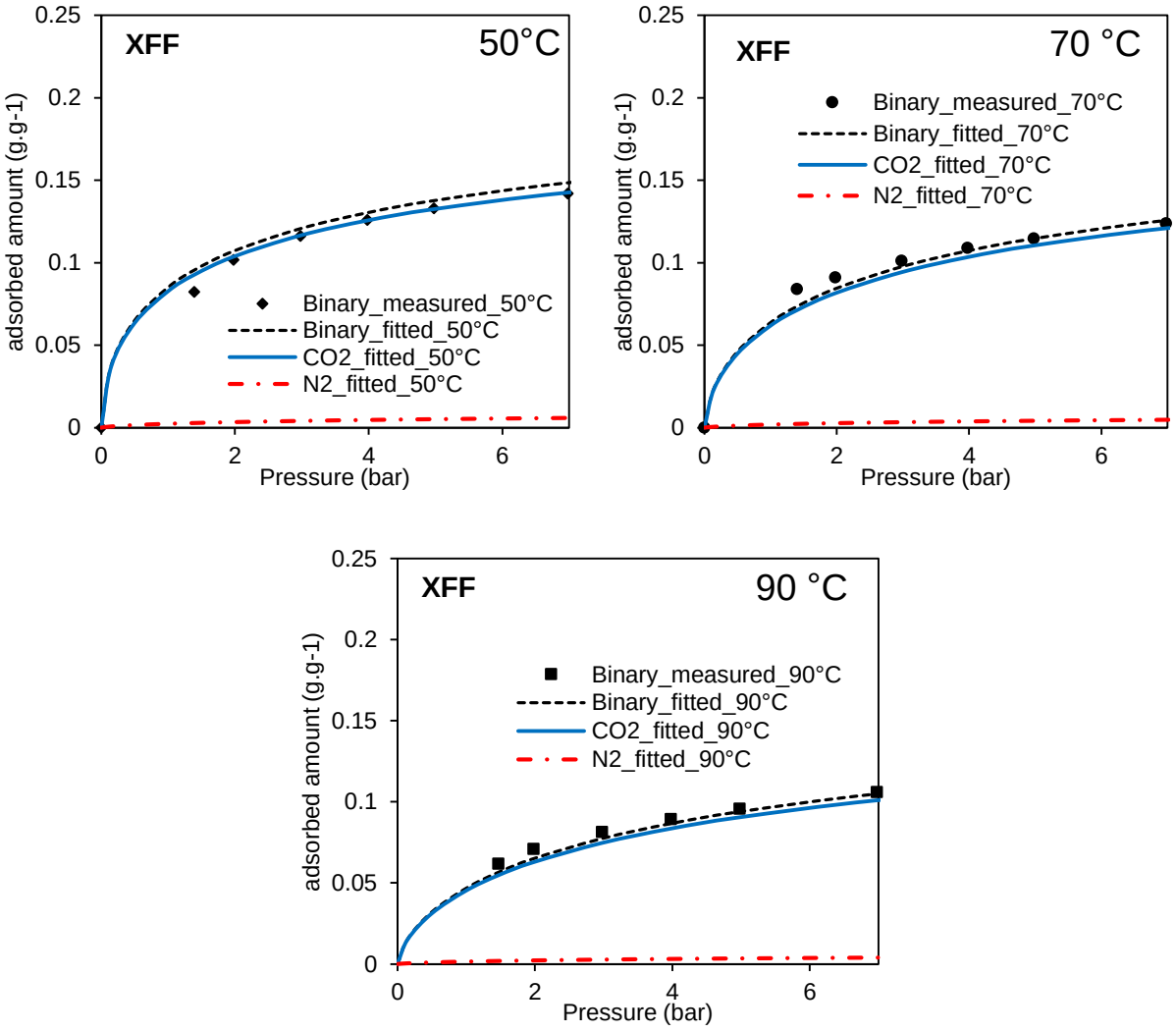

Source: own authorship

SAMPLE ZEO4A

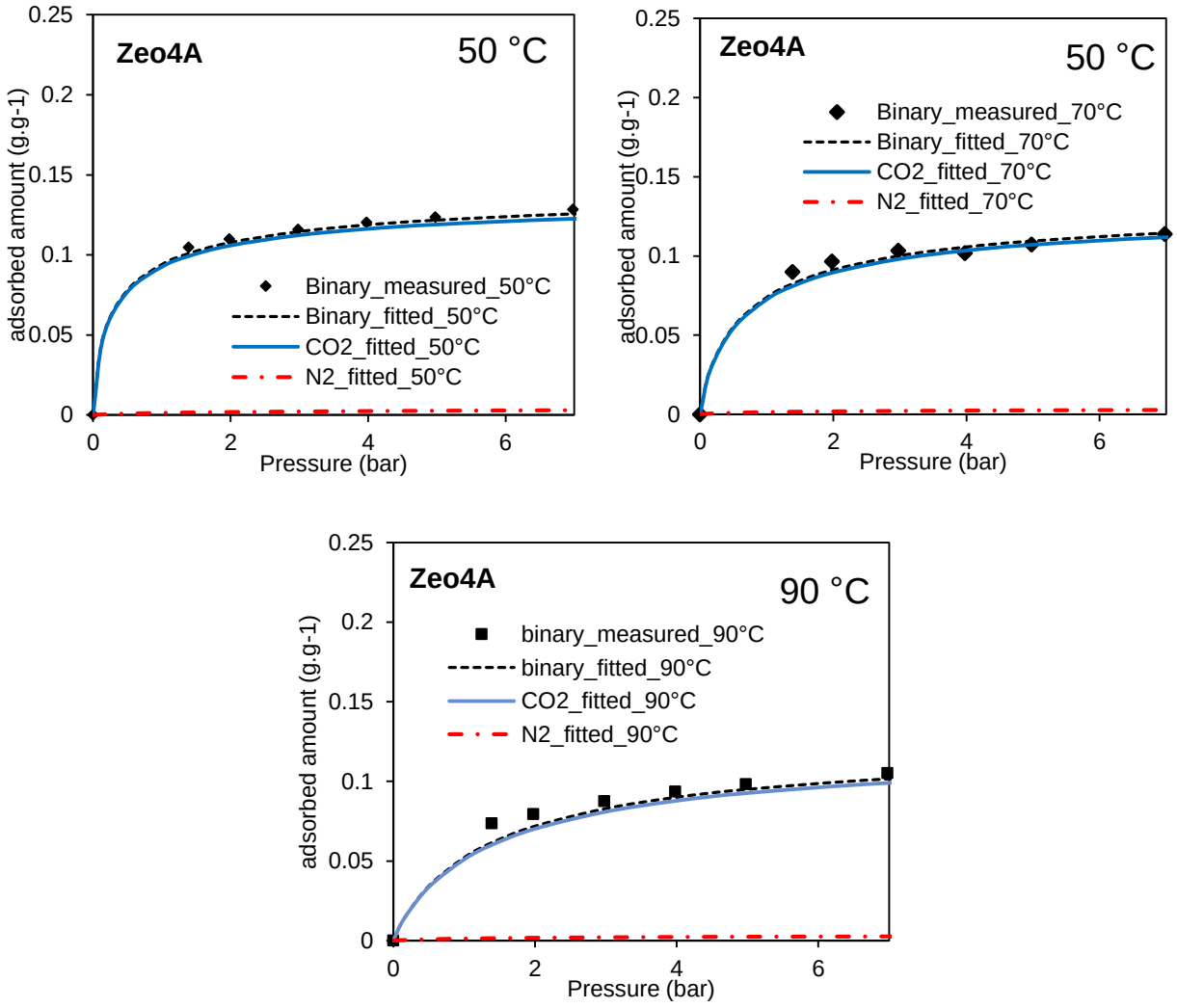

Source: own authorship

SAMPLE PAF

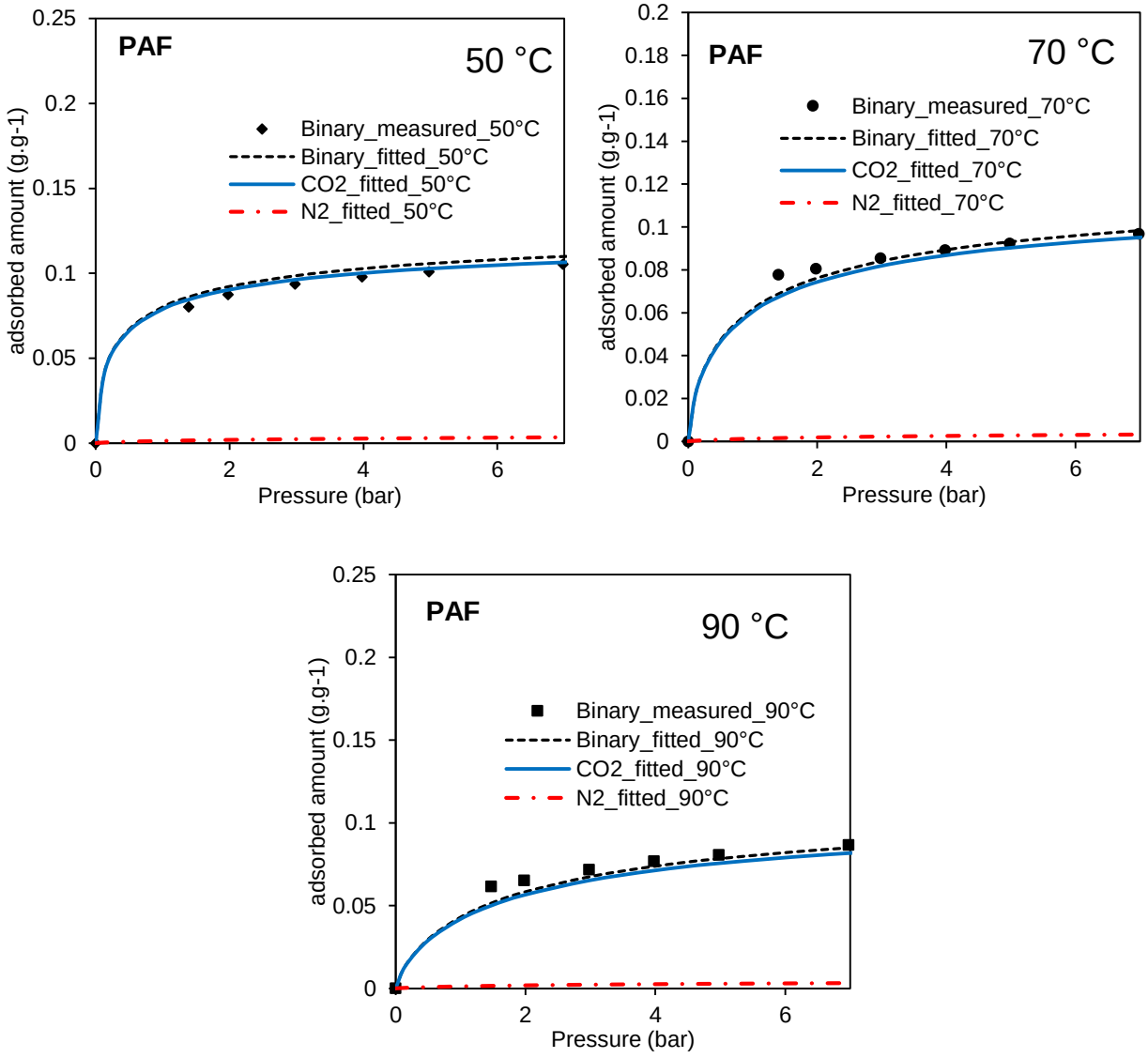

Source: own authorship

APPENDIX E – WATER VAPOR (LEFT) AND BINARY WATER VAPOR/CO2 (RIGHT) ADSORPTION ISOTHERMS ON ZEOLITE 13X AT 50 °C.

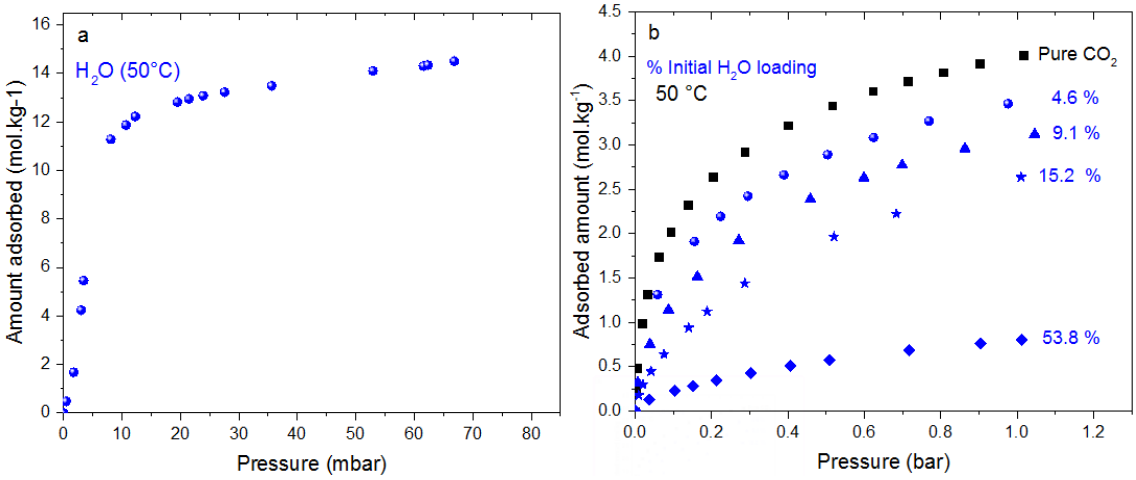

Source: own authorship